SCUOLA DI DOTTORATO

UNIVERSITÀ DEGLI STUDI DI MILANO-BICOCCA

Department of Earth and Environmental Sciences (DISAT)

PhD Program in Chemical, Geological and Environmental Sciences, Cycle XXXIII°

Curriculum in Geological Sciences

On the application of Raman micro-Spectroscopy to the characterisation of Earth's CO_2 fluids

REMIGI SAMANTHA

Registration number: 769984

Tutor: Prof.ssa Frezzotti Maria Luce

Co-tutor: Prof. Bodnar Robert J.

Supervisor: Prof.ssa Frezzotti Maria Luce

Coordinator: Prof. Marco Giovanni Malusà

ACADEMIC YEAR 2020/2021

ABSTRACT (English Version)

This thesis aims to investigate the applicability of Raman micro-spectroscopy as densimeter and mass-spectrometer for the calculation of density and C_{CO2} isotopic composition to improve the characterisation of Earth's CO_2 fluids trapped as fluid inclusions in peridotites. Based on the properties of the Raman spectrum of CO_2, where the distance (Δ) of the two main vibrations (ν_1 and ν_2) is density-dependent and both the $^{13}CO_2$ and $^{12}CO_2$ isotopologues ν_1 vibrations are present, Raman micro-spectroscopy has the potential to become a complementary technique for the in situ characterisation of CO_2 fluid inclusions in different rocks, allowing as the ultimate goal to better understand the C transport and recycling mechanisms within Earth. To this, CO_2 fluid inclusions trapped in peridotitic mantle xenoliths, enabling the acquisition of Raman spectra where parameters like bands position and areas can be measured with high precision, have been analysed.

The calculation of C_{CO2} isotopic composition by Raman micro-spectroscopy is possible due to the proportionality between $^{13}CO_2$ ν_1 and $^{12}CO_2$ ν_1 areas with their molar concentration within fluid inclusions. However, the calculation of area ratios requires precision at the fourth decimal place to calculate $\delta^{13}C_{CO2}$ values representative of Earth's natural reservoirs. Raman spectra are affected by unavoidable random effects - due to noise from various sources which reduce the precision of area measurements. Forty-two natural high-density CO_2-pure fluid inclusions from two localities - Lake Tana region (Ethiopia) and El Hierro (Canary Islands) - having comparable sizes and depths from the sample surface have been analysed. For each inclusion, two sets of spectra have been acquired in the same focal point with different acquisition times, at high resolution (1800 gr/mm grating, confocal hole aperture of 100 µm, and laser-powered at 150 mW). Among the 84 sets of measurements, 23 were characterised by $^{13}CO_2/^{12}CO_2$ area ratios differing of more than one order of magnitude one another. These have been removed from the dataset, since caused by random perturbations of spectra. For the remaining 61 sets of measurements, 95% were characterised by area ratios reproducibility $<\approx 4‰$, allowing to calculate FI $\delta^{13}C_{CO2}$ values with a precision of $<\pm\approx 2‰$, with only a few analyses characterised by lower precision, $\approx\pm 7‰$ on average. For area ratios having reproducibility $<\approx 4‰$, calculated $\delta^{13}C_{CO2}$ values for fluid inclusions trapped in mantle xenoliths from the Lake Tana region were consistent with mantle origin, while for those in mantle xenoliths from El Hierro significantly differed from the mantle isotopic signature. Thus, the accuracy of measurement has been checked by bulk measurements. These proved that calculated $\delta^{13}C_{CO2}$ values were accurate, allowing to model $\delta^{13}C_{CO2}$ variations at the single mineral scale.

The adoption of Raman micro-spectroscopy for calculating the density of CO_2 fluids has been previously investigated by many authors that proposed different densimeter equations. However,

for the same Δ values, different equations calculate different densities with a bimodal graphic distribution, the origin of which is not well understood, limiting the adoption of proposed densimeters to single laboratories. The origin of this distribution has been investigated in the present work by calculating the density of 40 CO_2-pure fluid inclusions trapped in mantle xenoliths from El Hierro (Canary Islands) over a variable range (from 0.37 to 1.08 g/cm^3) by mean of microthermometry. CO_2 fluid inclusions Δ values have been successively measured by acquiring Raman spectra applying analytical parameters common to those adopted by some of the existing Raman densimeters authors, and allowing a spectral per pixel resolution of ≈1.50 cm^{-1}/px. The best fit of the Δ-density data distribution has been obtained by a third-order polynomial equation, that calculates CO_2 densities with an error of ±0.015 g/cm^3. The proposed equation plots with those obtained by mean of a similar spectral per pixel resolution. Densimeters, plotting in the different groups, were also characterised by similar but higher spectral per pixel resolution. Moreover, the 95% confidence of Δ-density distribution obtained in proposed and previous works has been calculated by a bootstrapping statistical algorithm. These allowed to assess the accuracy of originally measured Δ-density values for all the densimeters and, in turn, define a cut-off point below which the CO_2 density estimation power is low. For all the densimeters, the cut-off point has been set where the relative distances of computed confidence intervals were lower than 7.5%. For all the equations, the cut-off point corresponded to gas-like CO_2 at ambient conditions and was set at a lower Δ-density value for higher spectral resolution densimeters. The comparison of 95% confidence interval calculated for high and low spectral resolution per pixel equations showed that densimeters having similar spectral per pixel resolution calculate CO_2 densities, which are statistically equivalent at 95% confidence. In contrast, densimeters with different resolutions calculate not comparable CO_2 densities.

Obtained results allowed to preliminarily propose an analytical procedure which allowed to calculate the C_{CO2} isotopic composition of in situ CO_2 fluid inclusions with a precision of ≈±2% for 95% of the analyses. Similar results proved that Raman micro-spectroscopy is a potential complementary method for in situ and non-destructive calculation of $\delta^{13}C_{CO2}$ values, further allowing to trace CO_2 fluids evolution at mantle depths. Moreover, these improved the knowledge about the Δ-density distribution of Raman densimeters, indicating that CO_2 densities calculated by mean of equations having similar spectral resolution are statistically equivalent at 95% confidence for CO_2 fluid inclusions having density values near and above the CO_2 critical point. However, they should be used carefully with gas-like CO_2 fluid inclusions.

ABSTRACT (Italian Version)

Questa tesi si prepone l'obiettivo di investigare l'applicabilità della micro-spettroscopia Raman come densimetro e come spettrometro di massa per il calcolo della densità e della composizione isotopica del carbonio per i fluid a CO_2, al fine di migliorare la caratterizzazione dei fluidi a CO_2 terrestri intrappolati come inclusioni fluide nelle peridotiti di mantello. Negli spettri Raman della CO_2, la distanza (Δ) delle due vibrazioni principali (ν_1 e ν_2) varia in funzione della densità del fluido, inoltre sono distinguibili le vibrazioni degli isotopologi $^{13}CO_2$ e $^{12}CO_2$. Sulla base di ciò, la micro-spettroscopia Raman risulta essere una potenziale tecnica, complementare alla microtermometria e alla spettrometria di massa per la caratterizzazione *in situ* di inclusioni fluide a CO_2, consentendo, come obiettivo finale, di migliorare la comprensione dei meccanismi di trasporto del carbonio nelle zone più profonde della Terra. A questo scopo, nel presente lavoro di tesi sono state analizzate inclusioni fluide a CO_2 intrappolate in xenoliti di mantello, la cui alta densità ha permesso di acquisire spettri Raman in cui parametri come la posizione delle bande e le loro aree possono essere misurate ad alta precisione.

Grazie alla proporzionalità tra le aree delle due vibrazioni degli isotopologi $^{13}CO_2$ ν_1 e $^{12}CO_2$ ν_1 con la loro concentrazione all'interno delle inclusioni fluide, è possibile utilizzare la micro-spettroscopia Raman per il calcolo della composizione isotopica dei fluidi a CO_2. Questo, tuttavia, richiede che i rapporti tra aree calcolati per i due isotopologi in una certa inclusione abbiano una precisione alla quarta decimale al fine di ottenere valori di $\delta^{13}C_{CO2}$ che siano rappresentativi per i serbatoi naturali di carbonio terrestre. L'output grafico degli spettri Raman è influenzato da effetti casuali ed inevitabili dovuti a sorgenti di rumore che contribuiscono a ridurre la precisione delle misure delle aree delle bande in uno spettro. L'applicabilità della micro-spettroscopia Raman per il calcolo delle composizioni isotopiche del carbonio è stata investigata analizzando 42 inclusioni fluide naturali, contenenti CO_2 pura e di alta densità, provenienti dalla regione del Lago Tana (Etiopia) e dall'isola di El Hierro (Isole Canarie), e caratterizzate da dimensioni e profondità simili. Due serie di spettri sono state acquisite per ogni inclusione nello stesso punto focale, attraverso diversi tempi di acquisizione e ad alta risoluzione (grating a 1800 gr/mm, apertura della confocal hole a 100 µm, potenza del laser a 150 mW). Di 84 set di analisi, 23 mostrano rapporti di aree $^{13}CO_2/^{12}CO_2$ che differiscono tra loro per più di un ordine di grandezza. Simili variazioni casuali dei rapporti sono state ritenute causate dalla perturbazione degli spettri dovuti ad effetti di rumore, perciò sono stati rimossi dal dataset. Per i rimanenti 61 set di analisi, il 95% delle misure mostra una riproducibilità dei rapporti tra aree $<\approx 4‰$. Simili riproducibilità consentono di calcolare valori di $\delta^{13}C_{CO2}$ con una precisione di $<\approx \pm 2‰$. Solo poche analisi sono, invece, caratterizzate da una minor precisione, fino a $\approx \pm 7‰$ in

media. Nei set di analisi aventi riproducibilità <≈4‰, per le inclusioni fluide a CO_2 selezionate nei campioni provenienti dalla regione del Lago Tana, la composizione del carbonio calcolata indica un'origine di mantello del carbonio. Per quelle nei campioni provenienti da El Hierro, invece, queste risultano essere molto diverse dai valori tipici per il carbonio mantellico. Per questo motivo, l'accuratezza di queste misure è stata verificata calcolando i valori di $\delta^{13}C_{CO2}$ tramite spettrometria di massa. Queste analisi hanno dimostrato che le composizioni isotopiche del carbonio misurate tramite micro-spettroscopia Raman sono effettivamente accurate alla scala del singolo minerale.

L'applicabilità della micro-spettroscopia Raman per il calcolo della densità dei fluidi a CO_2 è stata precedentemente studiata da molti autori, che hanno proposto diversi densimetri. Tuttavia, è stato osservato che, per gli stessi valori di Δ, equazioni diverse calcolano densità diverse con una distribuzione grafica bimodale, la cui origine non era ancora ben compresa. Ciò ha limitato l'utilizzo dei densimetri proposti in singoli laboratori. L'origine di questa distribuzione è stata studiata calcolando la densità di 40 inclusioni fluide a CO_2 pura, intrappolate in xenoliti di mantello provenienti da El Hierro (Isole Canarie), tramite micro-termometria, su un intervallo di densità variabile (da 0.37 a 1.08 g/cm^3). I valori di Δ delle stesse inclusioni fluide sono stati successivamente misurati mediante l'acquisizione di spettri Raman, applicando parametri analitici comuni a quelli adottati da alcuni degli autori dei densimetri esistenti, con una risoluzione spettrale per pixel di ≈1.50 cm^{-1}/px. Il miglior fitting della distribuzione dei valori di Δ-densità ottenuti è stato raggiunto mediante un'equazione polinomiale del terzo ordine, che ha permesso di calcolare le densità della CO_2 con un errore di ± 0.015 g/cm^3. L'espressione grafica dell'equazione proposta si è inserita nel gruppo di densimetri ottenuti attraverso Δ misurati in spettri con una risoluzione spettrale per pixel simile. È stato possibile, inoltre, osservare che anche i densimetri che formano il secondo gruppo sono caratterizzati da una risoluzione spettrale per pixel simile tra loro, anche se superiore rispetto agli altri. Successivamente, l'adozione di un algoritmo statistico di bootstrap ha permesso di calcolare gli intervalli di confidenza al 95% delle distribuzioni dei valori di Δ-densità, ottenute sia nel lavoro proposto che in lavori precedenti. Gli intervalli di confidenza al 95% hanno permesso di valutare l'accuratezza dei valori di Δ-densità originariamente misurati per tutti i densimetri e, a loro volta, di definire un punto di cut-off al di sotto del quale la potenza di stima della densità della CO_2 è risultata bassa. Per tutti i densimetri il punto di cut-off è stato fissato nel punto in cui le distanze relative degli intervalli di confidenza calcolati sono inferiori al 7.5%. Per tutte le equazioni il punto di cut-off corrisponde alla CO_2 gassosa a condizioni ambiente ed è risultato più basso per i densimetri a maggiore risoluzione spettrale. Il confronto degli intervalli di confidenza al 95% calcolati per le equazioni di alta e di bassa risoluzione spettrale per pixel ha mostrato che densimetri con risoluzione

spettrale per pixel simile calcolano densità della CO_2 statisticamente equivalenti al 95% di confidenza, mentre densimetri con risoluzione diversa calcolano densità non comparabili.

I risultati ottenuti, e presentati nel seguente lavoro di tesi, hanno consentito di proporre una procedura analitica preliminare che ha consentito di calcolare *in situ* il $\delta^{13}C_{CO2}$ in inclusioni fluide con una precisione di ≈±2‰ per il 95% delle analisi. Questi risultati hanno dimostrato come la micro-spettroscopia Raman sia un potenziale metodo complementare per il calcolo *in situ* e non distruttivo dei valori di $\delta^{13}C_{CO2}$, consentendo di tracciare l'evoluzione dei fluidi di CO_2 alle profondità del mantello litosferico terrestre. Inoltre, questi risultati hanno migliorato la conoscenza della distribuzione dei valori di Δ-densità per i diversi densimetri Raman esistenti, indicando che le densità della CO_2 calcolata per mezzo di equazioni ottenute con risoluzione spettrale simile sono statisticamente equivalenti al 95% di confidenza per le inclusioni fluide a CO_2 aventi valori di densità vicini e superiori al punto critico della CO_2. Tuttavia, le equazioni proposte dovrebbero essere usate con attenzione con inclusioni fluide a CO_2 gassosa a condizioni ambiente.

TABLE OF CONTENTS

1. INTRODUCTION AND AIMS OF THE THESIS

1.1 Earth's CO_2 fluids

CO_2-bearing fluids inclusions are extremely common in many geological environments. These can be found in association with water and salts in hydrothermal ore deposits (e.g., alpine-type deposits, epithermal metal deposits, VMS; Roedder, 1963; Roedder, 1984; Roedder and Bodnar, 1997), medium- to high-grade metamorphic rocks (Touret, 1977, 1981, and 1986; Roedder, 1984; Bodnar, 1995, and 2001; Török et al., 2005; Touret and Huizenga, 2012a, and 2012b), and peridotitic and ultramafic mantle xenoliths (Roedder, 1965, and 1984; Pasteris, 1987; Szabó et al., 1996; Andersen and Neumann, 2001; Frezzotti and Touret, 2014).

Similar fluids play an important role in most geological processes occurring at mantle and crustal depths, where they can be responsible for metamorphic and metasomatic reactions and magma genesis and can contribute to the eruptive style in different volcanic systems. Moreover, they allow to characterise the physical and chemical properties of the crust and upper mantle (e.g., pressure, density, temperature and composition) and to reconstruct magmatic dynamics on the ascent and rest in magma chambers (Roedder, 1984; Bergman and Dubessy, 1984; Frezzotti et al., 1994; Roedder and Bodnar, 1997; Bodnar et al., 2014; Yardley and Bodnar, 2014; Frezzotti and Ferrando, 2015; Oglialoro et al., 2017).

CO_2 fluids are extremely abundant within crustal metamorphic rocks and mantle peridotites (Roedder, 1965, Andersen and Neumann, 2001; Frezzotti and Touret, 2014). In metamorphic rocks, CO_2 fluids can assist the reactions and can be produced at any stage of the process (Touret, 1977, and 1992). CO_2 fluid inclusions trapped in metamorphic phases can preserve traces of both the original fluid which have induced the metamorphic reaction or trace the metamorphic evolution of the rocks (Touret, 1977, and 1992; Berkesi et al., 2012).

In peridotites, CO_2 fluids can be present as:

(i) abundant low density (ThL≥20°C; Frezzotti and Touret, 2014) CO_2-rich fluids associated with the last stages of magma resting before the eruptions (i.e., CO_2 fluids originated by degassing of basaltic magmas), allowing to trace the structure of magma chambers beneath volcanic systems (Zanon and Frezzotti, 2013; Zanon, 2015);

(ii) less abundant high density (ThL<0°C; Frezzotti and Touret, 2014) CO_2-rich fluids often associated with carbonates, silicate and carbonate melts, and brines (Frezzotti and Touret, 2014, and references therein). These latter ones can derive from deeper circulation of CO_2-

bearing fluids or carbonate-rich melts. These could be generated by the partial melting of carbonated mantle peridotites, and metasomatic reactions due to the interaction between silicate-carbonate fluids and/or melts with the mantle peridotite or immiscibility (Wallace and Green, 1988; Schrauder and Navon, 1994; Schrauder et al., 1996; Lee and Wyllie, 1998; Dasgupta and Hirschmann, 2006, 2007a,b; Dasgupta et al., 2007; Hydas et al., 2010; Berkesi et al., 2019). Carbonate-rich melts will be quickly consumed on the mantle during ascent, but can produce large amounts of CO_2 trapped in fluid inclusions, associated with brines, and preserve traces of deep carbon mantle outgassing (Frezzotti and Touret, 2014).

CO_2 fluid inclusions in crustal and mantle rocks constitute a direct tool to investigates fluids circulating at crust and mantle depths. Their characterisation is a crucial means to visualize and better understand active lithosphere deformation and recrystallization processes, metasomatic enrichments, partial melting and flux of volatiles through the lithosphere to the exosphere (Touret, 1992; Frezzotti and Touret, 2014).

1.2 Aims of the thesis

The present work of thesis aims to investigate the application of Raman micro-spectroscopy for the characterisation of Earth's CO_2 fluids, preserved as fluid inclusions in natural mantle rocks.

CO_2-rich fluid inclusions trapped in mantle xenoliths preserve uncontaminated traces of paleo-fluids circulating at lithospheric mantle depths, whose chemical-physical parameters (i.e. the density and the $^{13}C_{CO2}/^{12}C_{CO2}$ isotopic ratio) constitute a direct tool to understand the origin of the C and how it is transported and exchanged in the lithospheric mantle.

Historically, classic fluid inclusion studies allowed to investigate the chemistry and the density of CO_2-bearing fluids in crustal and mantle xenoliths (Roedder, 1965; Andersen and Neumann, 2001; Frezzotti and Touret, 2014) by mean of microthermometric analyses (i.e., observation of phase transitions in a heating-freezing stage under the microscope; Roedder, 1962). Bulk mass spectrometry of the main CO_2-rich fluid inclusion-bearing mineral phases constituting rock xenoliths are routinely used to measure the carbon isotopic signature of fluids and melts in their source region and evaluate their metasomatic overprints (Correale et al., 2015; Gennaro et al., 2017; Rizzo et al., 2018; Gaillard et al., 2020, and references therein).

In the last decades, Raman micro-spectroscopy has become an additional routinely used technique in fluid inclusions studies (e.g., Burke, 2001; Frezzotti et al., 2012a; Bodnar and Frezzotti, 2020). It allows a precise characterisation of fluid inclusion chemistry in a punctual (analytical spot of ≈1 μm),

and non-destructive way without requiring complex sample preparation procedures (Frezzotti et al., 2012a, and references therein). For CO_2 fluid inclusions, whose Raman spectrum is affected by the Fermi resonance effect (Fermi, 1931), the application of this technique as CO_2 densimeter has been evaluated, in particular for the characterisation of those fluid inclusions having sizes <3 µm and more likely to preserve the original fluid composition and density, difficult to analyse by mean of microthermometry (Frezzotti et al., 2012a; Campione et al., 2015). Moreover, the presence of the additional $^{13}CO_2$ isotopologue band in CO_2 Raman spectra makes Raman micro-spectroscopy a promising complementary technique to mass-spectrometry to calculate CO_2 fluids C isotopic signature (Bodnar and Frezzotti, 2020). The advantages to adopting Raman micro-spectroscopy to measure the density and the carbon isotopic composition of CO_2 fluid inclusions in minerals reside in the potential to associate the densities and the $^{13}C_{CO2}/^{12}C_{CO2}$ ratio in single fluid inclusions, allowing to characterise further the depths at which C is transported and to identify the origin of C for single CO_2 fluid inclusions generations.

Many works have dealt with the CO_2 density measurement by mean of the "Raman densimeter" method (Rosso and Bodnar, 1995; Kawakami et al., 2003; Yamamoto and Kagi, 2006, and 2008; Song et al., 2009; Fall et al., 2011; Wang et al., 2011; Lamadrid et al., 2017) and the $\delta^{13}C_{CO2}$ "Raman mass spectrometry" (Rosasco et al., 1975; Dhamelincourt et al., 1979; Marshall et al., 1994; Arakawa et al., 2007; Li et al., 2016, 2017, and 2018; Yokokura et al., 2020), but their reliability and applicability are still debated.

This work of thesis investigates the applicability of Raman mass-spectrometry for the calculation of C_{CO2} isotopic compositions (*Manuscript 1*) and Raman densimeter method (*Manuscript 2*) for CO_2 fluid inclusions. It aims to improve the characterisation of these fluids by developing analytical protocols allowing high precision analyses. For the present work, CO_2 fluid inclusions trapped in peridotitic mantle xenoliths have been selected since high-density fluids enable obtaining intense Raman spectra, where parameters like bands position and areas can be measured with high precision. A summary of the main procedures adopted to carry out the analyses during the Ph.D. and the main results and their implications are reported in the following paragraphs.

1.3 Summary of *In-Situ Discrimination of the Carbon Isotopic Signature of Natural CO_2 Fluid Inclusions by Raman Spectroscopy (Manuscript 1)*

Paper by Remigi, S., Frezzotti, M. L., Bodnar, R. J., Sandoval Velasquez A. L., Rizzo, A. L., Aiuppa, A.; to be submitted to *Journal of Raman Spectroscopy*.

The Raman spectrum of CO_2 allows distinguishing the upper bands of the two $^{13}CO_2$ and $^{12}CO_2$ isotopologues. It is known that the areas of the Raman bands of gas molecules within fluid inclusions are proportional to the mass of chemical groups associated with them. Thus, the areas of the two $^{13}CO_2$ and $^{12}CO_2$ upper bands can be used to determine single fluid inclusions $\delta^{13}C_{CO2}$ values. When calculating the isotopic signature of CO_2 by mean of Raman micro-spectroscopy, $^{13}CO_2/^{12}CO_2$ upper bands area ratio should be characterised by precision at the fourth decimal place. The $^{13}CO_2$ isotopologue in natural CO_2 fluids is present in very low relative concentrations (1.1% on average), affecting the precision with which the areas of $^{13}CO_2$ upper bands can be measured. Based on this, many researchers focussed on the development of analytical procedures allowing to apply Raman micro-spectroscopy for the C_{CO2} isotopic composition estimation in synthetic and natural fluid inclusions from different geological environments (Rosasco et al., 1975; Dhamelincourt et al., 1979; Marshall et al., 1994; Arakawa et al., 2007; Li et al., 2016, 2017, and 2018; Yokokura et al., 2020). In order to improve the $^{13}CO_2$ band area measurements, prolonged multiple acquisitions have been performed, allowing the integration of the $^{13}CO_2$ band areas. Prolonged acquisitions, however, may induce erratic background noises, which negatively affect the shapes of the $^{13}CO_2$ bands, resulting, in turn, in loss of precisions. Calculated $\delta^{13}C_{CO2}$ values were characterised by a precision of ±10-20‰, which only distinguished between biogenic and abiogenic carbon sources.

Manuscript 1 aims to investigate the optimal experimental parameters and procedures by which the $^{13}CO_2$ band areas and $^{13}CO_2/^{12}CO_2$ area ratios uncertainties related to the nature of Raman scattering of light can be reduced. This will enable the calculation of $^{13}C_{CO2}/^{12}C_{CO2}$ isotopic ratios in natural single CO_2 fluid inclusions by punctual and non-destructive analyses. To this, 42 high-density CO_2-pure fluid inclusions trapped in Ol, Opx and Cpx from peridotitic mantle xenoliths from the Lake Tana region and El Hierro (Canary Islands) have been analysed by Raman micro-spectroscopy. For each fluid inclusion, two sets of three spectra each have been acquired through different acquisition times. Among the 84 sets of measurements, 23 were characterised by at least one of the three area ratios that erratically diverged from the other two. This kind of random variation should be expected because of the insurgence of random noise effects, which randomly modify the shapes and the areas of the bands within the spectrum; thus, these analyses have been preliminarily removed from the dataset. For the remaining sets of measurements, the reproducibility of calculated area ratios has been obtained by calculating the area ratios *Variance‰* and R*eproducibility‰* to use as internal standards to evaluate the data quality. 95% of measurements sets are characterised by precision at the fourth decimal place and area ratio reproducibility $<\approx$4‰. Similar reproducibility would permit the calculation of fluid inclusions $\delta^{13}C_{CO2}$ values with a precision of units ‰, allowing the discrimination among many C_{CO2} natural reservoirs. For 95% of

the analyses, the precision of calculated $\delta^{13}C_{CO2}$ values was ≈±2‰. However, few $\delta^{13}C_{CO2}$ values significantly diverged from the others, being characterised by low precision up to ≈±7‰ on average. This indicates that it is not possible to avoid completely random perturbations of Raman spectra.

The carbon isotopic compositions calculated for CO_2 fluid inclusions trapped in mantle xenoliths from the Lake Tana region resulted in being of mantle origin (falling, on average, within the range of MORB-like upper mantle, being -8‰<$\delta^{13}C$<-4‰, e.g., Mattey et al., 1984), while those from El Hierro were higher than the MORB-like upper mantle field. The accuracy of these $\delta^{13}C_{CO2}$ values has been further tested by bulk measurements of the C_{CO2} isotopic composition of fluid inclusions trapped in 5 mantle xenoliths from El Hierro. Bulk measurements allowed to prove that, although slightly less precise (Raman based $\delta^{13}C_{CO2}$ values precision ≈±2‰ for 95% of the analyses in mantle xenoliths from El Hierro, vs bulk $\delta^{13}C_{CO2}$ values precision ≈±0.60‰), Raman micro-spectroscopy is capable of calculating accurate and reliable $\delta^{13}C_{CO2}$ values for CO_2 mantle fluids. Moreover, $\delta^{13}C_{CO2}$ values variations in fluid inclusions trapped in Ol, Opx and Cpx from both the localities have been reproduced by bulk $\delta^{13}C_{CO2}$ values from El Hierro mantle xenoliths. Present results indicate that, despite the shortcoming due to the unavoidable spectra perturbations, Raman micro-spectroscopy accurately distinguishes between different natural C_{CO2} reservoirs with a precision of ≈±2‰, being a promising complementary technique to mass spectrometry to trace the evolution of CO_2 fluids circulating at mantle depths.

1.4 Summary of *Inter-Laboratory Application of Raman CO_2 Densimeter Equations: Experimental Procedure and Statistical Analysis Using Bootstrapped Confidence Intervals (Manuscript 2)*

by Remigi, S., Mancini, T., Ferrando, S., and Frezzotti, M. L.; accepted on *Applied Spectroscopy* on 23 November 2020 and first published online on 4 February 2021

Raman spectroscopy has been intensively used to constrain the density of CO_2-bearing fluid and melt inclusions in different geological settings. The CO_2 Raman spectrum is affected by a resonance effect, known as Fermi resonance (Fermi, 1931), which causes the splitting apart of the two main CO_2 vibrations, whose distance (Δ) has been proven to be density-dependent. Based on this, synthetic and natural pure CO_2 fluid inclusions and optical cells have been employed to develop empirical equations that could calculate CO_2 fluid densities at the P-T conditions of the different geological environments by mean of Raman micro-spectroscopy (e.g., Rosso and Bodnar, 1995; Kawakami et al., 2003; Yamamoto and Kagi, 2006; Song et al., 2009; Fall et al., 2011; Wang et al., 2011 and

Lamadrid et al., 2017). Proposed densimeter equations have been empirically obtained using the regression of Δ values measured in CO_2 Raman spectra and independently calculated fluid densities. Although it should be expected for densimeters to calculate equal densities starting from the same Δ value, densimeter equations display a bimodal distribution, calculating densities differing of 0.09±0.02 g/cm^3. *Manuscript 2* aims to investigate the densimeters bimodal distribution, and to which extent the difference in calculated CO_2 densities affects the densimeters applicability.

In order to understand the origin of the bimodal distribution of Raman densimeter equations, the influence of the analytical conditions affecting the measurements of Δ values has been investigated by calibrating a new densimeter equation based on natural mantle CO_2-pure fluid inclusions, and obtained by adopting Raman analytical parameters similar to those applied by Kawakami et al. (2003) and Yamamoto et al. (2006) for their published densimeters and allowing a spectral per pixel resolution of about 1.50 cm^{-1}/px. Obtained spectra have been treated by baseline correction and fitting with a Pseudo Voight fitting curve to improve the accuracy of the Δ measurements. The quality of the spectra has been further checked by the introduction of the *Band shape factor* ($BDS = I_{v1;v2}/FWHM_{v1;v2}$), which allowed to exclude from the considered dataset all those spectra whose fitting accuracy was insufficient to produce reliable Δ values.

The proposed densimeter equation has been calibrated on 27 natural CO_2-pure fluid inclusions having densities from 0.37 to 1.08 g/cm^3, and Δ from 103.44 to 105.13 cm^{-1}. Data well fit with a third-order polynomial equation having an R^2 coefficient equal to 0.994, and a density standard error of ±0.015 g/cm^3. Compared with Raman densimeter equations in literature, the proposed equation plot together with Kawakami et al. (2003) and Yamamoto et al. (2006) densimeters, suggesting a major role of the spectral resolution on the Δ measurements. This has also been confirmed by comparing the equations of Song et al. (2009), Fall et al. (2011), and Wang et al. (2011), which are characterised by similar spectral per pixel resolution and calculates almost equal CO_2 densities for the same Δ value.

Once it has been demonstrated that the bimodal distribution of the densimeter equations depends on the spectral resolution, the applicability of the different equations has been investigated by applying an advanced statistical comparison based on the bootstrap approach. This has been done using an algorithm that allowed the calculation of the 95% confidence intervals for all the existing empirical equations, and transformed them into dataset-independent regressions. Confidence intervals allowed to assess the accuracy of originally measured Δ-d values for all the densimeters and, in turn, define a cut-off point below which the CO_2 density estimation power is low. The cut-off point has been set for all the considered densimeters where the relative distances of computed

confidence intervals were lower than 7.5%. Above this threshold, calculated CO_2 densities were assumed to be no more representative for the actual density of analysed CO_2 fluid inclusions. For high-resolution densimeters, the cut-off points have been set at lower Δ – d than in low spectral resolution densimeters. However, for all the equations, the cut-off points always corresponded to gas-like CO_2 at ambient conditions.

Computed confidence intervals have been successively used to statistically compare all the Raman densimeter equations. From the comparison, it resulted that Raman densimeters calibrated with similar spectral per pixel resolution calculate statistically equivalent CO_2 densities at 95% confidence. In contrast, CO_2 densities calculated by the mean of different spectral per pixel resolution equations are not statistically equivalent; thus, these cannot be compared.

Manuscript 2 demonstrates that the observed bimodal distribution of existing Raman densimeter equations is due to the different spectral resolutions achieved for the calculation of Δ values within the different laboratories. Moreover, there is no strong reason to avoid the interlaboratory adoption of proposed equations if the spectral resolution applied during the analyses is considered. For similar spectral per pixel resolution, in fact, each among the densimeters proposed in this work, by Kawakami et al. (2003), and by Yamamoto et al. (2006), or by Song et al. (2009), Fall et al. (2011) and Wang et al. (2011) can be used to calculate CO_2 densities which are statistically equivalent at 95% of confidence. Existing densimeters, however, calculate reliable densities near and above the critical CO_2 density values, covering P-T range conditions relevant for most geological processes in the crust and the mantle, but should be used carefully for the study of gas-like CO_2 fluid inclusions at ambient conditions.

2. LAYOUT OF THE THESIS

The present work of thesis is organised in two main sections. The first one consists of four chapters (Chapters 1,2, 3, and 4) and aims to give a general introduction regarding CO_2 fluids, the application of the Raman micro-spectroscopy for their characterization, with the related scientific background, and the description of the main techniques adopted to carry out the analyses during the PhD. In particular:

(i) *Chapter 1* briefly introduces the origin of Earth's CO_2 fluids and presents the aims of the present work of thesis, providing a summary of the papers produced during the Ph.D.;

(ii) *Chapter 2* (this chapter) presents the structure of the present work of thesis;

(iii) *Chapter 3* focusses on the characteristics of the CO_2 Raman spectrum and reviews its application to calculate: (i) fluid density by the Raman densimeter method, and (ii) $^{13}CO_2/^{12}CO_2$ isotopic ratio in single fluid inclusions. A summary of the central analytical problematics affecting the precision of bands positions and areas, related to the spectral resolution, noises sources, fitting and calibration of the instrument, is also proposed;

(iv) *Chapter 4* consists of a detailed description of the principles and the leading procedures for both the techniques (i.e., microthermometry and Raman micro-spectroscopy) adopted to study CO_2 fluid inclusions.

The second section (Chapters 6, and 7), consists of two manuscripts, *Manuscript 1* (to be submitted for peer reviews to "Journal of Raman Spectroscopy") and *Manuscript 2* (published in "Applied Spectroscopy", https://doi.org/10.1177/0003702820987601), which discuss in detail the main research lines adopted to investigate the applicability of: (i) Raman spectroscopy as mass spectrometry to the study of C_{CO2} isotopic composition and, (ii) Raman densimeters to the study of the CO_2 fluid inclusions densities, and presents the results obtained during the three years of Ph.D.

For the present work of thesis, CO_2 fluid inclusions trapped in peridotitic mantle xenoliths from El Hierro (Canary Islands; Oglialoro et al., 2017) and the Lake Tana region (Injibara, Ethiopia; Frezzotti et al., 2010, 2012b), have been considered. A summary of the main geological and petrological features of the sampling localities and considered peridotites and fluid inclusions assemblages are reported in the *Appendix* section.

3. SCIENTIFIC BACKGROUND

In this chapter, a summary of the main theoretical aspects required for developing the present work of thesis is reported. In particular, in the following paragraphs, the description of the Raman spectrum of the CO_2, a bibliographic review about the application of the Raman micro-spectroscopy as Raman densimeter and as a tool for the calculation of the CO_2 carbon isotopic composition, and the problems related to spectral acquisition are briefly described.

3.1 The Raman spectrum of CO_2

The molecule of CO_2 is characterised by a linear symmetry having four freedom degrees of motion (expressed as 3N-5 degree of freedom, where N is the number of the atoms within a molecule; Fig. 1): a symmetric in-phase stretching vibration (ν_1), an asymmetric out-of-the-phase vibration (ν_3), and a symmetric bending vibration (ν_2 or $2\nu_2$) consisting of two mutual perpendicular doubly degenerate sublevels ($2\nu_{2a}$ and $2\nu_{2b}$) having the same frequency but opposite direction of vibration and contributing to its symmetry (Herzberg, 1945; Ferraro et al., 2003). The symmetric in-phase stretching mode ν_1 is the only Raman active, with a theoretical frequency comprised between 1332.87 and 1340.00 cm^{-1}, while the asymmetric out-of-the-phase vibration mode ν_3 (with a frequency of about 2349.1-2350.00 cm^{-1}) and the symmetric bending mode $2\nu_2$ (frequency at 667.30 cm^{-1}) are Infra-Red (IR) active (Herzberg, 1945; Gordon and McCubbing, 1966; Rosso and Bodnar, 1995; Ferraro et al., 2003; Hurai et al., 2015).

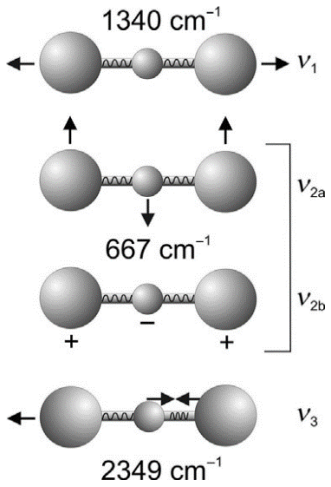

Fig.1 Internal vibration of the CO_2 molecule from Hurai et al., 2015. ν_1 is the Raman active symmetric in-phase stretching mode (frequency between 1332.87 and 1340.00 cm^{-1}); ν_{2a} and ν_{2b}, also referred to as $2\nu_{2a}$ and $2\nu_{2b}$, are the two sublevels contributing to the symmetry of the IR active symmetric bending mode ν_2 or $2\nu_2$ (frequency at 667.30 cm^{-1}); ν_3 is the IR active asymmetric out-of-the-phase stretching mode (frequency

between 2349.1-2350.00 cm^{-1}). Black arrows indicate the sense of motion of each vibrational mode, while the + and – symbols the upward and downward vibrations perpendicular to the paper plan, respectively.

Differing from Raman spectra of other polar gaseous species, which are characterised by a single band referring to the symmetric in-phase ν_1 mode, the CO_2 Raman spectrum consists of two strong bands with frequency at 1285.40 (lower band) and 1388.20 cm^{-1} (upper band) at ambient conditions, respectively (Fig.2; Gordon and McCubbing, 1966). These are referred to as the Fermi diad (Fermi, 1931), arising due to a resonance effect discovered by Fermi in 1931 (Fermi, 1931). The Fermi resonance arises from an anharmonic mixing of the overtone of the symmetric bending mode $2\nu_2$ with the symmetric stretching ν_1 (Amat and Pimbert, 1965; Gordon and McCubbing, 1966; Rosso and Bodnar, 1995; Hurai et al., 2015). In particular, the $2\nu_{2a}$ sublevel of the bending mode $2\nu_2$ has the same symmetry, and nearly the same frequency of the symmetric stretching ν_1, thus they perturb one another in an excited state, inducing an anharmonic vibrational coupling of the potential energy of the molecule (i.e., the Fermi resonance effect). This results in a continuous and contemporaneous excitation of the excited $2\nu_2$ mode by the excited ν_1 one and vice versa, causing the splitting apart of the two strong upper and lower bands frequencies. These latter are constituted by the mixture of both the excited $2\nu_2$ and ν_1 modes, thus could not be assigned to either the $2\nu_2$ or the ν_1 (Amat and Pimbert, 1965; Gordon and McCubbing, 1966; Howard-Lock and Stoicheff, 1971; Garrabos et al., 1989a, 1989b; Rosso and Bodnar, 1995; Hurai et al., 2015), but are generally referred together as the Fermi diad (ν_1-$2\nu_2$) or singularly as ν_1 for the upper band and ν_2 for the lower one.

The Fermi diad (ν_1-$2\nu_2$) is flanked by two satellite bands at about 1264 and 1409 cm^{-1} at ambient conditions (Fig.2), representing the second Fermi diad (Gordon and McCubbing, 1966; Rosso and Bodnar, 1995; Rudolph et al., 2006) and referred to the hot bands (Dickinson et al., 1929; Colthup et al., 1975; Rosasco et al., 1975; Dhamelincourt et al., 1979; Van den Kerkhof and Olsen, 1990; Rosso and Bodnar,1995; Dubessy et al., 1999; Frezzotti et al., 2012a). The hot bands arise due to the transition originated from the excited vibrational levels due to the thermal energy of the molecule. The forming excited levels (ν_1+ν_2 at 1994.88 cm^{-1}, and $3\nu_2$ at 2014.48 cm^{-1}) have, again, near the same energy and, thus, form a degenerate pair affected by the Fermi resonance (Gordon and McCubbing, 1966; Rosso and Bodnar, 1995; Rudolph et al., 2006).

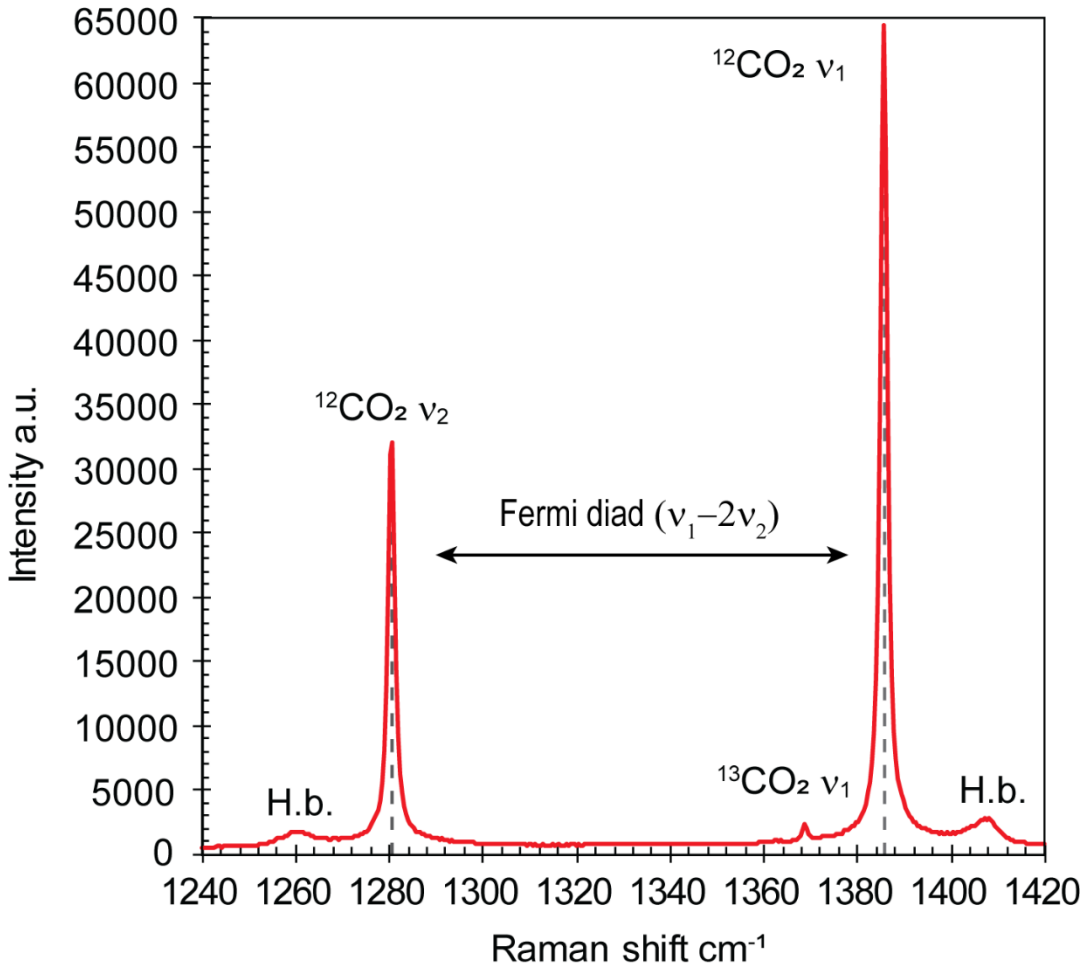

Fig.2 Figure showing Raman spectra acquired for a pure CO_2 fluid inclusion in a peridotitic sample from El Hierro (Canary Islands). The upper and lower bands (ν_1 and ν_2) referring to the $^{12}CO_2$ Fermi diad (ν_1-2 ν_2), the hot bands (H.b.), and the additional upper band (ν_1) of the $^{13}CO_2$ isotopologue are visible.

An additional weak band distorting the symmetry of the CO_2 molecule is also present at about 1370 cm^{-1}, at ambient conditions (Fig.2; Stoicheff, 1958; Howard-Lock and Stoicheff, 1971; Rosasco et al., 1975; Dhamelincourt et al., 1979; Rosso and Bodnar, 1995; Frezzotti et al., 2012a; Hurai et al., 2015). This band is referred to as the $^{13}CO_2$ upper band (ν_1) composing the Fermi diad related to the isotopic splitting of the $^{13}CO_2$ molecule. Since it has been demonstrated that the Fermi resonance affects the $^{13}CO_2$ isotope in a significantly weaker but not negligible way (Irmer and Graupner, 2002), the $^{13}CO_2$ lower band should also be present at around 1260 cm^{-1}, although its actual frequency remains uncertain because overlapped by the more intense hot band, with frequency at 1264 cm^{-1} (Irmer and Graupner, 2002; Arakawa et al., 2007; Yokokura et al., 2020). Finally, when high-resolution analyses are performed with prolonged acquisition times (i.e., few minutes), two more additional bands could be observed at about 1258 and 1364 cm^{-1}, respectively (Stoicheff, 1958; Irmer

and Graupner, 2002). These have been attributed to the Fermi diad relative to the $^{12}C^{16}O^{18}O$ isotopologue (Stoicheff, 1958; Irmer and Graupner, 2002).

We refer to $^{12}CO_2$ ν_1 and $^{12}CO_2$ ν_2 for the upper and lower bands of the $^{12}CO_2$ isotopologue and $^{13}CO_2$ ν_1 for the upper band of the $^{13}CO_2$ one.

3.2 Raman micro-spectroscopy applied for the investigation of CO_2 fluids

3.2.1 CO_2 Raman densimeters

The shifts of the symmetric stretching bands observed in Raman spectra of many gas phases (i.e., H_2, N_2, O_2, CO_2, and CH_4) are pressure and density-dependent (Fabre and Couty, 1986; Dubessy et al., 1989; Seitz and Pasteris, 1990; Fabre and Oksengorn, 1992; Seitz et al., 1993; Gu et al., 2000; Burke, 2001). Many works have focussed on the possibility to develops equations allowing the direct measurement of the fluid density, and thus, pressure, based on the Raman spectrum of such gases (Chou et al., 1989; Seitz et al., 1993; Rosso and Bodnar, 1995; Kawakami et al., 2003; Yamamoto and Kagi, 2006 and 2008; Lin et al., 2007; Song et al., 2009; Fall et al., 2011; Wang et al., 2011; Shang et al., 2014; Lamadrid et al., 2017; Sublett et al., 2019). For gas like CH_4 and N_2, whose Raman spectrum is characterised by a single ν_1 strong band, however, the development of Raman-based densimeter equations is complicated by the strong dependency of the measured positions of the bands by instrumental drifts, which lead to uncertainties on the correct estimation of the their "true" positions (Sublett et al., 2019).

The CO_2 Raman spectrum is affected by the Fermi resonance effect, which causes the splitting apart of the symmetric stretching vibration in two strong bands (i.e., the upper and the lower bands, ν_1 and ν_2, respectively) composing the Fermi diad (ν_1-$2\nu_2$). Generally, the bands composing a Raman spectrum of gas species could vary in shape, intensity or position based on the variation of the environment surrounding a molecule. Similar variations influence the polarizability of the molecule itself, originating a dipolar moment that affects the molecular vibration. In the CO_2 spectrum, the change of the CO_2 density, coupled with the Fermi resonance effect, leads to the shifting of the Fermi diad toward lower frequencies for increasing densities and vice versa. Although the ν_2 has a higher density dependence than the ν_1 (i.e., ν_2 shifting is higher in magnitude than that of the ν_1), the distance, Δ, between the two has a linear function with the density, and it is independent by instrumental drifts (Wright and Wang, 1973; Garrabos et al., 1980; Van den Kerkhof, 1988; Sublett et al., 2019). For these reasons, Raman spectra of CO_2 fluids at different P-T conditions have mainly been studied as

the more promising gas spectra for the direct calculation of reliable and accurate fluid densities and pressures.

After the pioneering work of Rosso and Bodnar (1995), which first proposed a Raman densimeter linear equation, other researchers investigated the Raman densimeter applicability.

Different experiments, based on synthetic and natural pure CO_2 fluid inclusions of variable density, have been used in order to propose six empirical relations that could better represent fluids density in different geological environments (Rosso and Bodnar, 1995; Kawakami et al., 2003; Yamamoto and Kagi, 2006; Song et al., 2009; Fall et al., 2011; Wang et al., 2011 and Lamadrid et al., 2017).

Single densimeters resulted from the most accurate mathematical expression of the relationships between CO_2 density values and Δ measurement in CO_2 Raman spectra for selected density ranges and adopted analytical setups, which are summarized as follows:

- Rosso and Bodnar (1995) linear equation (first densimeter equation investigating synthetic H_2O-CO_2 fluid inclusions obtained at 500°C and 5 kbar, at 600°C at 3 kbar and 700°C and 1.5 kbar, respectively, calculated by the Sterner and Bodnar, 1991, CO_2 EOS). The linear densimeter has been obtained for measured Δ values ranging from 102.6 to 105.2 cm^{-1} and fluid inclusion densities, calculated by microthermometry, from 0.025 to 1.00 g/cm^3. The standard error in Raman calculated density is ±0.02 g/cm^3. Inclusions have been analysed using a Dilor XY modular spectrometer coupled with an Olympus BH2 optical microscope. For the analysis, the adopted configuration was: a 514 nm Ar^+ ion laser, a 1200 gr/mm dispersion grating, a slit width of 100 μm and a 256*1024 CCD Peltier-cooled detector. Spectra have been collected into the region from 944.7 to 1805.1 cm^{-1}, with a spectral resolution of 4.6 cm^{-1}/px. Raman instrumental calibration has been performed with Ne lines.

- Kawakami et al. (2003) cubic equation (densimeter investigating natural and synthetic CO_2 pure fluid inclusions, P-T conditions from the lithospheric mantle to the upper crust, calculated by the Sterner and Pitzner, 1994, CO_2 EOS). The cubic densimeter has been obtained by the interpolation of measured Δ ranging from 102.71 to 105.07 cm^{-1}, with densities from 0.1 to 1.21 g/cm^3. The standard error in the Raman calculated densities is equal to ±0.02 g/cm^3. Inclusions have been analysed using the Chromex 250is single polychromator system, coupled with an Olympus BX60 optical microscope. The adopted analytical configuration for the Δ measurement was: a 514 nm Ar^+ ion laser, a 600 gr/mm grating and a 256*1024 CCD camera detector. Calculated spectral resolution was 1.5 cm^{-1}/px. Raman instrumental calibration has been performed by Naphthalene.

- Yamamoto et al. (2006) cubic equation obtained for the same inclusions and with the same Raman System configuration of Kawakami et al. (2003), but extending the density interval up to 1.24 g/cm^3, corresponding to a Δ value equal to 106.1 cm^{-1}. The standard error in the Raman calculated densities is equal to ±0.01 g/cm^3.

- Song et al. (2009) cubic equation (densimeter investigating synthetic nearly pure CO_2 fluid inclusions representative for P-T conditions from the lithospheric mantle to the upper crust, calculated by Angus, 1976, CO_2 EOS). The cubic densimeter was obtained by interpolating measured Δ values from 102.82 to 105.22 cm^{-1}, with densities ranging from 0.057 to 1.049 g/cm^3. The standard error in the Raman calculated densities is equal to ±0.03 g/cm^3. Inclusions have been investigated with a Horiba Jobin Yvon HR Raman System. The analytical setup was: a 532 nm laser and an 1800 gr/mm grating. Spectra have been acquired into the spectral region from 1200 to 1500 cm^{-1}, with a spectral resolution of 1 cm^{-1}/px. The instrumental calibration has been performed by diamond.

- Fall et al. (2011) cubic equation (densimeter investigating synthetic H_2O-CO_2-NaCl fluid inclusions of variable salinity, representing different P-T conditions from hydrothermal systems to medium- to high- grade metamorphic rocks, calculated by mean of the Span and Wagner, 1996, CO_2 EOS). The cubic equations were obtained by interpolating measured Δ values from 102.7 to 105.5 cm^{-1}, with densities from 0.019 to 1.081 g/cm^3. The standard error in the Raman calculated densities is equal to ±0.035 g/cm^3. Inclusions have been analysed by a Horiba Jobin Yvon HR Raman System. The analytical configuration was: a 514 nm Ar+ ion laser, a 600 gr/mm grating, a slit width of 150 μm and a 1024 CCD detector. The spectral resolution with this configuration was equal to 1 cm^{-1}/px. The Raman instrumental calibration has been performed by Ne lines.

- Wang et al. (2011) cubic equation (densimeter investigating synthetic pure CO_2 inclusions representative for the P-T conditions of the upper crust, calculated by mean of Span and Wagner, 1976, CO_2 EOS). The cubic equation has been obtained by the interpolation of Δ values from 103.06 to 105.39 cm^{-1}, with densities from 0.047 to 1.0006 g/cm^3. The standard error in the Raman calculated densities is equal to ±0.011. Inclusions have been analysed with a Horiba Jobin Yvon HR Raman System. The analytical configuration was: a 532 nm laser, an 1800 gr/mm grating and a 1024 CCD detector. The spectral resolution was 1 cm^{-1}/px. The instrumental calibration has been performed by mean of the diamond and the Benzonitrile standards.

- Lamadrid et al. (2017) linear equation (densimeter investigating synthetic low density pure CO_2 fluids contained in melt inclusions from shallower crustal P-T conditions, calculated by mean of

the Span and Wagner, 1996, CO_2 EOS). The linear equation was obtained by interpolating measured Δ values from 102.64 to 103.23 cm^{-1}, with densities from 0.001 to 0.207 g/cm^3. The standard error in the Raman calculated densities is equal to ±0.0034 g/cm^3. Inclusions have been analysed by mean of a Horiba Jobin Yvon HR Raman System. The analytical configuration was: a 514 nm Ar+ ion laser, an 1800 gr/mm grating and a 1024 CCD detector. The spectral resolution was 0.575 cm^{-1}/px. The instrumental calibration has been performed by mean of the Ne lines.

In Figure 3, the graphical comparison of Δ values measured in spectra with CO_2 density values shows a discreet distribution of the different densimeter polynomial regression curves in the density interval from 0.01 to 1.20 g/cm^3, forming two discreet groups of curves. If considered separately, the first group of regression curves (Kawakami et al., 2003, and Yamamoto and Kagi, 2006; K and Y, respectively in Fig.3) almost overlaps (within 0.01 g/cm^3 difference) in the density interval from 0.20 to 0.77 g/cm^3 (corresponding to Δs from 102.96 to 104.28 cm^{-1}; Fig.3a) and slightly diverges, reaching 0.03 g/cm^3 as the maximum difference for densities higher than 1.00, and lower than 0.12 g/cm^3, respectively ($\Delta s > 104.85$ and < 102.74 cm^{-1}, respectively; Figs.3b and c). The latter group of regression curves (Song et al., 2009; Fall et al., 2011; Wang et al., 2011) shows an almost parallel distribution and calculates density values differing no more than 0.03 g/cm^3 in the density interval from 0.10 to 1.05 g/cm^3 (Fig.3).

Consequently, while the mean deviation of the densities calculated within each group of densimeters is negligible, it can become critical when comparing data from the two distinct groups. For example, an error of 0.09 g/cm^{-1} for CO_2 fluid densities of 0.2 g/cm^3 corresponds to an overestimated density of 50%. While, at much higher fluid densities, such, as mantle CO_2 (d=1.00 g/cm^3), the error is less than 10%. Thus, the reliability of the interlaboratory application of the proposed densimeters has been questioned (Lamadrid et al., 2017).

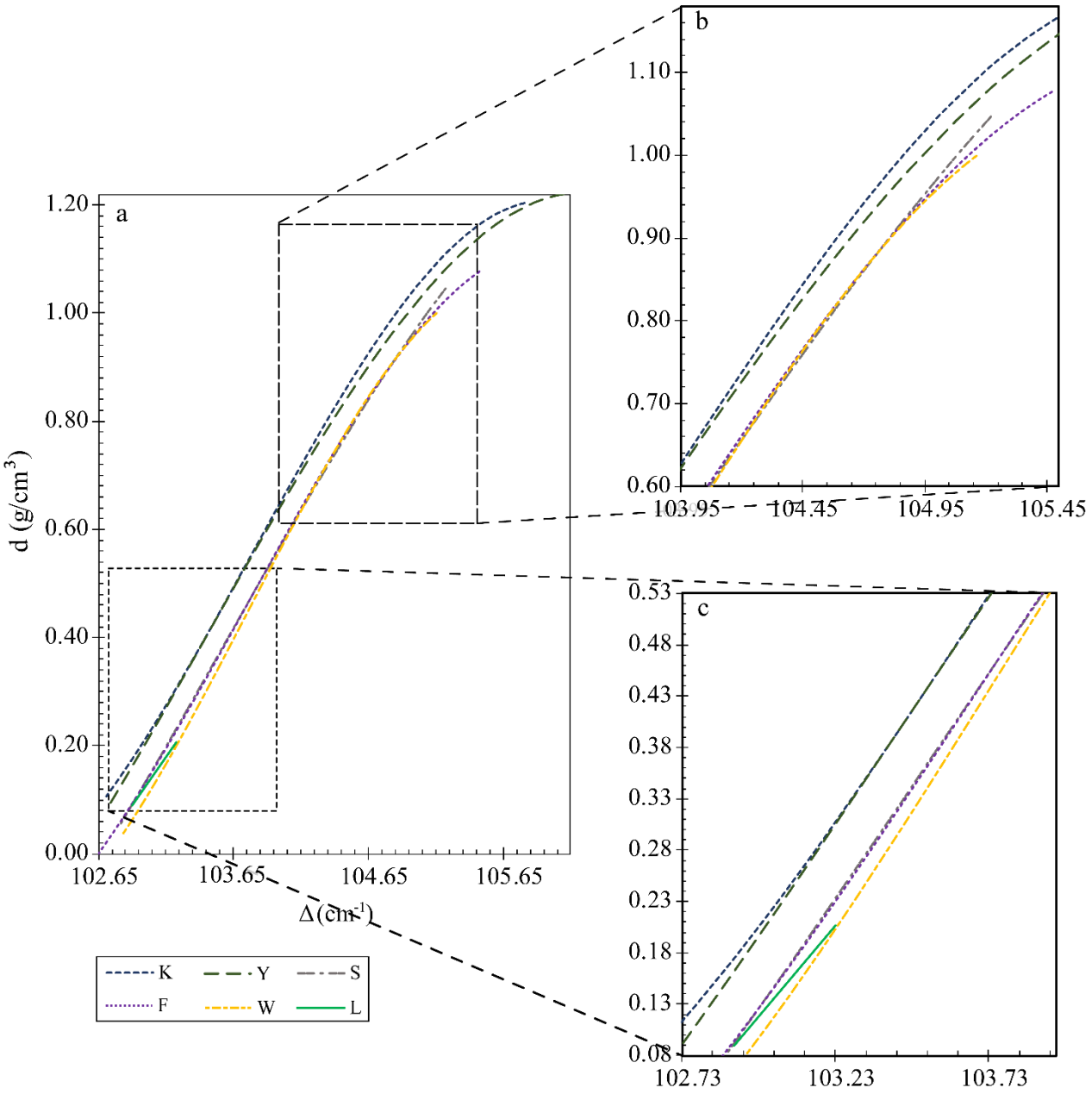

Fig.3 Graphical expression of Raman densimeter empirical equations on a Δ – density plot. (a) Plot showing the different densimeter regressions, forming two discreet groups of parallel curves. (b) Enlargement of the density interval characterising liquid-like CO_2 fluids. (c) Enlargement of the density interval characterising near-critical to gas-like CO_2 fluids. The linear equations of Rosso and Bodnar (1995) and Lamadrid et al. (2017) have been not considered since they are not comparable with all the other densimeter regressions. K = Kawakami et al. (2003); Y = Yamamoto and Kagi (2006); S = Song et al. (2009); F = Fall et al. (2011); W = Wang et al. (2011); L = Lamadrid et al. (2017); Δ = distance of the Fermi diad split; d = density.

A possible explanation, leading to the observed differences in CO_2 densities, has been found in the equations of state (EOS) adopted for the independent calculation of the density of CO_2 fluids, which have been related to the Δ values measured in CO_2 Raman spectra (Lamadrid et al., 2017). In

particular, most of the studies (Fall et al., 2011; Wang et al., 2011; Lamadrid et al., 2017) used the equation of state of Span and Wagner (Span and Wagner, 1996), while only two (Kawakami et al., 2003; Yamamoto and Kagi, 2006) that of Sterner and Pitzer (1994). CO_2 densities calculated over a similar P range at the same T with both the EOS, however, differed less than 1%. Therefore, the different equations of state cannot be considered responsible for the observed density differences.

Another and more likely explanation of the observed densimeters graphical distribution has been attributed to variations of the measured Δ values in Raman spectra. These latter ones could have depended by:

(i) Variation associated with the instrumentation, such as changes of the room temperature (Gaufres et al., 1995; Mestari et al., 1997; Fukura et al., 2006), Raman systems hardware configurations (Lamadrid et al., 2017), or confocal aperture and slit width (Seitz et al., 1994; Lamadrid et al., 2017);

(ii) Variation associated with the data collection and densimeter calibrations, such as choice of the diffraction grating, laser source wavelength, or calibration standard adopted for the calibration of spectrometer linearity (Lin et al., 2007; Lamadrid et al., 2017);

(iii) Variations associated with laser heating of the inclusions (i.e., changes of the CO_2 fluids temperature due to laser irradiation coupled with high magnifications; Hagiwara et al., 2021).

All these factors have been demonstrated to account for observed Δ differences (cf. chapter 3, paragraph 3 of the present work of thesis), leading to the calibration of different densimeter equations. Based on this, it has been concluded that it is better if each research lab, which focusses on CO_2 fluids study, calibrates its own Raman densimeter, rather than use one of those published in the literature to calculate CO_2 fluid inclusions density or to interpret CO_2 Raman data (Lamadrid et al., 2017). These conclusions, however, limited the application of Raman spectroscopy for the calculation of CO_2 density fluid to a single laboratory level, minimising the advantages of using this technique.

3.2.2 Carbon isotopic composition of CO_2 fluids based on the CO_2 Raman spectrum

Raman spectroscopy has been widely applied to estimate the molar amount of Raman active gas (e.g., CO_2, CO, N_2, H_2S, CH_4, O_2, H_2, and SO_2) components within gas mixtures commonly found in natural systems (i.e., fluid inclusions). Raman quantitative analyses are possible by applying a simple formula derived from Placzek's polarizability theory (Placzek, 1934), according to which in a system of freely oriented molecules (i.e., volatiles in fluid inclusions), the Raman scattering intensity depends

on the number of scattering molecules within it (Placzek, 1934; Schrötter and Klöckner, 1979). The intensity of a Raman band is further determined by the scattering cross-section or scattering efficiency (σ, i.e., the magnitude of the molecular vibration change of polarizability induced by exciting radiation with $\bar{\nu}_0$ wavelength; Schrötter and Klöckner, 1979; McMillan, 1985), and by the instrumental efficiency for the component under consideration (indicated as η in Wopenka and Pasteris, 1986, and 1987, and Pasteris et al., 1988; while as ζ in Dubessy et al., 1989; Burke, 2001 and Frezzotti et al., 2012a; from now on we refer to the instrumental efficiency as ζ). Thus, the relation existing between volatiles species band intensities and the number of molecules of considered species within the system could be expressed by the equation [Eq.1]:

$$X_a = \frac{I_a}{\sigma_a * \zeta_a} \qquad \text{[Eq.1]}$$

where X_a is the concentration of a gas species a, I_a the Raman intensity of the species a, σ_a the relative wavelength-dependent Raman scattering cross-section of the specie a, and ζ_a the instrumental efficiency for the species a (Wopenka and Pasteris, 1986, and 1987, and Pasteris et al., 1988; Dubessy et al., 1989; Seitz et al., 1996; Burke, 2001; Frezzotti et al., 2012a). Based on [Eq.1], the molar fraction of a component within the system can be calculated as [Eq.2]:

$$X_a = \frac{\frac{I_a}{\sigma_a * \zeta_a}}{\sum_a^n \frac{I_n}{\sigma_n * \zeta_n}} \qquad \text{[Eq.2]}$$

where X_a and is the molar fraction of the gas component a, I_a and I_n the Raman intensities of the component a and of all the components n measured within the system, I_a the Raman intensity of the specie a, and $\sigma_a, \sigma_n, \zeta_a$ and ζ_n the Raman scattering independent cross-section and the instrumental efficiency for the gas component a and for all the gas components n within the system (Wopenka and Pasteris, 1986, and 1987, and Pasteris et al., 1988; Dubessy et al., 1989; Seitz et al., 1996; Burke, 2001; Frezzotti et al., 2012a). [Eq.2] could be simplified by combining σ and ζ in the *"Raman quantification factor"*, F (Wopenka and Pasteris, 1986, and 1987, and Pasteris et al., 1988; Seitz et al., 1996), thus it becomes:

$$X_a = \frac{\frac{I_a}{F_a}}{\sum_a^n \frac{I_n}{F_a}}$$

Since the approach to quantitative fluid inclusions analyses requires to determine the ratio of two or more species (Pasteris et al., 1988), [Eq.2] can be written as [Eq.3]:

$$\frac{X_a}{X_b} = \frac{I_a}{I_b} * \frac{F_b}{F_a} \qquad \text{[Eq.3]}$$

Seitz et al. (1993 and 1996) demonstrated that the band areas, and thus, their ratios, of the gas species within fluid inclusions are very sensitive to the fluid composition but insensitive to the fluid pressure and to the Raman analytical setups (i.e., slit width), whereas the intensity ratios are sensitive to all these factors. Based on this, authors suggested to prefer area ratios rather than intensity ones to calculate the molar fraction of the volatile species within the fluid inclusions, thus [Eq.3] can be written as [Eq.4]:

$$\frac{X_a}{X_b} = \frac{A_a}{A_b} * \frac{F_b}{F_a} \qquad \text{[Eq.4]}$$

The idea to relate the intensities and areas of the $^{13}CO_2$ ν_1 and the $^{12}CO_2$ ν_2 isotopologues observed in the Raman spectrum of CO_2 to its carbon isotopic composition was first suggested by Rosasco et al. (1975). While studying a natural three-phase (L_1+L_2+V) CO_2-rich fluid inclusion in a quartz sample from Brazil, the authors noticed the additional presence of the $^{13}CO_2$ ν_1 in the CO_2-rich fluid inclusion Raman spectrum. The ratios of measured intensities have been used to calculate the $\delta^{13}C_{CO2}$ in respect to the $^{13}C_{CO2}/^{12}C_{CO2}$ isotopic ratio of the standard PDB (Pee Dee Belemnite; Schwartz, 1969) according to equation [Eq.5]:

$$\delta^{13}C_{CO2} = \left\{ \left[\frac{\left(\frac{X_{13CO2}}{X_{12CO2}}\right)_{Fi}}{\left(\frac{C_{13CO2}}{C_{12CO2}}\right)_{PDB}} \right] - 1 \right\} * 1000 \qquad \text{[Eq.5]}$$

where $\left(\frac{X_{13CO2}}{X_{12CO2}}\right)_{Fi}$ is the $^{13}C_{CO2}/^{12}C_{CO2}$ molar fraction isotopic ratio calculated for analysed fluid inclusion, and $\left(\frac{X_{13CO2}}{X_{12CO2}}\right)_{PDB}$ is the $^{13}C_{CO2}/^{12}C_{CO2}$ isotopic ratio of the standard PDB.

Due to the errors involved in measuring the intensity of the small $^{13}CO_2$ ν_1, however, performed calculations attained a very low $\delta^{13}C_{CO2}$‰ precision (about ±20‰).

Four years later, Dhamelincourt et al. (1979) made another attempt to calculate the carbon isotopic composition of CO_2 fluids trapped in a natural CO_2-rich fluid inclusion in a quartz sample from Camperio (Switzerland). The authors calculated 11 $^{13}CO_2$ $\nu_1/^{12}CO_2$ ν_1+$^{12}CO_2$ ν_2 intensity ratios to evaluate the reproducibility of their Raman band intensities measured for the same fluid inclusion. Obtained C_{CO2} isotopic compositions had a precision of ±37‰. The achieved low precision of the calculations has been related to the adopted analytical protocol not allowing precise intensity measurements of the $^{13}CO_2$ ν_1 band. The authors, however, suggested that by changing the analytical setup and the data processing method, it could have been possible to increase the intensity ratios

reproducibility more than 10 times. According to the authors, with similar analytical corrections, Raman spectroscopy could have become a valid alternative to mass spectrometry, allowing the measurements of C_{CO2} isotopic compositions in a punctual and non-destructive way, potentially allowing to monitor the changes and the evolution of the fluid isotopic composition within the rocks with greater representatively than that of bulk techniques.

These pioneering works posed the basis for developing a new analytical methodology based on Raman spectroscopy for the CO_2 fluids stable isotope geochemistry.

With the advent of Raman systems and detectors of new generations, which improved the precision of Raman analyses, many researchers further investigated the applicability of Raman spectroscopy for the calculation of CO_2 carbon isotopic composition in single fluid inclusions.

In 1994, Marshall et al. (1994) performed some experiments to re-evaluate Raman spectroscopy to determine the $^{13}C_{CO2}$ and $^{12}C_{CO2}$ concentrations in geological fluids. To this, the authors analysed two samples containing synthetic CO_2 fluid inclusions with known $^{13}C_{CO2}/^{12}C_{CO2}$ ratios ($\delta^{13}C_{CO2}$‰= -31.8‰ and +1.2‰, respectively), and one natural sample containing CO_2-rich fluid inclusions. From the three samples, 25 Raman spectra have been acquired by mean of a 514 nm Ar^+ ion laser source, powered approximatively at 25 mW at the sample surface, in a non-confocal mode. Each spectrum resulted from multiple scans of 8 to 30 minutes' acquisitions, performed to obtain the maximum counting scattering points without saturating the detector. Measured band areas resulted from the integration of the multiple scans. Area ratios have been obtained by dividing the $^{13}CO_2$ ν_1 areas by the sum of the $^{12}CO_2$ ν_1 and ν_2 ones. The reproducibility of the calculated area ratios ranged from 63.2 and 93.0‰ for synthetic fluid inclusions and was equal to 7.4‰ for the natural ones. The enormous difference observed for attained reproducibility between synthetic and natural fluid inclusions induced the authors to suggest that synthetic fluids shifted to higher $^{13}C/^{12}C$ ratios due to the possible interaction with the host mineral. Moreover, the relatively excellent reproducibility obtained for the natural fluid inclusions $^{13}C_{CO2}/^{12}C_{CO2}$ area ratios has been explained as the results of the improved analytical equipment. According to the authors, however, gains in terms of analytical reproducibility can be further obtained by improving the experimental techniques to produce synthetic fluid inclusions having higher dimensions to use as standards for accurately characterising the $\delta^{13}C_{CO2}$‰ values within the natural samples.

In 2007, Arakawa and co-authors (Arakawa et al., 2007) synthesized many CO_2 fluids with different $^{13}C_{CO2}/^{12}C_{CO2}$ ratios and known $\delta^{13}C_{CO2}$ isotopic compositions ($\delta^{13}C_{CO2}$ ranged from -31.5‰ to 1493‰) to use as standards for the calibration of the method. For each fluid with different carbon isotopic compositions, a variable number of Raman spectra have been collected by mean of a 514 nm

Ar+ ion laser source, powered at 20 mW. Several spectra of 20 s each have been acquired in the same focal point, and numerically integrated to produce a $^{13}CO_2$ peak with intensity higher than 4000 counts. The authors found that, with this configuration, other than the carbon isotopic composition of the fluid itself, the intensity ratio reproducibility was affected by the measurement environment factors such as room temperature oscillations, the grating centre position, and the stability of the excitation laser power. In contrast, the fluid density effect was negligible. Based on this, the attained reproducibility of the intensity ratios resulted in being equal to ±5‰ (1σ), allowing the discrimination among biogenic and abiogenic carbon reservoirs with an error on the $\delta^{13}C_{CO2}$ estimation of about 20‰.

Years later, the research group of Li and co-authors (Li et al., 2016, 2017 and 2018) made several experiments on synthetic binary mixtures of CO_2 and N_2, with different $^{13}C_{CO2}$ and $^{12}C_{CO2}$ carbon molar concentration and known $\delta^{13}C_{CO2}$‰ values ($\delta^{13}C_{CO2}$‰ from 31926‰ to 176980‰). The binary mixtures have been prepared in order to estimate the Raman quantification factors ($F_i = \sigma_i * \zeta_i$; where σ is the wavelength-dependent Raman scattering cross-section, and ζ the instrumental efficiency of the i gas specimen within the mixture; cf. Wopenka and Pasteris, 1987) of the $^{12}CO_2$ and the $^{13}CO_2$ components within the mixture. F_i is the proportionality constant which relates the band area of a specific gas species to the relative amount of molecules of the same gas within the system, and it varies for each gas depending on the excitation laser used to perform the Raman analyses (Schrötter and Klöckner, 1979; Dubessy et al., 1989; Burke, 2001). Calculated F_{12CO2} and F_{13CO2} have been used to convert ($^{13}CO_{2\ v1}$ + $^{13}CO_{2\ v2}$)/($^{12}CO_{2\ v1}$ + $^{12}CO_{2\ v2}$) area ratios measured in Raman spectra to $^{13}C_{CO2}/^{12}C_{CO2}$ molar fraction ratios, which, in turn, have been used to obtain the $\delta^{13}C_{CO2}$‰ isotopic composition. Raman spectra have been collected first by mean of a 785 nm Ar laser source (Li et al., 2016), and successively with a 532 nm Nd laser source (Li et al., 2018). For each gas mixture, an average of 30 scans of 20 s each has been performed. The proposed method was then adopted to calculate $\delta^{13}C_{CO2}$‰ values for natural CO_2 gas samples. Results were comparable to those measured by mean of IRMS (Isotope Ratio Mass Spectrometer) analyses, demonstrating that the proposed methodology can calculate C_{CO2} isotopic ratio with high precision.

From the observations made by Arakawa et al. (2007), Yokokura et al. (2020) focussed on the factors affecting the reproducibility of $^{13}CO_2/^{12}CO_2$ intensity and area ratios. In particular, their work compared the intensity and area ratios degree of reproducibility, and concentrated on the factors affecting bands intensity and shapes, such as the pressure dependence of the fluid Raman spectrum and the grating centre position. Raman spectra have been acquired on synthetic CO_2 fluids at different pressures (10, 25, 50, 100, and 150 MPa), having known $\delta^{13}C_{CO2}$‰ isotopic composition ($\delta^{13}C_{CO2}$‰

= -11.13±0.014‰). At each fluid pressure, 5 spectra have been acquired by mean of a 532 nm Nd laser source, powered at 63 mW (17 mW at the sample surface) for prolonged acquisition times (6000 s). The reproducibility of both the measured $^{13}CO_2$ ν_1/$^{12}CO_2$ ν_1 intensity and area ratios varied based on the fluid pressure, being comprised between 2.8-8.7‰ and 4.5-14.7‰, respectively. Area ratios resulted in being less reproducible than the intensity ones. Thus, the authors concluded that the intensities of the bands could determine the C_{CO2} isotopic composition more precisely compared to the areas of the bands, with an uncertainty on the $\delta^{13}C_{CO2}$‰ less than 8.7‰ (allowing the discrimination between biogenic and abiogenic carbon). Moreover, the authors assessed that, at adopted conditions, changes of pressures or grating centre positions had a negligible effect on the intensities and the shapes of the bands. At the same time, the ratios seemed to change based on the fluid density, suggesting an engendering role of this parameter on their reproducibility.

All these works demonstrated the possible applicability of Raman spectroscopy for the C_{CO2} isotopic composition calculations in single fluid inclusions. However, due to:

(i) the limitations of the experimental techniques and the lack of standards at that time (Marshall et al., 1994);
(ii) the effects related to the measurement environment factors (Arakawa et al., 2007);
(iii) the pressure-dependence of the intensity or area ratios (Yokokura et al., 2020);

none of these works could discriminate the fluid carbon source with more precision than that necessary to distinguish between biogenic or abiogenic carbon. Such precision is too low to compete with classical bulk techniques (mass-spectroscopy), limiting the benefits of applying Raman spectroscopy for CO_2 geochemical analyses.

One of the possible explanations of the precision achieved by Arakawa et al. (2007) and Yokokura et al. (2020) for the Raman-based C_{CO2} isotopic composition could reside on the choice these authors made to relate the $^{13}CO_2$ ν_1 /$^{12}CO_2$ ν_1 intensity ratios to the $\delta^{13}C_{CO2}$‰ values, rather than the area ones. Although the intensity of a particular gas species is proportional to the number of molecules of that gas within the system (i.e., Placzek's polarizability theory), measurements of Raman band intensities are more sensitive to variations of the analytical factors (i.e., the inherent Raman scattering efficiency of a molecule, the molecular interactions, the wavelength-dependent efficiency of the instrument, and the external environmental conditions) and setups (Bernstein and Allen, 1954, and references therein; Seitz et al., 1993, and 1996; Yuan and Mayanovich, 2017). This directly affects the precision with which the intensity of the considered Raman band is measured and reflects on the precision of the measured amounts of the gas within the system. This could constitute a limitation for the application of Raman spectroscopy for the calculation of the C_{CO2} isotopic composition.

Intensity variations could be minimised by relating the measured Raman band intensity with the Raman bandwidth (i.e., the full width at half maximum, FWHM) through the *"real band intensity"*, defined as the product of measured band intensity and FWHM (Bernstein and Allen, 1954). This relation, which at a first approximation can be expressed with the band area after fitting, allows constraining the band intensity to the band shape in a bi-dimensional space, reducing the uncertainties related to intensity measurements alone (Bernstein and Allen, 1954; Yuan and Mayanovich, 2017). This suggests that the *"real band intensity"* and, thus, the band area is a more precise measure of the amount of a gas component within the fluid inclusions. For this reason, it is advisable to use $^{13}CO_2$ ν_1/$^{12}CO_2$ ν_1 area ratios to calculate $\delta^{13}C_{CO2}$‰ values by mean of Raman spectroscopy.

The adoption of the $^{13}CO_2$ ν_1/$^{12}CO_2$ ν_1 intensity ratios rather than the area ratios alone, however, is not a sufficient reason to explain Arakawa et al. (2007) and Yokokura et al. (2020) C_{CO2} isotopic composition measurements precision. Yokokura et al. (2020) demonstrated that area ratios were characterised by relatively low reproducibility, worse than that characterising the intensity ratios at comparable fluid pressures. This suggests that other factors should have negatively influenced the quantification reliability of the $^{13}C_{CO2}$ and $^{12}C_{CO2}$ isotopic concentrations. The $^{13}C_{CO2}$/$^{12}C_{CO2}$ isotopic concentration precision, and, thus, the area ratio precision in CO_2 Raman spectra, required to discriminate among different Earth reservoirs must be at the fourth decimal place ($\delta^{13}C_{CO2}$‰ precision of units ‰; Hayes, 2004; Zare et al., 2009; Sharp, 2017). Since in natural systems, the $^{13}C_{CO2}$ isotopologue corresponds to 1.1% of the total C_{CO2}, the intensity and the area of the $^{13}CO_2$ ν_1 is low with respect to the $^{12}CO_2$ ν_1 one (Fig.2). This may induce uncertainties reflecting on the quality of the fit of the band. Any sample-generated and instrumental generated perturbations affecting the $^{13}CO_2$ ν_1 band shape requires further investigations.

Other considerations are required regarding the methodology proposed by Li et al. (2016, 2017, and 2018). The authors did preliminary obtained precise $\delta^{13}C_{CO2}$‰ values by mean of Raman spectroscopy. However, $^{13}CO_2$/$^{12}CO_2$ area ratios have been calculated by considering both the CO_2 ν_1 and ν_2 for both the isotopologues. Although this approach has been considered as theoretically more precise from the operative point of view (Burke, 2001), in Raman spectra of CO_2 fluids having natural $^{13}C_{CO2}$/$^{12}C_{CO2}$ ratios, the $^{13}CO_2$ ν_2 is overlapped and, thus, hidden by the more intense $^{12}CO_2$ ν_2-related hot band (at 1264 cm^{-1} at ambient conditions; Gordon and McCubbing, 1966). Although a statistic software like Origin 6.0 has been used for bands isolation and fitting, it is not clear how the authors have managed to obtain the $^{13}CO_2$ ν_2 area value with the sufficient accuracy required for the $^{13}CO_2$ ν_1/$^{12}CO_2$ ν_1 area ratios to be representative for the $\delta^{13}C_{CO2}$‰ of the analysed fluids (Yokokura

et al., 2020). The lack of description of the parameters used to obtain the area of the $^{13}CO_2$ ν_2 does not make it possible to use the proposed method in other laboratories.

3.3 Analytical problems

The application of Raman spectroscopy for quantitative or semi-quantitative studies (i.e., calculation of CO_2 fluid density by mean of the Raman densimeters; calculation of the molar fraction of the gas components within fluid inclusions; calculation of the $^{13}C_{CO2}$ and $^{12}C_{CO2}$ concentrations for Raman-isotopic analyses) requires high precision measurements of band positions and areas (Wopenka and Pasteris, 1986; Pasteris et al., 1986, and 1988; Dubessy et al., 1989; Burke, 2001; Dubessy et al., 2012). In particular, when band positions are acquired in order to monitor the variation of fluid physical parameters such as the density, the precision should be 0.05 – 0.1 cm^{-1}, while, in the case of an application for isotopic studies, the precision of measured areas should be at the fourth decimal place (Hayes, 2004; Zare et al., 2009; Dubessy et al., 2012; Sharp, 2017; Yuan and Mayanovic, 2017).

Many factors influence the precision with whom band positions and areas can be measured and are:

(i) Spectral resolution;

(ii) Noise sources;

(iii) Raman spectra baseline correction and bands fitting;

(iv) Linear calibration of the spectrometer;

These will be briefly described in the following paragraphs.

3.3.1 Spectral resolution

The precision with which band positions and areas could be measured is closely related to the intensity and the width of the considered bands, defining their shape (Yuan and Mayanovic, 2017). This latter, in the first place, is determined by the spectral resolution, defined as the ability of the spectrometer to separate two neighbouring Raman lines, λ and $\lambda+\Delta\lambda$ (Dubessy et al., 2012). Spectral resolution controls the amount of measured Raman shifts per pixel (cm^{-1}/px; i.e., the amount of measured Raman shifts within a single-pixel or the laser dispersion) and contributes to the definition of the graphical shape of the band in terms of the number of points sampled per cm^{-1}. Spectra resolution and, consequently, the spectral per pixel resolution, depends on five main instrumental parameters (Adar, 2013):

(i) the spectrometer focal length;

(ii) the diffraction grating;

(iii) the size of the slit;

(iv) the laser wavelength;

(v) the number of pixels of the detector.

The spectrometer focal length and the number of pixels of the CCD detectors of Raman systems of the last generation are fixed and equal to 800 mm and 1024*256 px, respectively. Thus, the significant contribution to spectral resolution is given by diffraction gratings, slit width, and the laser wavelength. Among these, diffraction gratings are the most relevant parameters controlling the graphical resolution of the Raman spectra. The number of grooves of the diffraction gratings and the number of pixels of the CCD detector directly define the spectrometer resolution in Raman shift per pixel (McCreery, 2000; Dubessy et al., 2012). The most commonly used diffraction gratings are characterized by different numbers of grooves per millimetre, from 600 to 3200 gr/mm (Adar, 2013): the higher the number of the grooves per millimetre, the higher the amount of the laser dispersion and, thus, the definition of the shapes of the bands within the spectrum (Horiba Scientific website; Adar, 2013).

When equal diffraction gratings are used for the analyses, the spectral resolution can be further improved by choosing the laser wavelength and the slit width aperture. Both these parameters contribute to the amplitude of the Raman scattering cross-section and the laser band-pass, and thus, on the direct response of the analysed material and on the amount of signal which is dispersed by the diffraction grating on the sample. Lower laser wavelengths and/or smaller slit width apertures, higher are the Raman scattering cross-sections and lower the bands-pass, thus, higher the spectral resolution (McCreery, 2000; Dubessy et al., 2012; Adar, 2013).

3.3.2 Noise sources

Straightforwardly, the noise is defined as that part of the spectrum carrying unwanted information originating from a random fluctuation of the Raman signal intensities (Pelletier, 2003). The noise (σ_y) is made by five components, and it is expressed as [Eq.6] (McCreery, 2000):

$$\sigma_y = (\sigma_S^2 + \sigma_B^2 + \sigma_d^2 + \sigma_F^2 + \sigma_r^2)^{1/2} \quad \text{[Eq.6]}$$

where σ_S is the shot noise, σ_B is the background noise, σ_d is the dark signal noise, σ_F is the flicker noise, and σ_r is the readout noise.

Among these, the σ_S, the σ_B, the σ_d, and the σ_r noises contribute to negatively affect the resolution of the shape of the bands in Raman spectra:

- σ_S (shot noise): is the result of the inconsistent intensity of photons collected per pixel per unit of time and is governed by a Poisson distribution. The shot noise is an unescapable random source of noise in Raman spectra and cannot be excluded from the signal (Pelletier, 2003). The only way to minimise the effects of the shot noise is to collect a higher number of photons; this can be accomplished by increasing the slit width and the confocal hole apertures or by adopting prolonged acquisition times. However, these changes in the analytical setting are responsible for increasing other noise sources such as the instrumental generated background noise or the dark signal noise (McCreery, 2000; Pelletier, 2003; Dubessy et al., 2012; Barton et al., 2016).
- σ_B (background noise): is the random Raman bands intensity variations caused by sample (sample generated background noise; i.e., sample physical characteristics, fluorescence, thermal emissions; McCreery, 2000; Pelletier, 2003; Barton et al., 2016) and by laser changes (instrumental generated background noise; i.e., thermal heating of the optics, laser line reflections due to the optics or due to dust on the samples; McCreery, 2000; Pelletier, 2003; Barton et al., 2016). In Raman spectra of fluid inclusions, the most common causes generating background noise effects are:
  (i) the host mineral: minerals having high refractive indexes (i.e., garnet or olivine), or being fluorescent, contribute to reducing (i.e., worsening) the signal to noise ratio of the fluid inclusions Raman scattering (Burke, 2001; Pelletier, 2003; Caumon et al., 2015, and 2019);
  (ii) sizes, depths and habits of the analysed fluid inclusion: fluid inclusions with variable sizes and habits can be trapped at various depths within the host minerals. Smaller fluid inclusions and/or higher depths within the sample and/or irregular shapes directly affect the amount of laser which can successfully reach and excite the analysed fluid molecules compared to the surrounding host mineral. This influences the scattered Raman radiation which comes back from the sample to the CCD detector and, thus, the fluid molecules signal to noise ratio in the spectrum (Dubessy et al., 1989; Burke, 2001; Fukura et al., 2006; Frezzotti et al., 2012a; Dubessy et al., 2012; Remigi et al., 2021);
  (iii) presence of metastable phases within the fluid inclusions (i.e., presence of bubbles in liquid fluid inclusions, which can move during the analyses due to the laser heating);
  (iv) fluid inclusion compositions and presence of gas mixtures: molecular interactions between two or more gas components can originate local order/disorders effects, which affects the strength of the chemical bonds of the molecules composing the system, modifying the shape

of the Raman bands. This lead to incorrect band positions or areas measurements (Pelletier et al., 2003; Le et al., 2019);

(v) the density of the fluid and temperature variations: as with the fluid inclusion composition, these factors can originate changes in the strength of the molecular bonds and, in turn, the gas phase Raman scattering. This lead to the decrease of the signal to noise ratio in the Raman spectrum (Dubessy et al., 1989; Seitz et al., 1996; Pelletier, 2003; Le et al., 2019; Sublett et al., 2019)

Reducing the confocal hole aperture, with the consequent extension of the spectra acquisition times, and the adoption of large magnifications are effective ways to reduce the sample background noise but can originate instrumental background noise effects. Thus, similar noises cannot be eliminated entirely from the Raman spectra (McCreery, 2000; Burke, 2001; Pelletier, 2003; Frezzotti et al., 2012a).

- σ_d (dark signal noise): is the spontaneous thermal generation of electrons within the CCD detector during analyses. Changes in temperatures can be recorded on the CCD detectors during the analyses during the laser heating (McCreery, 2000; Pelletier, 2003; Barton et al., 2016);
- σ_r (readout noise): is the standard deviation associated with the digital conversion of scattered electrons from the detector to the spectrum. The readout noise is inherent in every signal acquisition, and it is independent by the laser or the magnitude of the scattered radiation reaching the CCD detectors (McCreery, 2000; Pelletier, 2003; Barton et al., 2016).

3.3.3 Raman spectra baseline correction and bands fitting

The uncertainties in the measurements of band shapes, and, thus, bands positions and areas, originated by the noise effects on the raw Raman spectra, can be mitigated by spectral processing. Raw spectra can be processed through baseline removal and band fitting (Pelletier, 2003; Yuan and Mayanovic, 2017). The shape of the baseline is determined by the sum of all the noise components. Nowadays, automated baseline correction software is present to identify the points of the spectrum that belong to the Raman bands and fit the remaining ones with appropriate baseline functions (Stellman et al., 1995; Pelletier, 2003). These, however, can be responsible for the generation of a secondary or external source of noises by producing new functions oscillating around the real background value they are trying to remove (Pelletier, 2003). In many cases, manual baseline removal performed by the users, by specifying those background points which should be equal to zero, are preferred; despite manual baseline-correction could be affected by bias introduced by operators, the function which is generated to fit the specified points to be removed is forcibly less sensitive to

oscillations of the background values (McCreery, 2000). Once the baseline has been removed, the fitting of the remaining Raman bands by mean of the most appropriate fitting curve should be performed in order to obtain bands parameters like positions, intensities, shapes, and areas with improved accuracy of about 30 times (Yuan and Mayanovic, 2017, and references therein).

Raman band profiles depend on the perturbation of the vibrational modes due to molecular interaction (Dubessy et al., 2012). For Raman quantitative and semi-quantitative analyses of gas phases, the symmetric stretching modes are characterised by asymmetric band profiles, resulting from the sum of a Gaussian and a Lorentzian curve (i.e., Pseudo-Voigt behaviour; Dubessy et al., 2012; Yuan and Mayanovic, 2017). The Gaussian component of the symmetric stretching profile increases with the increasing ratio of spectral resolution/FWHM, inducing an enlargement of the band at the base and a decrease in intensity at the peak maximum (Dubessy et al., 2012). For this reason, to perform precise measures of band positions and areas, gas profiles should be fitted using a Pseudo-Voigt fitting curve. However, for symmetric Raman bands characterised by "apparent" asymmetries on the shapes of the bands due to the overlapping of the signals (e.g., $^{13}CO_2$ ν_1 and the $^{12}CO_2$ ν_1; Irmer and Graupner, 2002; Hurai et al., 2015), fitting by mean of a Pseudo-Voigt profile can lead to imprecise measurements. In similar cases, fitting curves for asymmetric Raman bands should be used, as the Pearson VII profile (Yuan and Mayanovic, 2017). Much fitting software (e.g. Fityk), however, implement a Split Pseudo-Voigt fitting algorithm which allows the processing of symmetric Raman bands affected by "apparent" asymmetries (Wojdyr, 2010). These profiles can improve the accuracy of bands parameters (Weber et al., 1997; Pelletier, 2003; Wojdyr, 2010; Yuan and Mayanovic, 2017).

3.3.4 Linear calibration of the spectrometer

The relation between the grating, the CCD detector pixels and the Raman shift is generally a straight line, described by the general equation $y = mx + q$ (Dubessy et al., 2012). The presence of a slope in this equation leads to an apparent non-linear behaviour of the Raman spectrometer monochromator. Thus, adrift in the positions of the bands from their theoretical wavenumber is observed, particularly for those vibrations far from the calibrated wavenumber region (Lin et al., 2007; Lamadrid et al., 2017). The instrumental linearity, above all, depends on the variations of the laboratory environmental conditions and, in particular, by the temperature (McCreery et al., 2000; Fukura et al., 2006; Lin et al., 2007). Changes of less than 1°C during the analytical session could affect the mechanics of the Raman systems, leading to the apparent non-linear behaviour of the spectrometer (Lin et al., 2007). This can be easily corrected by calibrating the system with apposite standards, whose vibrations cover the spectral range of interest, and perform analyses under

controlled and constant room temperature (McCreery et al., 2000; Fukura et al., 2006; Lin et al., 2007).

4. ANALYTICAL METHODS

For the present work of the thesis, the characterisation of CO_2 fluids has been carried out on previously studied fluid inclusions (cf. Appendix section, paragraph 9.1; Frezzotti et al., 2010, and 2012b; Oglialoro et al., 2017) by using microthermometry and Raman micro-spectroscopy.

An additional collection of data on the bulk isotopic signature of CO_2 fluid inclusions and advanced statistical treatment of data distributions, which has served for the preparation of the presented manuscripts, has also been carried out by several co-authors, and, in particular:

(i) Bulk calculation of the $\delta^{13}C_{CO2}$‰ values of studied CO_2 fluid inclusions have been performed by A. L. Sandoval-Velasquez, A. L. Rizzo and A. Aiuppa, at the Laboratorio degli isotopi dei gas nobili e degli isotopi stabili, Istituto Nazionale di Geofisica e Vulanologia (INGV), Sezione di Palermo;

(ii) Statistical analyses based on the bootstrapping approach have been performed by T. Mancini, at the Department of Economic, Social and Political Science, University of Southampton.

In the following paragraphs, a summary of the primary methodologies (i.e., microthermometry and Raman micro-spectroscopy, which had a central role in the present work) and of fluid inclusions selected for the analyses are reported.

4.1 Microthermometry

Microthermometry allows observing the phase transitions with changing temperature (heating) of the fluid within fluid inclusions. The temperatures where fluid phase transitions occur are distinctive for the chemical composition and the density at trapping conditions of the analysed fluids.

Microthermometric analyses on heating allow to record different phase transition temperatures:

(i) The temperature of melting, Tm for pure gas systems (e.g., pure CO_2): instantaneous disappearance of the solid phase and appearance of the liquid one;
(ii) First melting Te (eutectic) or Ti (initial) temperature for mixtures of two or more gases: the appearance of the first liquid occur;
(iii) The temperature of homogenization into the liquid ThL (L+V→L): shrinkage of gas bubble;
(iv) The temperature of homogenization into the vapour ThV (L+V→ L): expansion of gas bubble;
(v) The temperature of sublimation Ts (S+V→V).

Figure 4 shows the projection of CO_2 pure systems in a P-T space. The system is characterised by the presence of three univariant curves for coexisting, LV, SL, and SV, which separates the three-phase stability fields for solid (S), liquid (L), and vapour (V) CO_2 (Van den Kerkhof and Thiery, 2001).

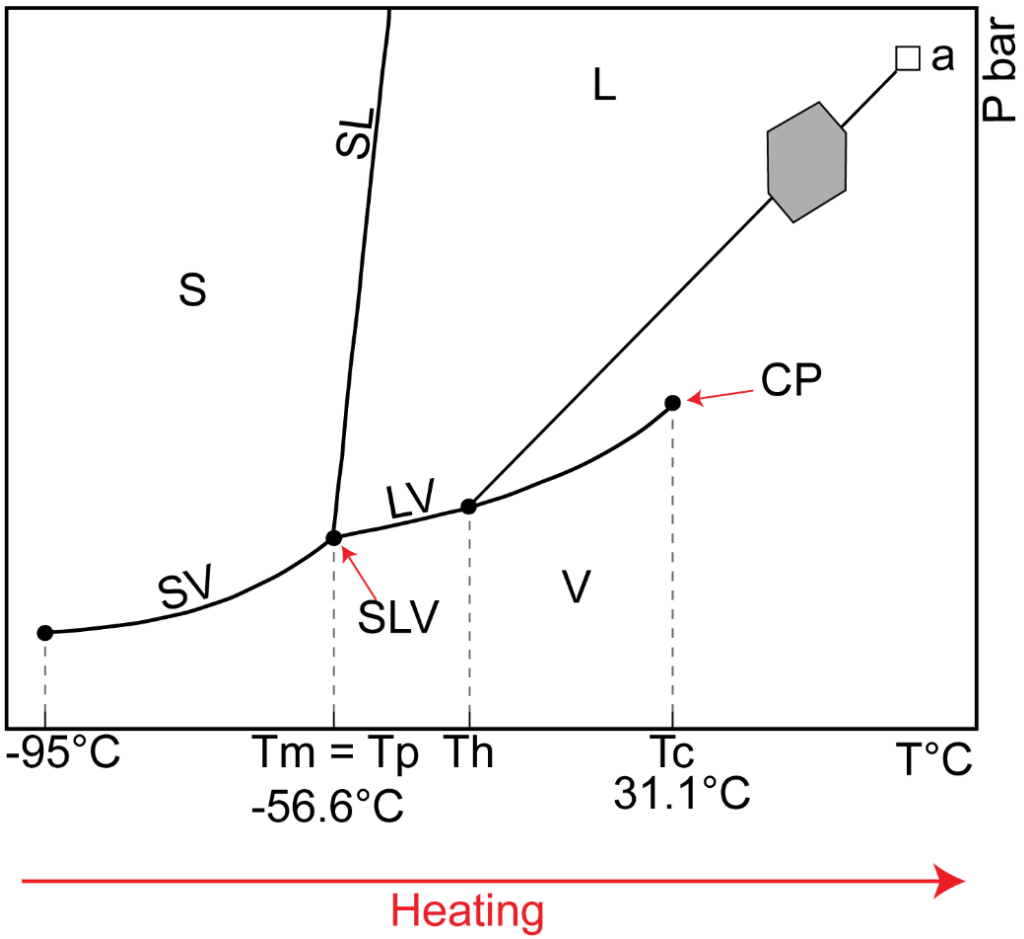

Fig.4 Schematic phase diagram describing CO_2 fluid inclusion (grey filled icon), trapped at P-T condition of a, phase transitions on heating, modified after Van den Kerkhof and Thiery, 2001. T = temperature; P = pressure; Tm = melting temperature; Tp = invariant triple point; Th = homogenization; Tc = critical temperature; S = solid stability field; L = liquid stability field; V = vapour stability field; SV = coexisting S+V univariant curve; SL = coexisting S+L univariant curve; LV = coexisting L+V univariant point; SLV = coexisting S+L+V invariant point; CP = critical point.

On heating, CO_2 phase transitions occur between -95°C (CO_2 solidification) and -31.1°C (CO_2 critical temperature). On heating, solid CO_2 instantaneously melts at the triple point -56.6°C (Tp), which is coincident with CO_2 melting temperature (Tm). Increasing the system temperature fluid homogenization occurs at Th in the liquid or vapour phases (Van den Kerkhof and Thiery, 2001). For the specific case of the fluid inclusions shown in figure 4.1, homogenization occurs in the liquid phase

(ThL). Recorded Th can be directly related to the CO_2 density at trapping conditions and, in turn, to the minimum trapping pressure conditions.

For the present work of thesis, microthermometric measurements of CO_2 fluid inclusions have been performed using a Linkam THM 600 heating-freezing stage system, coupled with a Leitz petrographic microscope (50X objective) at the Università degli Studi di Milano - Bicocca. The system is equipped with a silver cylinder characterized by a central hole for the light, a single cone trunk shaped crystal, surrounded by resistance, and it is provided with a monitoring sensor for the temperature and many tubes for the circulation of the liquid nitrogen. The cylinder is covered by a second cylindrical block, constituting the upper part of the sample compartment. The system is enclosed into a hermetically closed chamber, located on the sample holder of an optical microscope, characterized by long-distance magnifications

The system has been calibrated by the double-checking of H_2O and CO_2 triple points (Tp), respectively at 0.015°C and -56.6°C, by mean of synthetic standards SYNFLINC, with an error of ±0.1°C. Daily controls on the CO_2 triple point (Tp) have additionally been performed before starting the analyses. Temperatures of phase transition have been recorded through several freezing-heating cycles, with heating rates variable from 0.1 to 0.5°C/min in the temperature intervals close to phase transitions. Measured homogenization temperatures both to the liquid (ThL) and vapour phase (ThV) have been used to calculate densities by mean of the freeware software BULK (Bakker, 2003), by adopting the CO_2 equation of state of Duschek et al. (1990). The error on CO_2 densities was ± 0.01 g/cm^3.

4.2 Raman micro-spectroscopy

Over the past few decades, Raman spectroscopy has become a commonly used technique in the study of fluid inclusions since it allows non-destructive and in situ chemical and semi-quantitative characterisation of fluid samples with a minimum spatial resolution of about 1 μm (Delhaye and Dhamelincourt, 1975; Rosasco et al., 1975; Dhamelincourt et al., 1979; Dubessy et al., 1982, and 1989; Pasteris et al., 1986, and 1988; Seitz et al., 1987; Burke, 1994, and 2001; Burruss, 2003; Frezzotti et al., 2012a; Bodnar and Frezzotti, 2020). Raman spectroscopy is based on the inelastic scattering of light through the sample (known as the Raman effect; Raman, 1928), first discovered by the Indian physician C.V. Raman in 1928 (Raman, 1928). The Raman inelastic scattering of the light can be described based on the quantum mechanical model as the result of energy transfer between the incident light and the molecules (Colthup et al., 1975; Nasdala et al., 2004; Frezzotti et al., 2012a and references therein; Hurai et al., 2015 and references therein). Within a sample, the molecules could

have different vibrational states, separated by a quantum of energy. The collisions between the incident light photons, having frequency ν_1, induce a momentaneous increase of the molecules vibrational energy to a virtual high-energy state. The recovery of the system after the excitation occurs by the emission of diffuse scattering of the light, which can be elastic (i.e., Rayleigh-type scattering; the diffuse scattering of light has the same frequency ν_1 of the incident light), or inelastic (i.e., the diffuse scattering of light has lower, ν_1-ν_m, or higher, ν_1+ν_m, energy in respect than that of the incident light, where ν_m is the molecule fundamental frequency). The decreasing of the frequency of the diffuse light (ν_1-ν_m) originates the Stokes-type scattering, while the increasing of the frequency (ν_1+ν_m) the anti-Stokes one (Nasdala et al., 2004; Frezzotti et al., 2012a and references therein).

Raman spectroscopy measures the photons arising from the inelastic scattering of light through the sample, expressed in a Raman spectrum by the plot of the light intensity, generally given as counts or arbitrary units, and the energy of the photon, conventionally given as wavenumbers, $\tilde{\nu}$, in cm^{-1}, and expressed by [Eq.7]:

$$\tilde{\nu} = \frac{\nu}{c} = \frac{1}{\lambda} \qquad \text{[Eq.7]}$$

where ν is the frequency of the photon, c the speed of the light and λ the light wavelength.

Generally, only the Stokes-type scattering relative to the vibrational modes of analysed molecules is recorded within the Raman spectra since their higher intensity than the anti-Stokes one. Recorded scattered frequencies consists of one or more bands whose wavenumbers strictly depends on the structure and the bonding nature of the analysed molecules, thus, constituting a fingerprint to qualitatively discriminate among different samples (Nasdala et al., 2004; Frezzotti et al., 2012a and references therein; Hurai et al., 2015 and references therein).

The Raman spectra of natural CO_2 fluid inclusions have been acquired by mean of two Raman systems:

(i) Horiba Jobin Yvon LabRAM HR Evolution Raman System (focal length 800 mm; Fig.5) at the Laboratorio di micro-spettroscopia Raman, Dipartimento di Scienze dell'Ambiente e della Terra, Università di Milano – Bicocca. This system is connected to an air-cooled 1024*256 px CCD detector and a wheel of nine neutral density filters. The system is further provided by two diffraction gratings (600 and 1800 gr/mm) and a green 532 nm Nd laser source (power of 300 mW). It is also equipped with an Olympus BXFM microscope, allowing observations in transmitted and reflected light.

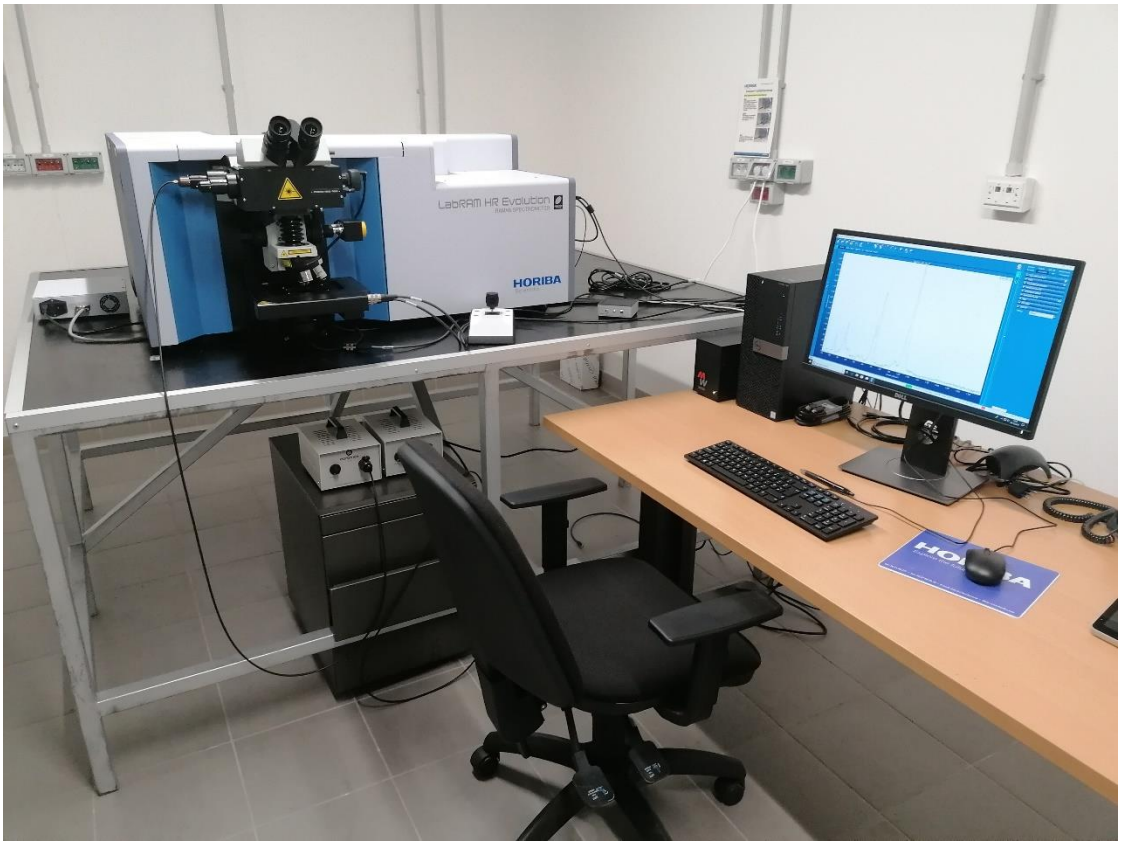

Fig.5 Photograph of the Horiba Jobin Yvon LabRAM HR Evolution Raman System, Laboratorio di micro-spettroscopia Raman, Dipartimento di Scienze dell'Ambiente e della Terra, Università degli Studi di Milano-Bicocca, adopted for CO_2 spectra acquisitions.

(ii) Horiba Jobin Yvon LabRam HRVIS Raman System (focal length 800 mm; Fig.6) at the Centro "G. Scansetti", Dipartimento di Scienze della Terra, Università di Torino. This system is connected to an air-cooled 1024*256 px CCD detector and a wheel of six filters for laser attenuation. It is also provided with two laser sources, a green 532 nm Nd laser source (power of 250 mW) and a red 633 nm HeNe one (power of 20 mW) and two diffraction gratings (600 and 1800 gr/mm). The system is also provided with an Olympus BX41 microscope for petrographic observations in both transmitted and reflected light. In order to analyse CO_2 fluid inclusions with densities lower than 0.74 and higher than 0.22 g/cm^3, characterized by the coexistence of vapour (V) and liquid (L) phases at room temperature (18°C), the spectrometer has also been equipped with a Linkam THM 600 heating-freezing stage. Inclusions have been analyzed at a temperature of 32°C (above the CO_2 critical T at 31.1°C) at ambient pressure.

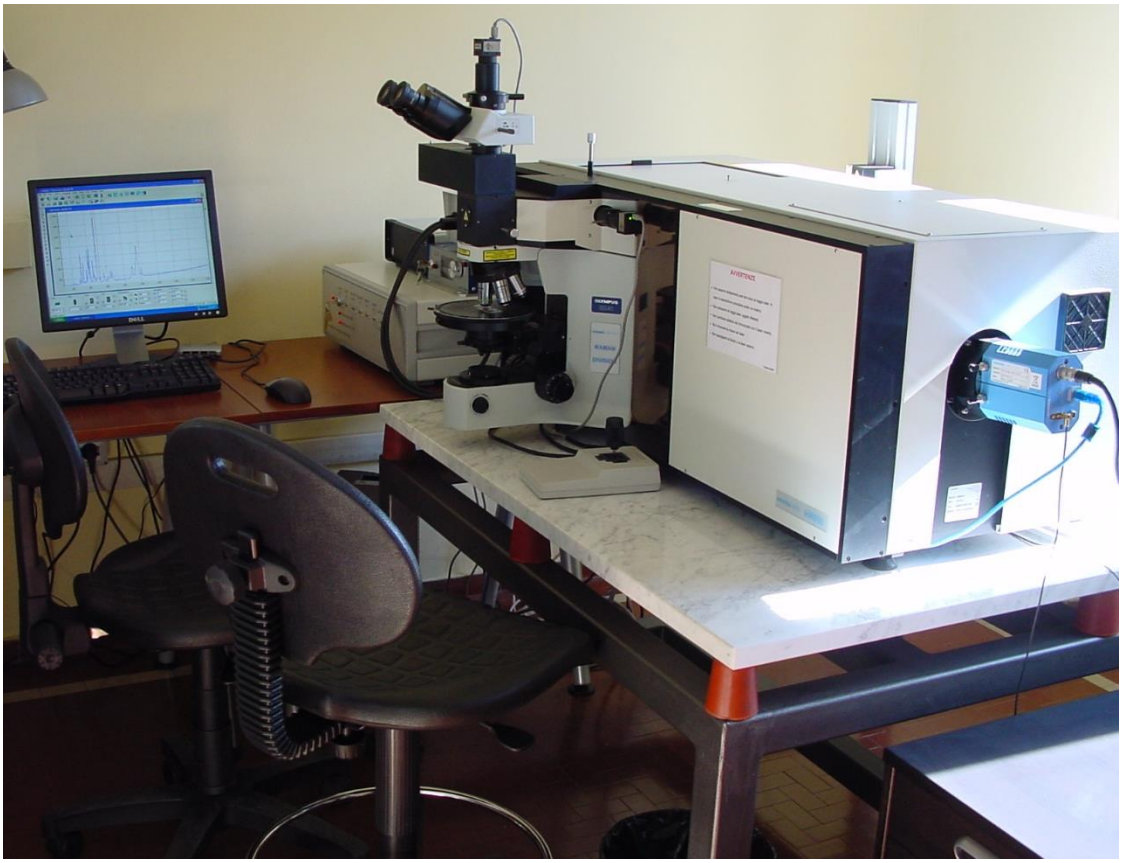

Fig.6 Photograph of the Horiba Jobin Yvon LabRam HRVIS Raman System, at the Centro "G. Scansetti", Dipartimento di Scienze della Terra, Università di Torino, adopted for CO_2 spectra acquisitions.

For both systems, the instrumental calibration has been daily checked. For the Horiba Jobin Yvon LabRAM HR Evolution Raman System, calibration has been carried out through the automatic auto-calibration process performed by the Ryman system Service in respect to the zero lines and the silicon standard. During the process, the Raman system Service checks also the linearity of the spectrometer and corrects any drift of the measured band positions, automatically reporting the measured *Koeff* value to that calculated after the calibration during the installation of the system, based on material standards having two or more well-known peaks (i.e., Ne emission lamp, Naphthalene, Benzonitrile). For the Horiba Jobin Yvon LabRam HRVIS Raman System, instead, calibration has been carried out concerning the zero line (the Rayleigh line, i.e., the laser wavelength) with a synthetic diamond standard (vibration at 1331.83 cm^{-1}), according to the ASTM 1840 – 96 (2007) normative (Hutsebaut et al., 2005; ASTM 1840 – 96 [2007] normative). The spectrometer linearity has been further checked through the position of the central band of the silicon standard (vibration at 520.70 cm^{-1}), and corrected by adjusting the *Koeff.* parameter in the Labspec 5 software, as recommended by Lamadrid et al. (2017).

Raman micro-spectroscopic analyses on CO_2 fluid inclusions have been carried out in order to calculate CO_2 fluid densities by applying the Raman densimeter method (cf. chapter 3, paragraph 3.2.1), and to quantitatively estimate the molar fractions of the $^{13}CO_2$ and the $^{12}CO_2$ isotopologues (cf. chapter 3, paragraph 3.2.2). According to Remigi et al., 2021, the density of CO_2 fluid inclusions has been calculated by the mean of Fall et al. (2011) Raman densimeter, allowing to investigate CO_2 fluid inclusions in the density range between 0.24 to 1.08 g/cm^3 for spectra acquired by high spectral per pixel resolution analyses (i.e., 0.33 cm^{-1}/px).

4.3 Fluid inclusions selected for the analyses

CO_2 fluid inclusions selected for the present work of thesis were preserved in Ol I and II, Opx I and II and Cpx from five mantle xenoliths from El Hierro, Canary Islands (samples XML3, 6, 7, 9, and 11; cf. Oglialoro et al., 2017), and in Ol I and Opx I from seven mantle xenoliths from the Lake Tana region (samples INJ4, 7, 16, 18, 34, 35, and 39, Ferrando et al., 2008; cf. Appendix section, paragraph 9.1; Frezzotti et al., 2010, and 2012b; Oglialoro et al., 2017).

Only CO_2 pure fluid inclusions have been analysed (cf. Appendix section, paragraph 9.1; Frezzotti et al., 2010, and 2012b; Oglialoro et al., 2017). To test the applicability of Raman micro-spectroscopy to calculate the C_{CO2} isotopic composition in single fluid inclusions, selected fluid inclusions were characterised by high density, from 0.73 to 1.07 g/cm^3, and negative crystal shapes or rounded habits. They ranged from 5 to 21 µm in size, and 5 to 19 µm in depth from the sample surface. Instead, the investigation of the CO_2 Raman densimeter method has been carried out on fluid inclusions with variable density, from 0.37 to 1.08 g/cm^3, and characterized by negative crystal shape to prismatic and rounded habits. They ranged from 2 to 20 µm in size and, when prismatic, from 1 to 5 µm in width, and were found from 8 to 43 µm in depth from the sample surface.

5. REFERENCES

Adar, F. (2013). Raman Microscopy Analysis of Molecular Orientation in Organic Fibers. *Spectroscopy*, **28(2),** 14–22.

Amat, G., Pimbert, M. (1965). On Fermi resonance in carbon dioxide. *Journal of Molecular Spectroscopy*, **16(2)**, 278-290; https://doi.org/10.1016/0022-2852(65)90123-2

Andersen, T., and Neumann, E. R. (2001). Fluid inclusions in mantle xenoliths. *Lithos*, **55(1-4)**, 301-320; https://doi.org/10.1016/S0024-4937(00)00049-9

Angus, S., Armstrong, B., and De Reuck, K. M. (1976). Thermodynamic Tables of the Fluid State: Carbon Dioxide. PergamonPress: Oxford.

Arakawa, M., Yamamoto, J., Kagi, H. (2007). Developing micro-Raman mass spectrometry for measuring carbon isotopic composition of carbon dioxide. *Applied spectroscopy*, **61(7)**, 701-705; https://www.osapublishing.org/as/abstract.cfm?URI=as-61-7-701

ASTM. (2007). E1840–96: Standard Guide for Raman Shift Standards for Spectrometer Calibration; https://www.astm.org/Standards/E1840.htm

Bakker, R. J. (2003). Package FLUIDS 1. Computer programs for analysis of fluid inclusion data and for modelling bulk fluid properties. *Chemical Geology*, **194(1-3)**, 3-23; https://doi.org/10.1016/S0009-2541(02)00268-1

Barton, S. J., Kerr, L. t., Domijan, K., Hennelly, B. M. (2016). On the effect of experimental noise on the classification of biological samples using Raman micro-spectroscopy. *Proceedings, SPIE 9887, Biophotonics: Photonic Solutions for Better Health Care V*, **98873A**; https://doi.org/10.1117/12.2227785

Bergman, S. C., and Dubessy, J. (1984). CO_2-CO fluid inclusions in a composite peridotite xenolith: implications for upper mantle oxygen fugacity. *Contributions to Mineralogy and Petrology*, **85(1)**, 1-13; https://doi.org/10.1007/BF00380216

Berkesi, M., Guzmics, T., Szabó, C., Dubessy, J., Bodnar, R. J., Hidas, K., and Ratter, K. (2012). The role of CO_2-rich fluids in trace element transport and metasomatism in the lithospheric mantle beneath the Central Pannonian Basin, Hungary, based on fluid inclusions in mantle xenoliths. *Earth and Planetary Science Letters*, **331**, 8-20; https://doi.org/10.1016/j.epsl.2012.03.012

Berkesi, M., Czuppon, G., Szabó, C., Kovacs, I., Ferrero, S., Boiron, M. C., and Peiffert, C. (2019). Pargasite in fluid inclusions of mantle xenoliths from northeast Australia (Mt. Quincan): evidence of interaction with asthenospheric fluid. *Chemical Geology*, **508**, 182-196; https://doi.org/10.1016/j.chemgeo.2018.06.022

Bernstein, H. J., Allen, G. (1954). Intensity in the Raman Effect. I. Reduction of Observed Intensity to a Standard Intensity Scale for Raman Bands in Liquids. *Journal of the Optical Society of America*, **45(4)**, 237-249; https://doi.org/10.1364/JOSA.45.000237

Bodnar, R. J. (1995). Fluid inclusion evidence for a magmatic source for metals in porphyry copper deposits. J.F.H. Thompson (Ed.), Magmas, Fluids and Ore Deposits, Mineral Association of Canada Short Course, **Vol. 23**, pp. 139-152.

Bodnar, R. J. (2001). PTX phase equilibria in the H_2O-CO_2-salt system at Mars near-surface conditions. In *Lunar and Planetary Science Conference* (p. 1689);

Bodnar, R. J., Frezzotti, M. L. (2020). Microscale chemistry: Raman analysis of fluid and melt inclusions. *Elements: An International Magazine of Mineralogy, Geochemistry, and Petrology*, **16(2**), 93-98; https://doi.org/10.2138/gselements.16.2.93

Bodnar, R. J., Lecumberri-Sanchez, P., Moncada, D., Steele-MacInnis, M. (2014). 13.5–Fluid inclusions in hydrothermal ore deposits. *Treatise on Geochemistry, Second Editionth edn. Elsevier, Oxford*, 119-142;

Burke, E. A. (1994). Raman microspectrometry of fluid inclusions: the daily practice. In Vivo, B. D. and Frezzotti, M. L.(eds.) Fluid Inclusions in Minerals: Method and Applications. Short Course of Working Group (IMA) "Inclusions in Minerals", 25–44, Virginia Polytechnic Inst. and State University

Burke, E. A. (2001). Raman microspectrometry of fluid inclusions. *Lithos*, **55(1-4)**, 139-158; https://doi.org/10.1016/S0024-4937(00)00043-8

Burruss, R. C., Samson, I. M., Anderson, A., Marshall, D. (2003). Raman spectroscopy of fluid inclusions (Vol. 32, pp. 279-289). Mineralogical Association of Canada.

Campione, M., Malaspina, N., Frezzotti, M. L. (2015). Threshold size for fluid inclusion decrepitation. *Journal of Geophysical Research: Solid Earth*, **120(11)**, 7396-7402; https://doi.org/10.1002/2015JB012086

Caumon, M. C., Tarantola, A., and Mosser-Ruck, R. (2015). Raman spectra of water in fluid inclusions: I. Effect of host mineral birefringence on salinity measurement. *Journal of Raman Spectroscopy*, **46(10)**, 969-976; https://doi.org/10.1002/jrs.4708

Caumon, M-C, Tarantola, A, Wang, W. (2019). Raman spectra of gas mixtures in fluid inclusions: Effect of quartz birefringence on composition measurement. *Journal of Raman Spectrosc*opy, **51,** 1868– 1873; https://doi.org/10.1002/jrs.5605

Chou, I. M., Pasteris, J. D., Seitz, J. C. (1989). High-density volatiles in the system COHN for the calibration of a laser Raman microprobe. *Geochimica et Cosmochimica Acta*, **54(3)**, 535-543; https://doi.org/10.1016/0016-7037(90)90350-T

Colthup, N. B. (1975). Daly, and SE Wiberley. Introduction to Infrared and Raman Spectroscopy 2rid edn. Academic Press, New York, 246.

Correale, A., Paonita, A., Rizzo, A., Grassa, F., Martelli, M. (2015). The carbon-isotope signature of ultramafic xenoliths from the Hyblean Plateau (southeast Sicily, Italy): Evidence of mantle heterogeneity. *Geochemistry, Geophysics and Geosysmic*, **16**, 600-611; https://doi.org/10.1002/2014GC005656

Dasgupta, R., Hirschmann, M. M. (2006). Melting in the Earth's deep upper mantle caused by carbon dioxide. *Nature*, **440(7084)**, 659-662; https://doi.org/10.1038/nature04612

Dasgupta, R., Hirschmann, M. M. (2007a). Effect of variable carbonate concentration on the solidus of mantle peridotite. *American Mineralogist*, **92(2-3)**, 370-379; https://doi.org/10.2138/am.2007.2201

Dasgupta, R., Hirschmann, M. M. (2007b). A modified iterative sandwich method for determination of near-solidus partial melt compositions. II. Application to determination of near-solidus melt compositions of carbonated peridotite. *Contributions to Mineralogy and Petrology*, **154(6)**, 647-661; https://doi.org/10.1007/s00410-007-0214-8

Dasgupta, R., Hirschmann, M. M., and Smith, N. D. (2007). Water follows carbon: CO_2 incites deep silicate melting and dehydration beneath mid-ocean ridges. *Geology*, **35(2)**, 135-138; https://doi.org/10.1130/G22856A.1

Delhaye, M., Dhamelincourt, P. (1975). Raman microprobe and microscope with laser excitation. *Journal of Raman Spectroscopy*, **3(1)**, 33-43; https://doi.org/10.1002/jrs.1250030105

Dhamelincourt, P., Beny, J. M., Dubessy, J., Poty, B. (1979). Analyse d'inclusions fluides à la microsonde MOLE à effet Raman. *Bulletin de Mineralogie*, **102(5)**, 600-610; https://doi.org/10.3406/bulmi.1979.7309

Dickinson, R. G., Dillon, R. T., Rasetti, F. (1929). Raman spectra of polyatomic gases. *Physical Review*, **34(4)**, 582; https://doi.org/10.1103/PhysRev.34.582

Dubessy, J., Audeoud, D., Wilkins, R., Kosztolanyi, C. (1982). The use of the Raman microprobe MOLE in the determination of the electrolytes dissolved in the aqueous phase of fluid inclusions. *Chemical Geology*, **37(1-2)**, 137-150; https://doi.org/10.1016/0009-2541(82)90073-0

Dubessy, J., Caumon, M. C., Rull, F., Sharma, S. (2012). Instrumentation in Raman spectroscopy: elementary theory and practice. *In Raman spectroscopy applied to earth sciences and cultural heritage*, **12**, 83-172.

Dubessy, J., Moissette, A., Bäkker, R. J., Frantz, J. D., Zhang, Y. G. (1999). High-temperature Raman spectroscopic study of H_2O-CO_2-CH_4 mixtures in synthetic fluid inclusions: first insights

on molecular interactions and analytical implications. *European Journal of Mineralogy*, **11(1)**, 23-32; https://doi.org/10.1127/ejm/11/1/0023

Dubessy, J., Poty, B., Ramboz, C. (1989). Advances in COHNS fluid geochemistry based on micro-Raman spectrometric analysis of fluid inclusions. *European journal of Mineralogy*, **1(4)**, 517-534; https://doi.org/10.1127/ejm/1/4/0517

Duschek, W., Kleinrahm, R., Wagner W. (1990). Measurement and correlation of the (pressure, density, temperature) relation of carbon dioxide II. Saturated-liquid and saturated-vapor densities and the vapor pressure along the entire coexistence curve. *Journal of Chemical Thermodynamics*, **22(9)**, 841-864; https://doi.org/10.1016/0021-9614(90)90173-n

Fabre, D., Couty, R. (1986). Etude par spectroscopie Raman, du methane comprimé jusqu'a 3kbar. Application à la mesure de pression dand les inclusion fluids continues dans les mineraux. *Comptes Rendus de l'Académie des Sciences de Paris*, t. 303, série II, **14**, 1305-1308.

Fabre, D., Oksengorn, B. (1992). Pressure and density dependence of the CH_4 and N_2 Raman lines in an equimolar CH_4/N_2 gas mixture. *Applied spectroscopy*, **46(3)**, 468-471; https://www.osapublishing.org/as/abstract.cfm?URI=as-46-3-468

Fall, A., Tattitch, B., Bodnar, R. J. (2011). Combined microthermometric and Raman spectroscopic technique to determine the salinity of H_2O–CO_2–NaCl fluid inclusions based on clathrate melting. *Geochimica et Cosmochimica Acta*, **75(4)**, 951-964; https://doi.org/10.1016/j.gca.2010.11.021

Fermi, E. (1931). Über den ramaneffekt des kohlendioxyds. *Zeitschrift für Physik*, **71(3)**, 250-259; https://doi.org/10.1007/BF01341712

Ferraro, J.R., Nakamoto, K., Brown, C.W. (2003). Introductory Raman Spectroscopy. Elsevier, Amsterdam, 434 p.

Frezzotti, M. L., Ferrando, S. (2015). The chemical behavior of fluids released during deep subduction based on fluid inclusions. *American Mineralogist*, **100(2-3)**, 352-377; https://doi.org/10.2138/am-2015-4933

Frezzotti, M. L., Ferrando, S., Peccerillo, A., Petrelli, M., Tecce, F., Perucchi, A. (2010). Chlorine-rich metasomatic H_2O–CO_2 fluids in amphibole-bearing peridotites from Injibara (Lake Tana region, Ethiopian plateau): nature and evolution of volatiles in the mantle of a region of continental flood basalts. *Geochimica et Cosmochimica Acta*, **74(10)**, 3023-3039; https://doi.org/10.1016/j.gca.2010.02.007

Frezzotti, M. L., Ferrando, S., Tecce, F., and Castelli, D. (2012b). Water content and nature of solutes in shallow-mantle fluids from fluid inclusions. *Earth and Planetary Science Letters*, **351**, 70-83; https://doi.org/10.2138/am-2015-4933

Frezzotti, M. L., Tecce, F., Casagli, A. (2012a). Raman spectroscopy for fluid inclusion analysis. *Journal of Geochemical Exploration*, **112**, 1-20; https://doi.org/10.1016/j.gexplo.2011.09.009

Frezzotti, M. L., Touret, J. L. (2014). CO_2, carbonate-rich melts, and brines in the mantle. *Geoscience Frontiers*, **5(5)**, 697-710; https://doi.org/10.1016/j.gsf.2014.03.014

Frezzotti, M. L., Touret, J. L., Lustenhouwer, W. J., Neumann, E. R. (1994). Melt and fluid inclusions in dunite xenoliths from La Gomera, Canary Islands: tracking the mantle metasomatic fluids. *European Journal of Mineralogy-Ohne Beihefte*, **6(6)**, 805-818; 10.1127/ejm/6/6/0805

Fukura S., Mizukami T., Odake S., Kagi H. (2006). Factors determining the stability, resolution, and precision of a conventional Raman spectrometer. *Applied Spectroscopy* **60(8)**, 946-950; https://doi.org/10.1366/000370206778062165

Gaillard, F., Sator, N., Gardés, E., Guillot, B., Massuyeau, M., Sifré, D., . . . Richard, G. (2019). The Link between the Physical and Chemical Properties of Carbon-Bearing Melts and Their Application for Geophysical Imaging of Earth's Mantle. In B. Orcutt, I. Daniel, and R. Dasgupta (Eds.), *Deep Carbon: Past to Present* (pp. 163-187). Cambridge: Cambridge University Press; https://doi.org/10.1017/9781108677950

Garrabos, Y., Chandrasekharan, V., Echargui, M. A., Marsault-Herail, F. (1989a). Density effect on the Raman fermi resonance in the fluid phases of CO_2. *Chemical physics letters*, **160(3)**, 250-256; https://doi.org/10.1016/0009-2614(89)87591-8

Garrabos, Y., Echargui, M. A., Marsault-Herail, F. (1989b). Comparison between the density effects on the levels of the Raman spectra of the Fermi resonance doublet of the $^{12}C^{16}O_2$ and $^{13}C^{16}O_2$ molecules. *The Journal of chemical physics*, **91(10)**, 5869-5881; https://doi.org/10.1063/1.457455

Garrabos, Y., Tufeu, R., Le Neindre, B., Zalczer, G., Beysens, D. (1980). Rayleigh and Raman scattering near the critical point of carbon dioxide. *The Journal of Chemical Physics*, **72(8)**, 4637-4651; https://doi.org/10.1063/1.439706

Gaufrès, R., Huguet, P., Arab, Y. (1995). Method for the determination of spectral shifts in Raman spectroscopy. *Journal of Raman Spectrosc*opy, **26 (3)**, 243–253; https://doi.org/10.1002/jrs.1250260307

Gennaro, M. E., Grassa, F., Martelli, M., Renzulli, A., Rizzo, A. L. (2017). Carbon isotope composition of CO_2-rich inclusions in cumulate-forming mantle minerals from Stromboli volcano (Italy). *J. Volcanologica and Geothermal Research*, **346**, 95-103; https://doi.org/10.1016/j.jvolgeores.2017.04.001

Gordon, H. R., McCubbin Jr, T. K. (1966). The 2.8-micron bands of CO_2. *Journal of Molecular Spectroscopy*, **19(1-4)**, 137-154; https://doi.org/10.1016/0022-2852(66)90237-2

Gu, Y., Zhou, Y., Tang, H., Rothe, E. W., Reck, G. P. (2000). Pressure dependence of vibrational Raman scattering of narrow-band, 248-nm, laser light by H_2, N_2, O_2, CO_2, CH_4, C_2H_6, and C_3H_8 as high as 97 bar. *Applied Physics B*, **71(6)**, 865-871; https://doi.org/10.1007/s003400000412

Hagiwara, Y., Yoshida, K., Yoneda, A., Torimoto, J., Yamamoto, J. (2021). Experimental variable effects on laser heating of inclusions during Raman spectroscopic analysis. *Chemical Geology*, **559**, 119928; https://doi.org/10.1016/j.chemgeo.2020.119928

Hayes, J. M. An introduction to isotopic calculations. Woods Hole Oceanographic Institution, Woods Hole, MA, 2543; (2004).

Herzberg, G. (1945). Molecular spectra and molecular structure. Vol. 2: Infrared and Raman spectra of polyatomic molecules. Molecular spectra and molecular structure.

Howard-Lock, H. E., Stoicheff, B. P. (1971). Raman intensity measurements of the Fermi diad ν_1, $2\nu_2$ in $^{12}CO_2$ and $^{13}CO_2$. *Journal of Molecular Spectroscopy*, **37(2)**, 321-326; https://doi.org/10.1016/0022-2852(71)90302-X

Hurai, V., Huraiová, M., Slobodník, M., Thomas, R. (2015). Geofluids: developments in microthermometry, spectroscopy, thermodynamics, and stable isotopes. Elsevier.

Hutsebaut, D., Vandenabeele, P., Moens L. (2005). Evaluation of an accurate calibration and spectral standardization procedure for Raman spectroscopy. *Analyst*, **130(8)**, 1204-1214; https://doi.org/10.1039/b503624k

Hidas, K., Guzmics, T., Szabó, C., Kovács, I., Bodnar, R. J., Zajacz, Z., ... and Perucchi, A. (2010). Coexisting silicate melt inclusions and H2O-bearing, CO2-rich fluid inclusions in mantle peridotite xenoliths from the Carpathian–Pannonian region (central Hungary). *Chemical Geology*, **274(1-2)**, 1-18; https://doi.org/10.1016/j.chemgeo.2010.03.004

Irmer, G., Graupner, T. (2002). Isotopes of C and O in CO_2: a Raman study using gas standards and natural fluid inclusions. Acta Univ. Carolinae, Geol, 46, 35-36.

Kawakami, Y., Yamamoto, J., Kagi, H. (2003). Micro-Raman densimeter for CO_2 inclusions in mantle-derived minerals. *Applied spectroscopy*, **57(11)**, 1333-1339; https://www.osapublishing.org/as/abstract.cfm?URI=as-57-11-1333

Lamadrid, H. M., Moore, L. R., Moncada, D., Rimstidt, J. D., Burruss, R. C., Bodnar, R. J. (2017). Reassessment of the Raman CO_2 densimeter. *Chemical Geology*, **450**, 210-222; https://doi.org/10.1016/j.chemgeo.2016.12.034

Le, V., Caumon, M., Tarantola, A., Randi, A., Robert, P., Mullis, J. (2019). Quantitative Measurements of Composition, Pressure, and Density of Microvolumes of CO_2–N_2 Gas Mixtures

by Raman Spectroscopy. *Analytical chemistry*, **91**, 14359-14367; https://doi.org/10.1021/acs.analchem.9b02803

Lee, W. J., Wyllie, P. J. (1998). Petrogenesis of carbonatite magmas from mantle to crust, constrained by the system CaO–(MgO+FeO*)–(Na_2O+K_2O)–(SiO_2+Al_2O_3+TiO_2)-CO_2. *Journal of Petrology*, **39(3)**, 495-517; https://doi.org/10.1093/petroj/39.3.495

Li, J. J., Li, R. X., Dong, H., Wang, Z. H., Zhao, B. S., Wang, N., Cheng, J. H. (2017). Carbon isotopic compositions in carbon dioxide measured by micro-laser Raman spectroscopy. *Journal of Applied Spectroscopy*, **84(2)**, 237-241; https://doi.org/10.1007/s10812-017-0457-8

Li, J., Li, R., Zhao, B., Guo, H., Zhang, S., Cheng, J., Wu, X. (2018). Quantitative measurement of carbon isotopic composition in CO_2 gas reservoir by Micro-Laser Raman spectroscopy. *Spectrochimica Acta Part A: Molecular and Biomolecular Spectroscopy*, **195**, 191-198; https://doi.org/10.1016/j.saa.2018.01.082

Li, J., Li, R., Zhao, B., Wang, N., Cheng, J. (2016). Quantitative analysis and measurement of carbon isotopic compositions in individual fluid inclusions by micro-laser Raman spectrometry. *Analytical Methods*, **8**, 6730-6738. https://doi.org/10.1039/C6AY01897A

Lin, F., Sum, A. K., Bodnar, R. J. (2007). Correlation of methane Raman ν_1 band position with fluid density and interactions at the molecular level. *Journal of Raman Spectroscopy*, **38(11)**, 1510-1515; https://doi.org/10.1002/jrs.1804

Marshall, D., Pfeifer, H. R., Sharp, Z. (1994). A re-evaluation of Raman as a tool for the determination of ^{12}C and ^{13}C in geological fluid inclusions. *Analysis*, **22**, M38-M41.

Mattey, D. P., Carr, R. H., Wright, I. P., Pillinger, C. T. (1984). Carbon isotopes in submarine basalts. *Earth Planetary Sciences Letters*, **70**, 196-206; https://doi.org/10.1016/0012-821X(84)90005-0

McCreery, R. L. (2000). Raman spectroscopy for chemical analysis. John Wiley and Sons, Vol. 225.

McMillan, P. F. (1985). Vibrational spectroscopy in the mineral sciences. In: Kiffer SW and Navrotsky A (eds.) Microscopic to Macroscopic: Atomic Environments to Mineral Thermodynamics, vol. 14, pp. 9–63. Washington, DC: Mineralogical Society of America.

Mestari, A., Gaufrès, R., Huguet, P. (1997). Behaviour of the calibration of a Raman spectrometer with temperature changes. *Journal of Raman Spectroscopy*, **28 (10)**, 785–789; https://doi.org/10.1002/(SICI)1097-4555(199710)28:10<785::AID-JRS148>3.0.CO;2-D

Nasdala, L., Smith, D. C., Kaindl, R., Ziemann, M. A. (2004). Raman spectroscopy: analytical perspectives in mineralogical research. In Spectroscopic methods in mineralogy, **6**, 281-343.

Oglialoro, E., Frezzotti, M. L., Ferrando, S., Tiraboschi, C., Principe, C., Groppelli, G., Villa, I. M. (2017). Lithospheric magma dynamics beneath the El Hierro Volcano, Canary Islands: insights from fluid inclusions. *Bulletin of Volcanology*, **79(10)**, 1-17; https://doi.org/10.1007/s00445-017-1152-6

Pasteris, J. D. (1987). Fluid Inclusions in Mantle Xenoliths. P.H. Nixon (Ed.), Mantle Xenoliths, John Wiley and sons, Chichester (1987), pp. 691-708.

Pasteris, J. D., Kuehn, C. A., Bodnar, R. J. (1986). Applications of the laser Raman microprobe RAMANOR U-1000 to hydrothermal ore deposits; Carlin as an example. *Economic Geology*, **81(4)**, 915-930; https://doi.org/10.2113/gsecongeo.81.4.915

Pasteris, J. D., Wopenka, B., Seitz, J. C. (1988). Practical aspects of quantitative laser Raman microprobe spectroscopy for the study of fluid inclusions. *Geochimica et Cosmochimica Acta*, **52(5)**, 979-988; https://doi.org/10.1016/0016-7037(88)90253-0

Pelletier, M. J., (2003). Quantitative Analysis Using Raman Spectrometry. *Applied Spectroscopy*, **57**, 20A-42A; https://www.osapublishing.org/as/abstract.cfm?URI=as-57-1-20A

Placzek, G. (1934). *Rayleigh-streuung und Raman-effekt* (Vol. 2). Akademische Verlagsgesellschaft.

Raman, C. (1998). A new radiation [Reproduced from Indian J. Phys., 1928, 2, 387–398]. *Current Science*, **74(4)**, 382-386. https://www.jstor.org/stable/24101519

Remigi, S., Mancini, T., Ferrando, S., Frezzotti, M. L. (2021). Inter-Laboratory Application of Raman CO_2 Densimeter Equations: Experimental Procedure and Statistical Analysis Using Bootstrapped Confidence Intervals. *Applied Spectroscopy*, 0003702820987601; https://doi.org/10.1177/0003702820987601

Rizzo, A. L., Pelorosso, B., Coltorti, M., Ntaflos, T., Bonadiman, C., Matusiak-Małek, M., ..., Bergonzoni, G. (2018). Geochemistry of noble gases and CO_2 in fluid inclusions from lithospheric mantle beneath Wilcza Góra (Lower Silesia, southwest Poland). *Frontiers in Earth Sciences*, **6**, 215; https://doi.org/10.3389/feart.2018.00215

Roedder, E. (1962). Studies of fluid inclusions; Part 1, Low temperature application of a dual-purpose freezing and heating stage. *Economic Geology*, **57(7)**, 1045-1061; https://doi.org/10.2113/gsecongeo.57.7.1045

Roedder, E. (1963). Studies of fluid inclusions; [Part] 2, Freezing data and their interpretation. *Economic Geology*, **58(2)**, 167-211; https://doi.org/10.2113/gsecongeo.58.2.167

Roedder, E. (1965). Liquid CO_2 inclusions in olivine-bearing nodules and phenocrysts from basalts. *American Mineralogist: Journal of Earth and Planetary Materials*, **50(10)**, 1746-1782.

Roedder, E. (1984). Volume 12: fluid inclusions. *Mineralogical Society of America*.

Roedder, E., Bodnar, R. J. (1997). Fluid inclusion studies of hydrothermal ore deposits. H.L. Barnes (Ed.), Geochemistry of Hydrothermal Ore Deposits (third ed.), Wiley and Sons Inc., New York, pp. 657-698.

Rosasco, G. J., Roedder, E., Simmons, J. H. (1975). Laser-excited Raman spectroscopy for nondestructive partial analysis of individual phases in fluid inclusions in minerals. *Science*, **190(4214)**, 557-560; https://www.jstor.org/stable/1740436

Rosso, K. M., Bodnar, R. J. (1995). Microthermometric and Raman spectroscopic detection limits of CO_2 in fluid inclusions and the Raman spectroscopic characterization of CO_2. *Geochimica et Cosmochimica Acta*, **59(19)**, 3961-3975; https://doi.org/10.1016/0016-7037(95)94441-H

Rudolph, W. W., Fischer, D., Irmer, G. (2006). Vibrational spectroscopic studies and density functional theory calculations of speciation in the CO_2-water system. *Applied spectroscopy*, **60(2)**, 130-144; https://doi.org/10.1366/000370206776023421

Schrauder, M., and Navon, O. (1994). Hydrous and carbonatitic mantle fluids in fibrous diamonds from Jwaneng, Botswana. *Geochimica et Cosmochimica Acta*, **58(2)**, 761-771; https://doi.org/10.1016/0016-7037(94)90504-5

Schrauder, M., Koeberl, C., and Navon, O. (1996). Trace element analyses of fluid-bearing diamonds from Jwaneng, Botswana. *Geochimica et Cosmochimica Acta*, **60(23)**, 4711-4724; https://doi.org/10.1016/S0016-7037(96)00274-8

Schrötter, H. W., Klöckner, H. W. (1979). Raman scattering cross sections in gases and liquids. In Raman spectroscopy of gases and liquids (pp. 123-166). Springer, Berlin, Heidelberg.

Schwarts, H. P. (1969). The stable isotopes of carbon. In: Handbook of geochemistry, Vol II/I, p. 6BI-6BI6, Springer.

Seitz, J. C., Blencoe, J. G., Joyce, D. B., Bodnar, R. J. (1994). Volumetric properties of CO_2-CH_4-N_2 fluids at 200° C and 1000 bars: A comparison of equations of state and experimental data. *Geochimica et cosmochimica acta*, **58(3)**, 1065-1071; https://doi.org/10.1016/0016-7037(94)90572-X

Seitz, J. C., Pasteris, J. D. (1990). Theoretical and practical aspects of differential partitioning of gases by clathrate hydrates in fluid inclusions. *Geochimica et Cosmochimica Acta*, **54(3)**, 631-639; https://doi.org/10.1016/0016-7037(90)90359-S

Seitz, J. C., Pasteris, J. D., Chou, I. M. (1993). Raman spectroscopic characterization of gas mixtures; I, Quantitative composition and pressure determination of CH_4, N_2 and their mixtures. *American Journal of Science*, **293(4)**, 297-321; https://doi.org/10.2475/ajs.293.4.297

Seitz, J. C., Pasteris, J. D., Chou, I. M. (1996). Raman spectroscopic characterization of gas mixtures. II. Quantitative composition and pressure determination of the CO_2-CH_4 system. *American Journal of Science*, **296(6)**, 577-600; https://doi.org/10.2475/ajs.296.6.577

Seitz, J. C., Pasteris, J. D., Wopenka, B. (1987). Characterization of CO_2-CH_4-H_2O fluid inclusions by microthermometry and laser Raman microprobe spectroscopy: Inferences for clathrate and fluid equilibria. *Geochimica et Cosmochimica Acta*, **51(6)**, 1651-1664; https://doi.org/10.1016/0016-7037(87)90345-0

Shang, L., Chou, I. M., Burruss, R. C., Hu, R., Bi, X. (2014). Raman spectroscopic characterization of CH_4 density over a wide range of temperature and pressure. *Journal of Raman Spectroscopy*, **45(8)**, 696-702; https://doi.org/10.1002/jrs.4529

Sharp, Z. "Principles of Stable Isotope Geochemistry, 2nd Edition." (2017). https://doi.org/10.25844/h9q1-0p82

Song, Y., Chou, I. M., Hu, W., Robert, B., Lu, W. (2009). CO_2 density-Raman shift relation derived from synthetic inclusions in fused silica capillaries and its application. *Acta Geologica Sinica-English Edition*, **83(5)**, 932-938; https://doi.org/10.1111/j.1755-6724.2009.00090.x

Span, R., Wagner, W. (1996). A new equation of state for carbon dioxide covering the fluid region from the triple-point temperature to 1100 K at pressures up to 800 MPa. *Journal of physical and chemical reference data*, **25(6)**, 1509-1596; https://doi.org/10.1063/1.555991

Stellman, C. M., Aust, J. F., Myrick, M. L. (1995). In Situ Spectroscopic Study of Microwave Polymerization. *Applied Spectroscopy*, **49(3)**, 392–394; https://doi.org/10.1366/0003702953963535

Sterner, S. M., and Bodnar, R. J. (1991). Synthetic fluid inclusions; X, Experimental determination of PVTX properties in the CO_2-H_2O system to 6 kbar and 700°C degrees. *American Journal of Science*, **291(1)**, 1-54; https://doi.org/10.2475/ajs.291.1.1

Sterner, S.M., Pitzer, K.S. (1994). An equation of state for carbon dioxide valid from zero toextreme pressures. *Contribution to Mineralogy and Petrology*, **117(4)**, 362–374; https://doi.org/10.1007/BF00307271

Stoicheff, B. (1958). High resolution Raman spectroscopy of gases: XI. Spectra of CS_2 and CO_2. *Canadian Journal of Physics*, **36(2)**, 218-230; https://doi.org/10.1139/p58-026

Sublett, Jr D. M., Sendula, E., Lamadrid, H., Steele-MacInnis, M., Spiekermann, G., Burruss, R. C., Bodnar R. J. (2019). Shift in the Raman symmetric stretching band of N_2, CO_2, and CH_4 as a function of temperature, pressure, and density. *Journal of Raman Spectroscopy*, **51(3)**, 555-568; https://doi.org/10.1002/jrs.5805

Szabo, C., Bodnar, R. J., and Sobolev, A. V. (1996). Metasomatism associated with subduction-related, volatile-rich silicate melt in the upper mantle beneath the Nograd-Gomor volcanic field, northern Hungary/southern Slovakia; evidence from silicate melt inclusions. *European Journal of Mineralogy*, **8(5)**, 881-899; 0935-1221/96/0008-0881

Török, K., Dégi, J., Szép, A., and Marosi, G. (2005). Reduced carbonic fluids in mafic granulite xenoliths from the Bakony–Balaton Highland Volcanic Field, W-Hungary. *Chemical geology*, **223(1-3)**, 93-108; https://doi.org/10.1016/j.chemgeo.2005.05.010

Touret, J. (1977). The significance of fluid inclusions in metamorphic rocks. In *Thermodynamics in geology* (pp. 203-227). Springer, Dordrecht.

Touret, J. (1986). Fluid inclusions in rocks from the lower continental crust. *Geological Society, London, Special Publications*, **24(1)**, 161-172; https://doi.org/10.1144/GSL.SP.1986.024.01.15

Touret, J. L. (1981). Fluid inclusions in high grade metamorphic rocks. In: Short Course in Fluid Inclusions: Applications to Petrology. In: Hollister, L.S., Crawford, M.L. (Eds.), Mineralogical Association of Canada Short Course Handbook 6, pp. 182–208.Touret, 1986;

Touret, J. L. (1992). CO_2 transfer between the upper mantle and the atmosphere: temporary storage in the lower continental crust. *Terra Nova*, **4(1)**, 87-98; https://doi.org/10.1111/j.1365-3121.1992.tb00453.x

Touret, J. L., and Huizenga, J. M. (2012a). Fluid-assisted granulite metamorphism: a continental journey. *Gondwana Research*, **21(1)**, 224-235; https://doi.org/10.1016/j.gr.2011.07.022

Touret, J. L., Huizenga, J. M. (2012b). Charnockite microstructures: from magmatic to metamorphic. *Geoscience Frontiers*, **3(6)**, 745-753; https://doi.org/10.1016/j.gsf.2012.05.004

Van den Kerkhof, A. M. (1988). Phase transitions and molar volumes of CO_2-CH_4-N_2 inclusions. *Bulletin de minéralogie*, **111(3)**, 257-266; https://doi.org/10.3406/bulmi.1988.8046

Van den Kerkhof, A. M., Olsen, S. N. (1990). A natural example of superdense CO_2 inclusions: microthermometry and Raman analysis. *Geochimica et Cosmochimica Acta*, **54(3)**, 895-901; https://doi.org/10.1016/0016-7037(90)90383-V

Van den Kerkhof, A., Thiery, R. (2001). Carbonic inclusions. *Lithos*, **55(1-4)**, 49-68; https://doi.org/10.1016/S0024-4937(00)00038-4

Wallace, M. E., Green, D. H. (1988). An experimental determination of primary carbonatite magma composition. *Nature*, **335(6188)**, 343-346; https://doi.org/10.1038/335343a0

Wang, X., Chou, I. M., Hu, W., Burruss, R. C., Sun, Q., Song, Y. (2011). Raman spectroscopic measurements of CO_2 density: Experimental calibration with high-pressure optical cell (HPOC) and fused silica capillary capsule (FSCC) with application to fluid inclusion observations.

Geochimica et Cosmochimica Acta, **75(14)**, 4080-4093; https://doi.org/10.1016/j.gca.2011.04.028

Weber, W. H., Zanini-Fisher, M., Pelletier, M. J. (1997). Using Raman Microscopy to Detect Leaks in Micromechanical Silicon Structures. *Applied Spectroscopy*, **51(1),** 123–129; https://doi.org/10.1366/0003702971938876

Wojdyr, M. (2010). Fityk: a general-purpose peak fitting program. *Journal of Applied Crystallography*, **43**, 1126-1128; https://doi.org/10.1107/S0021889810030499

Wopenka, B., Pasteris, J. D. (1986). Limitations to quantitative analysis of fluid inclusions in geological samples by laser Raman microprobe spectroscopy. *Applied Spectroscopy*, **40(2)**, 144-151; https://www.osapublishing.org/as/abstract.cfm?URI=as-40-2-144

Wopenka, B., Pasteris, J. D. (1987). Raman intensities and detection limits of geochemically relevant gas mixtures for a laser Raman microprobe. *Analytical Chemistry*, **59(17)**, 2165-2170; https://doi.org/10.1021/ac00144a034

Wright, R. B., Wang, C. H. (1973). Density effect on the Fermi resonance in gaseous CO_2 by Raman scattering. *The Journal of Chemical Physics*, **58(7)**, 2893-2895; https://doi.org/10.1063/1.1679594

Yamamoto, J., Kagi, H. (2006). Extended micro-Raman densimeter for CO_2 applicable to mantle-originated fluid inclusions. *Chemistry Letters*, **35(6)**, 610-611; https://doi.org/10.1246/cl.2006.610

Yamamoto, J., Kagi, H. (2008). Application of densimetry using micro-Raman spectroscopy for CO_2 fluid inclusions: a probe for elastic strengths of mantle minerals. *European Journal of Mineralogy*, **20(4)**, 529-535; https://doi.org/10.1127/0935-1221/2008/0020-1825

Yardley, B. W., Bodnar, R. J. (2014). Fluids in the continental crust. *Geochemical Perspectives*, **3(1)**, 1-2.

Yokokura, L., Hagiwara, Y., Yamamoto, J. (2020). Pressure dependence of micro-Raman mass spectrometry for carbon isotopic composition of carbon dioxide fluid. *Journal of Raman Spectroscopy*, **51(6)**, 997-1002; https://doi.org/10.1002/jrs.5864

Yuan, X., Mayanovic, R. A. (2017). An empirical study on Raman peak fitting and its application to Raman quantitative research. *Applied Spectroscopy*, **71(10)**, 2325-2338; https://doi.org/10.1177/0003702817721527

Zanon, V. (2015). Conditions for mafic magma storage beneath fissure zones at oceanic islands. The case of São Miguel island (Azores archipelago). *Geological Society, London, Special Publications*, **422(1)**, 85-104; https://doi.org/10.1144/SP422.4

Zanon, V., Frezzotti, M. L. (2013). Magma storage and ascent conditions beneath Pico and Faial islands (Azores archipelago): A study on fluid inclusions. *Geochemistry, Geophysics, Geosystems*, **14(9)**, 3494-3514; doi: 10.1002/ggge.20221

Zare, R. N., Kuramoto, D. S., Haase, C., Tan, S. M., Crosson, E. R., Saad, N. M. (2009). High-precision optical measurements of $^{13}C/^{12}C$ isotope ratios in organic compounds at natural abundance. *Proceedings of the National Academy of Science Usa*, **106(27)**, 10928-10932; https://doi.org/10.1073/pnas.0904230106

6. IN-SITU DISCRIMINATION OF THE CARBON ISOTOPIC SIGNATURE OF NATURAL CO_2 FLUID INCLUSIONS BY RAMAN SPECTROSCOPY (*MANISCRIPT 1*)

Samantha Remigi[1,*], Maria Luce Frezzotti[1,*], Robert J. Bodnar[2], Andres Libardo Sandoval Velasquez[3], Andrea Luca Rizzo[4] and Alessandro Aiuppa[3]

[1] *Dipartimento di Scienze dell'Ambiente e della Terra, Università Milano - Bicocca, Piazza della Scienza 4, 20126, Milano, Italia.*

[2] *Department of Geosciences, Virginia Tech, 926 West Campus Drive, Blacksburg (VA), 24061, USA.*

[3] *Dipartimento di Scienze della Terra e del Mare, Università di Palermo, Via Archirafi 22, 90153, Palermo, Italia.*

[4]*Instituto Nazionale Geofisica e Vulcanologia, Via Ugo La Malfa I-153, 90146, Palermo, Italia.*

**corresponding authors: s.remigi@campus.unimib.it; maria.frezzotti@unimib.it*

Abstract

In the Raman spectrum of CO_2, band areas for $^{13}CO_2$ and $^{12}CO_2$ upper bands (ν_1) are proportional to their molar fraction, allowing determinating $\delta^{13}C_{CO2}$ values. To calculate reliable $\delta^{13}C_{CO2}$ values, an area ratio precision at the fourth decimal place is required, but achieving this high level of precision is complicated due to random noise that affects $^{13,12}CO_2$ ν_1 area measurements. The present work investigates the optimum experimental parameters and procedures, allowing the reduction of uncertainties related to the nature of Raman scattering of light and enabling the calculation of $^{13}C_{CO2}/^{12}C_{CO2}$ isotopic ratios in single fluid inclusions (FI). Forty-two mantle-derived pure CO_2 FI from the Lake Tana region (Ethiopia) and El Hierro (Canary Islands) have been selected for analyses. Sets of area ratios measurements characterised by area ratios differing more than one order of magnitude have been removed from the dataset since they are caused by random perturbations of spectra. 95% of the sets of analyses were characterised by area ratios reproducibility $<\approx 4‰$, allowing to calculate FI $\delta^{13}C_{CO2}$ values with a precision of $<\pm\approx 2‰$. A few analyses had lower precision, reflecting the inability to avoid random Raman spectra perturbations during analyses altogether. Bulk measurements of $\delta^{13}C_{CO2}$ compositions of FI in Ol, Opx and Cpx from El

Hierro proved that 95% of $\delta^{13}C_{CO2}$ values obtained with Raman analyses were in agreement with bulk analyses, allowing us modelling $\delta^{13}C_{CO2}$ variations at a single mineral scale. Results show that, although isotopic compositions determined by Raman spectroscopy are slightly less precise than those obtained by conventional ratio mass spectrometry, Raman micro-spectroscopy is a potential complementary method for in situ and non-destructive determination of $\delta^{13}C_{CO2}$ in FI, improving our ability to trace CO_2 fluid evolution at mantle depths.

Keywords

Raman spectroscopy, carbon dioxide, in situ $^{13}C_{CO2}/^{12}C_{CO2}$ isotope ratio, carbon dioxide $\delta^{13}C_{CO2}$

Introduction

Carbon dioxide (CO_2) is an essential component of the Earth's carbonbudget, and likely plays a crucial role in the deep carbon cycle. Determining the origin of CO_2 in geological fluids is crucial for linking carbon mobility in the crust and upper mantle to surface processes. [1-4] In this regard, knowledge of the carbon stable isotope composition is essential for discriminating the relative contributions from the various reservoirs in the Earth system, each having distinct isotopic signatures. [5-12]

CO_2 fluids present at crustal and mantle pressure and temperature conditions are locally preserved in rocks as fluid inclusions – micrometre-sized fluid-filled cavities in minerals (Fig. 1a). [13-15] The $^{13}C_{CO2}/^{12}C_{CO2}$ isotopic ratio is expressed in delta (δ) notation [16] relative to the Vienna Pee Dee Belemnite (PDB) standard per mil ($\delta^{13}C_{CO2}$ ‰). Most commonly, $^{13}C_{CO2}/^{12}C_{CO2}$ ratios in FI are measured using conventional ratio mass spectrometry, which allows high precision measurements (≈ 0.1 -0.15‰) [17-20] but is technically challenging due to the small fluid quantity extracted from the crushing or heating of samples. [21, 22]

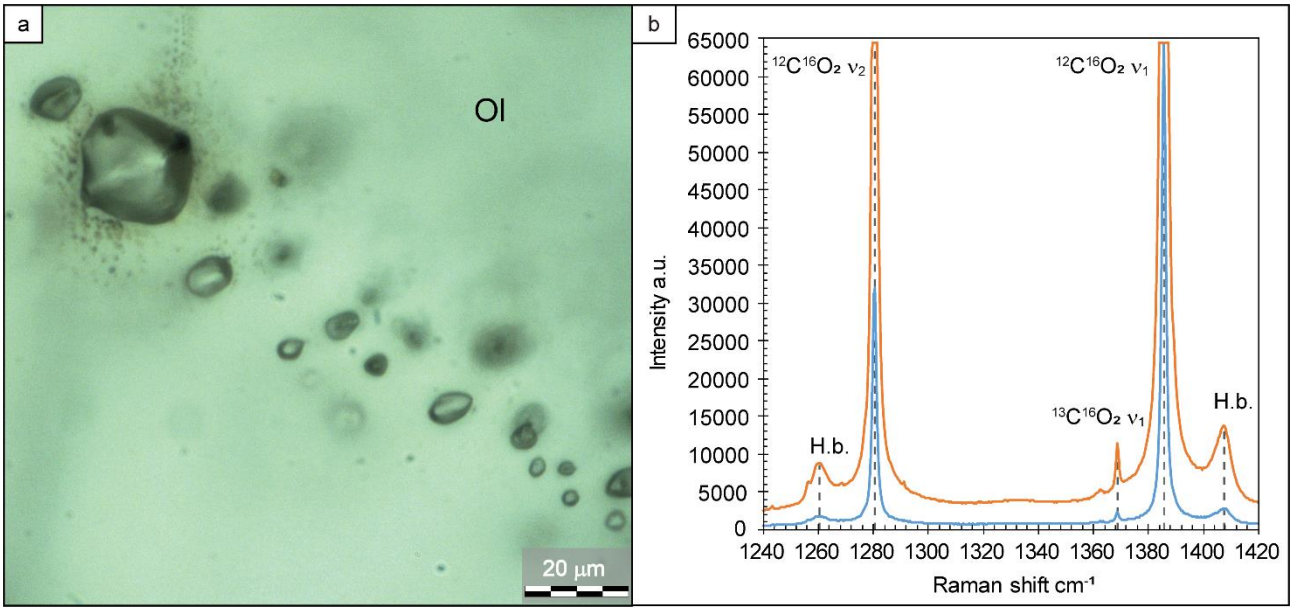

Figure 1 Photomicrograph of natural CO_2 FI and Raman spectrum of a natural CO_2 FI from a mantle xenoliths. a) Photomicrograph of a trail of CO_2 FI trapped in olivine in a mantle xenolith (sample XML6) from El Hierro (Canary Islands). b) Two Raman spectra of a CO_2 FI obtained using different acquisition times (light blue = 85 seconds acquisition time; orange = 425 seconds acquisition time). The spectra are characterised by the upper and lower bands of the $^{12}C^{16}O_2$ isotopologue ($^{12}C^{16}O_2$ ν_1 and $^{12}C^{16}O_2$ ν_2, respectively) and the upper band of the $^{13}C^{16}O_2$ one ($^{13}C^{16}O_2$ ν_1); hot bands (H.b.) are also visible. Due to the longer acquisition times, the spectrum for the $^{12}C^{16}O_2$ upper and lower bands shown in orange are saturated. Ol = olivine; a.u. = arbitrary units; cm^{-1} = Raman shift.

Raman micro-spectroscopy provides an alternative to determine the carbon isotopic composition of CO_2 that offers many benefits compared to conventional mass-spectrometry, such as the fact that it is a non-destructive technique and with high spatial resolution. [23-26] Raman vibrational modes for the various isotopologues (molecules differing from one another only in isotopic composition) are different, allowing the isotopic composition to be inferred based on the Raman spectrum. In the Raman spectrum of CO_2 (Fig. 1b), bands for the $^{12}C^{16}O_2$ and $^{13}C^{16}O_2$ molecules are represented by the ν_1 Fermi diad, separated by a wavenumber shift of about 20 cm^{-1}. [27, 28]

For gaseous species, such as CO_2, the area of the Raman spectral band is directly proportional to the number of molecules in the analytical volume, which, in turn, is proportional to the number of bonds being interrogated. [23, 29-32] As a result, it should be possible to measure the concentrations of the different CO_2 isotopologues based on the statistical treatment of relative band areas.

Several previous studies have reported Raman analyses of $^{13}CO_2/^{12}CO_2$ ratios in natural fluid inclusions (FI) and optical cells. [30, 34-38] Unfortunately, none of these studies was able to determine $\delta^{13}C_{CO2}$ with a precision of better than about ±10-20‰, rendering it inadequate to distinguish between the different carbon reservoirs in the Earth system. Consequently, additional analytical development is necessary to explore the possibility of improving the prevision of isotopic composition based on Raman spectroscopy.

Here, we determine the optimal experimental parameters for Raman micro-spectroscopic analysis of CO_2 isotopologues in FI that reduce the intrinsic errors related to the discrete nature of the light phonon (e.g., intensity fluctuations, noise). To develop and test the methodology, we selected FI in lithospheric mantle rocks from two different locations: El Hierro Island (Canary Islands) and the Lake Tana region (Ethiopia) [39, 40]. Results presented here describe the *in situ* determination of the carbon isotopic signature of single FI with a precision of $\leq\approx$2.00‰, allowing carbon isotopic variations at the single mineral scale to be characterised.

Analytical methods

Analytical setup

Raman spectroscopy allows the simultaneous measurement of both the $^{13}CO_2$ and $^{12}CO_2$ scattering bands in a single FI. The amplitude of these bands is proportional to the excited bonding energy of the single molecules, which, in turn, depends on the relative number of $^{13}CO_2$ and $^{12}CO_2$ molecules within the analysed system (cf. Supplementary note S.1). [23, 29-32] Thus, the band area ratios of $^{13}CO_2$ and $^{12}CO_2$ can be used to calculate the $\delta^{13}C_{CO2}$ value (cf. Supplementary note S.1). In natural systems,

the relative concentration of $^{13}C_{CO2}$ in CO_2 fluids is ≈1.1%, on average. As such, a precision in the area ratio at the fourth decimal place is required to allow discrimination among different carbon reservoirs on Earth with a precision of part per thousands (‰). [12, 41, 42] Thus, in the CO_2 Raman spectrum, the low intensity of the $^{13}CO_2$ band (Fig. 1b) relative to the $^{12}CO_2$ band is the primary source of uncertainty that affects the quality of the fit of the band area.

In order to obtain a sufficient number of "counts" to minimize the uncertainty related to the area of the $^{13}CO_2$ band, long accumulation times have been applied in most studies to increase the area (intensity) of the $^{13}CO_2$ band, followed by integrating the $^{13}CO_2$ and the $^{12}CO_2$ band areas measured separately in consecutive analyses. [34-38] However, long accumulation times can introduce other biases through various sample-generated and instrument-generated sources of noises, typically occurring during prolonged exposure of the sample to laser light (e.g., dark noise, mainly depending on the temperature variation at the sample or in the instrument mechanic and optic components through laser heating). [43-45] Noise enhances the background scattering, randomly modifying the shapes of the bands and, consequently, band areas in consecutive acquisitions.

In the present study, we improved the sensitivity of the $^{13}CO_2$ signal by analysing CO_2 inclusions at high laser power, and using high-resolution gratings and high confocality, while keeping short acquisition times (cf. "Raman micro-spectroscopy" section). This analytical setup mitigates the spectral background noise, allowing the $^{13}CO_2$ and the $^{12}CO_2$ band measurements in most cases in the same spectrum. The temperature in the laboratory was kept within a 1° interval.

Even with the approach described above, noise effects cannot be entirely eliminated during consecutive analyses and may erratically affect spectral output, leading to highly variable measured $^{12}C_{CO2}/^{13}C_{CO2}$ area ratios for the same FI. For this reason, we performed 84 sets of measurements in 42 FI. Each inclusion was analysed by collecting two consecutive sets of 3 spectra each. In the first set, accumulation times were set to allow simultaneous measurement of $^{13}CO_2$ and $^{12}CO_2$ band areas in a single spectrum, while in the second one, longer accumulations were used for the $^{13}CO_2$ band compared to the $^{12}CO_2$ band (cf. "Raman micro-spectroscopy" section). Those sets of analyses in which at least one area ratio differed by one order of magnitude from the other ratios were excluded from further analysis. For the remaining set of analyses, the reproducibility has been evaluated both in terms of *Variance‰* and *Reproducibility‰* (cf. "Raman micro-spectroscopy" section).

Raman micro-spectroscopy

Raman analyses have been performed by mean of the Horiba Jobin Yvon LabRAM HR Evolution Raman System, at the Dipartimento di Scienze dell'Ambiente e della Terra, Università di Milano –

Bicocca. The system has a focal length of 800 mm and includes an air-cooled 1024*256 pixel CCD detector and nine neutral density filters. An Olympus BXFM microscope allows observations in transmitted and reflected light. CO_2 spectra were recorded using a frequency-doubled green Nd 532.06 nm (green) laser source (300 mW), powered at 150 mW by mean of the 50% neutral density filter, with a 100× magnification. The analytical setup included a 100 µm confocal hole and an 1800 gr/mm grating, allowing coverage of a spectral range between 1069.98 and 1522.70 cm^{-1}, corresponding to a spectral resolution of about 0.44 cm^{-1}/px. Acquired CO_2 spectra were treated by baseline removal and fitting with a Split-PseudoVoight curve (cf. Supplementary note S.2) [46] by the freeware software Fytik 1.3.1. [47]

The distance between the $^{12}CO_2$ upper and lower bands (Δ, in cm^{-1}) has been additionally measured to calculate the density of CO_2 in fluid inclusions based on the Raman densimeter method. According to Remigi et al. (2021), [48] due to the achieved spectral per pixel resolution (1800 gr/mm grating), the density of CO_2 fluid inclusions was calculated using the densimeter equation proposed by Fall et al. (2011). [49]

Fluid inclusions have been analysed in two consecutive sets of 3 spectra each. In the first set, accumulation times were set to allow simultaneous measurement of $^{13}CO_2$ and $^{12}CO_2$ band areas in a single spectrum (SS), and varied from 35 to 360 seconds based on the size and the depth of FI. In the second set of acquisitions, longer accumulations times, ranging from 175 to 1500 seconds, were used and $^{13}CO_2$ and $^{12}CO_2$ band areas measured in distinct (separate) spectra (DS).

$^{13}CO_2/^{12}CO_2$ area ratio reproducibility was investigated as *Variance‰* and *Reproducibility‰.* The *Variance‰* was used as an area ratio internal standard for each FI and was calculated according to equation [Eq.1]:

$$Variance‰ = \left\{\left[\left(\frac{\left(\frac{A_{13CO2v1}}{A_{12CO2v1}}\right)_{FI\ Max}}{\left(\frac{A_{13CO2v1}}{A_{12CO2v1}}\right)_{Ave}}\right) - 1\right] - \left[\left(\frac{\left(\frac{A_{13CO2v1}}{A_{12CO2v1}}\right)_{FI\ Min}}{\left(\frac{A_{13CO2v1}}{A_{12CO2v1}}\right)_{Ave}}\right) - 1\right]\right\} * 1000 \qquad \text{[Eq.1]}$$

where $\left(\frac{A_{13CO2v1}}{A_{12CO2v1}}\right)_{FI\ Max}$ and $\left(\frac{A_{13CO2v1}}{A_{12CO2v1}}\right)_{FI\ Min}$ are the maximum and the minimum area ratio values calculated for a single FI, and $\left(\frac{A_{13CO2v1}}{A_{12CO2v1}}\right)_{Ave}$ is the mean area ratio determined for the same FI. The higher the calculated *Variance‰* the lower is the precision of area ratios. The *Reproducibility‰* was calculated according to the equation proposed by Marshall et al. (1994) [Eq.2]:

$$Reproducibility‰ = \left[\frac{\left(\frac{A_{13CO2v1}}{A_{12CO2v1}}\right)_{1\sigma}}{\left(\frac{A_{13CO2v1}}{A_{12CO2v1}}\right)_{Ave}}\right] * 1000 \qquad \text{[eq.2]}$$

where $\left(\frac{A_{13CO2v1}}{A_{12CO2v1}}\right)_{1\sigma}$ is the standard deviation of the area ratio for a single FI and $\left(\frac{A_{13CO2v1}}{A_{12CO2v1}}\right)_{Ave}$ is the mean value for the same FI.

Mass spectroscopy

The carbon isotopic composition of CO_2 trapped in FI of minerals was analysed at the noble gas and stable isotopes laboratories of INGV, Sezione di Palermo (Italy) following the preparation methods and analytical procedures described by Correale et al. (2015), Gennaro et al. (2017) and Rizzo et al. (2018).[18-20] For this purpose, a suite of four ultramafic xenoliths from El Hierro (Canary Islands) was crushed and sieved, followed by hand-picking crystals of Ol, Opx and Cpx with diameters >0.5 mm. After cleaning, samples were weighed and loaded into an ultra-high-vacuum crusher for noble gas analyses, where the first estimate of the concentration of CO_2 in FI was performed. Based on the obtained results, seven aliquots of crystals with the highest concentrations were selected for $^{13}C/^{12}C$ analysis of CO_2 (2 aliquots of Ol, 4 of Opx and 1 of Cpx). These aliquots were ultrasonically cleaned in HCl (to avoid carbon contribution from the crystal surface), deionised water and high-purity acetone. Crystals were then weighed and loaded in a crusher system consisting of a stainless steel sample holder, a hydraulic press (which exerts a single-step pressure of approximately 200 bar), a glass sampler to freeze CO_2, and a vacuum pump to maintain a low pressure (10^{-3} - 10^{-4} mbar) inside the system. After crushing and trapping CO_2 in a portable glass sampler, the latter was connected to a glass line, equipped with a 626B Baratron® Absolute Capacitance Manometer MKS (measuring range 10^{-3}– 10 mbar), for the purification procedure and quantification of CO_2 concentration. The purified CO_2 was then condensed in the glass sampler (adjusted to atmospheric pressure by adding pure helium) and transferred to the mass spectrometer. The $^{13}C_{CO2}/^{12}C_{CO2}$ isotope ratio was determined using a Thermo (Finnigan) Delta Plus XP CF-IRMS connected to a Trace GC gas chromatograph and a Thermo (Finnigan) GC/C III interface. The internal accuracy of the instrument is better than 0.06‰ (standard deviation (1σ) on ten measures of reference gas) and the external precision better than 0.15‰ (standard deviation (1σ) on ten measures of the same sample. Finally, the $^{13}C_{CO2}/^{12}C_{CO2}$ is expressed in parts per mil (‰) relative to the V-PDB international standard) using the delta notation ($\delta^{13}C_{CO2}$).

Results and discussions

For the present study, 42 high-density (0.73 to 1.07 g/cm^3) pure CO_2 FI trapped in olivine (Ol), orthopyroxene (Opx), and clinopyroxene (Cpx) from mantle peridotites from the Lake Tana region (Injibara, Ethiopia) and El Hierro (Canary Islands) were analysed. [39-40] Among these, 20 FI were in Ol and Opx in mantle peridotites from the Lake Tana region, and 22 in Ol, Opx and Cpx from El Hierro. In selected peridotites from the Lake Tana region, Cpx of do not contain CO_2 FI. Only high-density pure CO_2 FI having, on average, comparable sizes (5−21 μm) and depths (5−19 μm) within the samples (cf. Table S.1), were selected for the analyses to avoid any bias on the $^{13}CO_2$ and $^{12}CO_2$ areas and area ratio measurements due to sample-generated noise, which could lead to an increased error in the calculated C_{CO2} isotopic compositions.

Validation of $^{13}CO_2$ ν_1/$^{12}CO_2$ ν_1 area ratios

Each fluid inclusion was analysed twice, collecting three times each set of 42 SS and 42 DS, for a total number of 84 sets of analyses and 256 spectra. Table 1 summarizes the average $^{13}CO_2$ ν_1 and $^{12}CO_2$ ν_1 band areas and area ratios of the three spectra collected for each set of analyses on each FI in mantle xenoliths from both localities.

In mantle xenoliths from the Lake Tana region, $^{13}CO_2$ ν_1/$^{12}CO_2$ ν_1 area ratios calculated for the 20 SS sets of analyses ranged between 0.01036 and 0.01117 in Ol, and between 0.01114 and 0.01116 in Opx, while those for the 20 DS sets of analyses span between 0.01022 and 0.01178 in Ol, and between 0.01109 and 0.01117 in Opx, respectively (Table 1). As shown in Table 1, area ratios calculated in both SS and DS set of analyses in Ol are less precise (i.e., greater area ratios interval, up to two orders of magnitude) than those in Opx, and measurements in DS span in a wider interval. These observations may suggest that bands areas measured in Ol could potentially be more affected by spectral perturbations than those in Opx. In the DS sets of analyses, calculated area ratios are more variable than those in the SS sets of analyses.

Table 1 Average $^{12}CO_2$ ν_1 and $^{13}CO_2$ ν_1 areas and average $^{13}CO_2$ ν_1/$^{12}CO_2$ ν_1 area ratios measured and calculated for single and distinct spectra of analyses CO_2 fluid inclusions.

	Host	Set of measurements	FI n	Ave $A_{12CO2v1}$ Min	Ave $A_{12CO2v1}$ Max	Ave $A_{13CO2v1}$ Min	Ave $A_{13CO2v1}$ Max	Ave $A_{13CO2v1}/A_{12CO2v1}$ Min	Ave $A_{13CO2v1}/A_{12CO2v1}$ Max	Ave $A_{13CO2v1}/A_{12CO2v1}$ Interval
Lake Tana region	Ol	SS	13	134338	172615	1500	1927	0.01036	0.01117	0.00081
		DS		134338	172615	7493	9683	0.01022	0.01178	0.00156

	Opx	SS	7	134270	161623	1499	1803	0.01114	0.01116	0.00002
		DS		134270	161623	7495	9962	0.01109	0.01117	0.00008
El Hierro	Ol	SS	6	95612	169854	1075	1767	0.01040	0.01131	0.00091
		DS		95612	169854	5358	9542	0.01108	0.01129	0.00021
	Opx	SS	10	130164	176957	1464	1987	0.01115	0.01136	0.00021
		DS		130164	176957	5005	9928	0.01092	0.01149	0.00057
	Cpx	SS	6	135320	150632	1518	1689	0.01121	0.01122	0.00000
		DS		135320	150632	7586	8255	0.01089	0.01122	0.00033

Ol = olivine; Opx = orthopyroxene; Cpx = clinopyroxene; FI = fluid inclusions; $A_{12CO2v1}$ = $^{12}CO_2$ upper band area; $A_{13CO2v1}$ = $^{13}CO_2$ upper band area; $A_{13CO2v1}/A_{12CO2v1}$ = $^{13}CO_2/^{12}CO_2$ upper bands area ratios; Ave = average; Min = Minimum; Max = Maximum; Interval = (Max – Min)/2; n = number; SS = single spectra; DS = distinct spectra.

In mantle xenoliths from El Hierro, $^{13}CO_2$ $\nu_1/^{12}CO_2$ ν_1 area ratios calculated for the 22 SS sets of measurements ranged between 0.01040 and 0.01131 in Ol, between 0.01115 and 0.01136 in Opx, and between 0.01121 and 0.01122 in Cpx. In the 22 DS sets of analyses, calculated area ratios span between 0.01108 and 0.01129 in Ol, between 0.01092 and 0.01149 in Opx, and between 0.01089 and 0.01122 in Cpx, respectively (Table 1). Again, the area ratios calculated for SS spectra in Ol are slightly less precise than those in Opx and up to two orders of magnitude less precise than those in Cpx (Table 1). For both SS and DS sets of analyses from this locality, the area ratios calculated in Ol and Opx are generally less precise than those in Cpx (Table 1). Moreover, compared with those calculated for Ol and Opx in mantle peridotites from the Lake Tana region, the precision of calculated area ratios is lower, except for area ratios measured in DS sets in Ol from El Hierro.

Among the 84 sets of measurements (42 SS and 42 DS) from both the localities, in 7 SS and 16 DS sets of measurements, at least one out the three calculated $^{13}CO_2$ $\nu_1/^{12}CO_2$ ν_1 area ratios differed from the other two by more than one order of magnitude (Table S.2), lowering the analytical precision of calculated area ratios below the third decimal place. [12, 41, 42] This erratic difference in calculated area ratios is consistent with Raman spectral perturbations due to random noise effects. [43-45] Thus, these sets have been preliminarily excluded from the database for further analysis. As a result, 17% of SS sets of measurements and 38% of DS sets were removed from the initial dataset. The significant difference in the percentage of the analyses discarded between SS and DS sets of analyses suggested that $^{13}CO_2$ ν_1 and $^{12}CO_2$ ν_1 band area measurements in distinct spectra were more easily affected by erratic noises than those measured in single ones.

For the remaining 61 sets of analyses (35 SS sets of measurements: 18 for Lake Tana inclusions and 17 for El Hierro; 26 DS sets of measurements: 15 for Lake Tana FI and 11 for El Hierro) the reproducibility of the three area ratios was evaluated based on the calculation of the *Variance‰* and

the *Reproducibility‰*, according to [Eq.1] and [Eq.2] (cf. "Raman micro-spectroscopy" section of the "Analytical methods"). Resulting *Variance‰* and *Reproducibility‰* values are summarised in Table 2.

Table 2 *Variance‰* and *Reproducibility‰* calculated in both the SS and DS sets of measurements for all the FI trapped in Ol, Opx and Cpx in mantle xenoliths from Lake Tana region (Ethiopia) and El Hierro (Canary Islands).

				Variance‰				***Reproducibility‰***			
	Host	**Set of measures**	**FI**	**Min**	**Max**	**Ave**	**Interval**	**Min**	**Max**	**Ave**	**Interval**
			n	‰	‰	‰	‰	‰	‰	‰	‰
Lake Tana region	Ol	SS	11	0.68	3.08	1.63	1.20	0.28	1.28	0.70	0.50
		DS	9	0.28	2.15	1.37	0.93	0.12	0.93	0.60	0.40
	Opx	SS	7	0.71	4.12	1.72	1.70	0.32	1.68	0.73	0.68
		DS	6	0.35	2.19	1.18	0.92	0.15	0.90	0.50	0.38
El Hierro	Ol	SS	2	1.73	2.00	1.86	0.14	0.73	0.83	0.78	0.05
		DS	4	1.05	10.32	5.32	4.54	0.44	4.39	2.30	1.97
	Opx	SS	9	0.40	13.42	3.53	6.51	0.16	5.93	1.53	2.88
		DS	3	0.54	10.88	4.50	5.17	0.22	4.44	1.86	2.11
	Cpx	SS	6	0.36	1.91	1.12	0.78	0.15	0.81	0.47	0.33
		DS	4	0.29	1.23	0.73	0.47	0.12	0.50	0.31	0.19

Ol = olivine; Opx = orthopyroxene; Cpx = clinopyroxene; n = number; Min = Minimum; Max = Maximum; Ave = Average; Interval = (Max.-Min.)/2; SS = single spectra; DS = distinct spectra.

In mantle xenoliths from the Lake Tana region, on average, the *Variance‰* calculated for the three area ratios in each SS set of measurements was 1.63±1.20‰ in Ol, and to 1.72±1.70‰ in Opx, while the *Reproducibility‰* was 0.70±0.50‰ in Ol, and 0.73±0.68‰ in Opx (Table 2). The *Variance‰* calculated for the three area ratios in each DS set of measurements, on the other hand, was 1.37±0.93‰ in Ol, and to 1.18±0.92‰ in Opx, while the *Reproducibility‰* was equal to 0.60±0.40‰ in Ol, and 0.50±0.38‰ in Opx (Table 2). Although for both the sets of measurements the *Variance‰* and the *Reproducibility‰* were always lower than ≈2.00 and ≈1.00‰, respectively, the reproducibility of the remaining 15 DS sets of analyses for the peridotites from the Lake Tana region is always better than that calculated for the remaining 18 SS ones.

In mantle xenoliths from El Hierro, on average, the *Variance‰* calculated for the three area ratios in each SS set of measurements was 1.86±0.14‰ in Ol, to 3.53±6.51‰ in Opx, and 1.12±0.78‰ in Cpx, while the *Reproducibility‰* was 0.78±0.05‰ in Ol, 1.53±2.88‰ in Opx, and 0.47±0.33‰ in Cpx (Table 2). The *Variance‰* calculated for the three area ratios in each DS set of measurements

was 5.32±4.54‰ in Ol, 4.50±5.17‰ in Opx, and 1.23±0.73‰ in Cpx, while the *Reproducibility‰* was 2.30±1.97‰ in Ol, 1.86±2.11‰ in Opx, and 0.31±0.19‰ in Cpx (Table 2). Although most of the *Variance‰* and the *Reproducibility‰* values calculated for Ol and Opx in both SS and DS sets of measurements were lower than ≈3.00 and ≈1.00‰, the average calculated values are affected by the presence of 4 sets of analyses (2 DS in Ol, 1 SS and 1 DS in Opx) where the *Variance‰* and the *Reproducibility‰* were higher than 5 and 3‰, respectively (cf. Table S.3). These analyses are characterised by one area ratio that differs from the other two by about 0.00005, leading to uncertainty in the analytical precision between the third and the fourth decimal place. Again, the erratic variation of a single area ratio among the three acquired for the same set of analyses could be related to random noise effects, which cannot be removed from spectra. [43-45]

The DS sets of analyses performed in FI in mantle xenoliths from El Hierro were characterised by slightly better precision than the SS sets. This feature is observed in mantle xenoliths from both localities, indicating that $^{13}CO_2$ ν_1/$^{12}CO_2$ ν_1 calculated based on the DS sets of analyses are more precise than those based on SS sets. This is consistent because, due to the prolonged acquisition times, the amount of collected signal for the $^{13}CO_2$ ν_1 and the $^{12}CO_2$ ν_1 is greater, allowing band areas to be measured with higher precision. However, the reproducibility of SS and DS area ratios is comparable. Thus, there is no advantage to using the analytical procedure adopted to collect DS sets of measures compared to those used for SS analyses.

Except for a few sets of measurements, in 97% of the SS sets of analyses and 88% of the DS sets, the reproducibility was better than 4‰. Similar values, coupled with a precision of the area ratios in the fourth decimal place, indicate that the method could theoretically be applied to determine the $\delta^{13}C_{CO2}$‰ with a precision sufficient to distinguish between various C_{CO2} reservoirs in the Earth system.

Calculation of FI $\delta^{13}C_{CO2}$‰ values

$\delta^{13}C_{CO2}$‰ values for FI from both the localities were calculated based on the average of the three area ratios of each set of measurements, according to [eq. S.3] (Figs. 2 and 3; cf. Supplementary note S.1 and Table S.4). Figures 2 a and b compare $\delta^{13}C_{CO2}$‰ values calculated from both the SS and DS sets of analyses. As expected, based on the calculated reproducibility, at both the localities, the $\delta^{13}C_{CO2}$‰ values are generally more precise when calculated for DS sets of measurements (Fig.2a, b). However, on average, $\delta^{13}C_{CO2}$‰ values calculated from SS sets of measurements are similar to those based on DS sets. Thus, for FI whose isotopic composition was determined using both SS and the DS sets of measurements (13 FI from the Lake Tana region, and 8 from El Hierro), only those

having lower error and 1σ have been selected as the most representative for the CO_2 FI carbon isotopic composition. Based on this, the $\delta^{13}C_{CO2}$‰ values of 40 FI have been reported. For both the SS and DS sets of measurements, no variations of the $\delta^{13}C_{CO2}$‰ depending on the density of the fluid inclusions have been observed.

Table 3 summarizes the $\delta^{13}C_{CO2}$‰ values calculated for the 40 FI, separated according to sample and mineral host for both localities.

On average, $\delta^{13}C_{CO2}$‰ values were -6.73±1.04‰ (-7.60−-5.53‰; 1σ=±0.64‰) for FI in Ol, and -7.34±0.81‰ (-8.16−-6.53‰; 1σ=±0.48‰) for FI in Opx from the Lake Tana region (Ethiopia; Table 3). In mantle xenoliths from El Hierro (Canary Islands), the average $\delta^{13}C_{CO2}$‰ values were 2.40±2.42‰ (0.01−5.12‰; 1σ=±2.03‰) for FI in Ol, 0.92±6.45‰ (-1.89−11.01‰; 1σ=±3.52‰) for FI in Opx, and -1.87±0.39‰ (-2.12−-1.34‰; 1σ=±0.25‰) for FI in Cpx (Table 3). The C_{CO2} isotopic compositions determined for FI in Ol and Opx in mantle xenoliths from El Hierro are characterised by more significant error and 1σ compared to those in Lake Tana xenoliths, indicating a generally lower precision (Table 3). The C_{CO2} isotopic compositions of FI in Ol and Opx in mantle xenoliths from El Hierro are influenced by one set of analyses in Ol, where the calculated $\delta^{13}C_{CO2}$‰ value, error and 1σ are almost two times larger than the others (XML11_FI24, $\delta^{13}C_{CO2}$=4.85±3.65‰, 1σ=±3.31‰; Fig.3b, cf. Table S.4), and one set of analyses in Opx, where the calculated $\delta^{13}C_{CO2}$‰ value differs by a significant amount from all the others, having an error and 1σ greater than 5‰ (XML11_FI18, $\delta^{13}C_{CO2}$=11.01±6.78‰, 1σ=±5.99‰; Fig. 3b, cf. Table S.4). Without these two "outliers", 75% of the calculated $\delta^{13}C_{CO2}$‰ values for FI in Ol fall in the range 1.58±1.95‰ (0.01−3.91‰, 1σ=±1.68‰; cf. Table S.4), while 90% of those in Opx are in the range -0.20±1.67‰ (-1.89−1.45‰, 1σ=±1.11‰; cf. Table S.4).

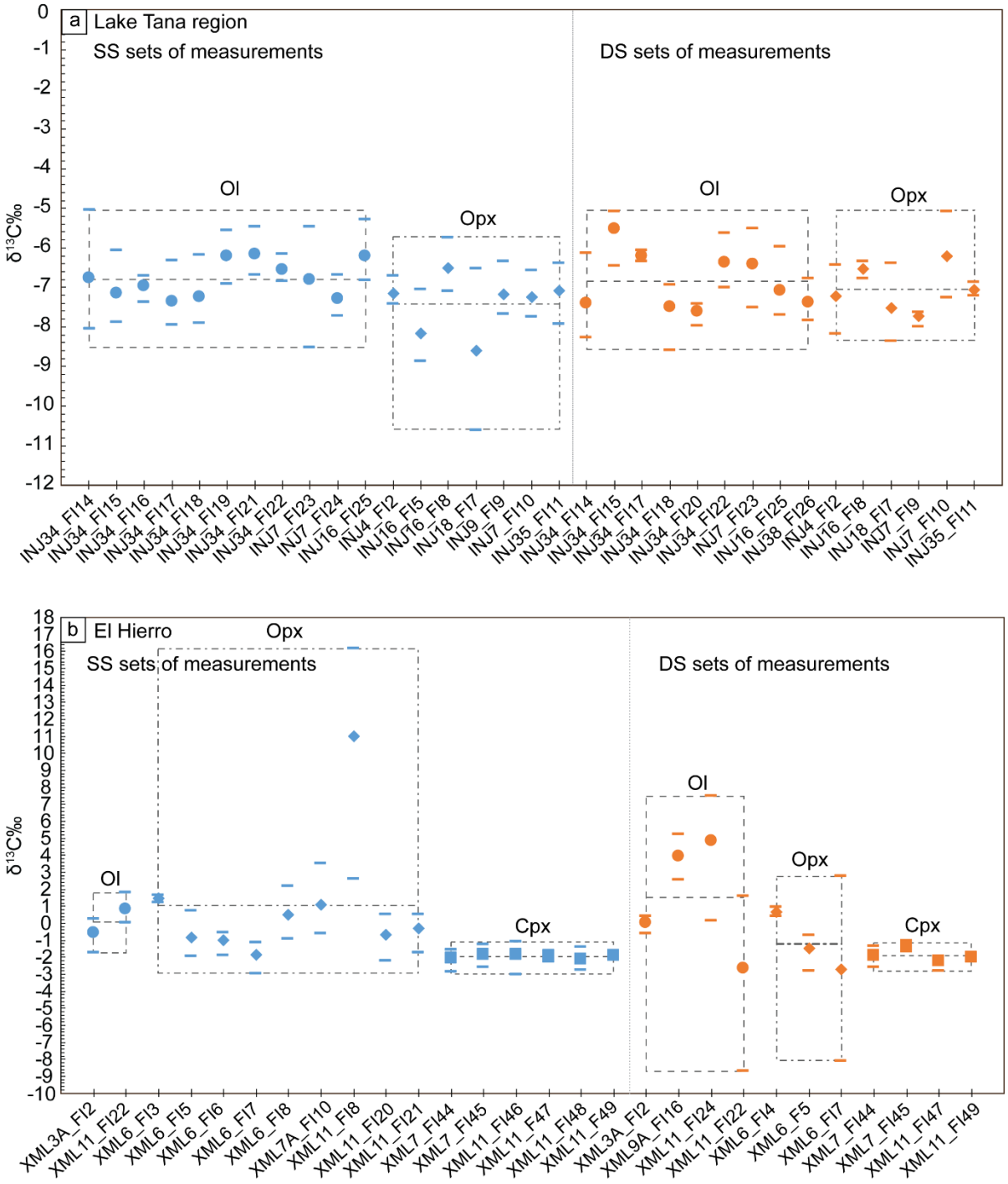

Figure 2. Raman-calculated $\delta^{13}C_{CO2}$‰ values for the SS (blue) and the DS (orange) sets of measurements of all the CO_2 fluid inclusions trapped in Ol (circles), Opx (diamonds) and Cpx (triangles) in peridotite sample from (a) the Lake Tana region (Ethiopia), and (b) El Hierro (Canary Islands). The thick dashed grey lines represent the maximum, the minimum and the average $\delta^{13}C_{CO2}$‰ values calculated for a single mineral phase in SS and DS sets of analyses.

Table 3 $\delta^{13}C_{CO2}$‰ values based on Raman micro-spectroscopic analysis of fluid inclusions trapped in Ol, Opx and Cpx in mantle xenoliths from the Lake Tana region (Ethiopia) and El Hierro (Canary Islands).

Host	Samples	$\delta^{13}C_{CO2}$

			Analyses	Min	Max	Ave	Error	1σ
			n	‰	‰	‰	‰	‰
Lake Tana Region	Ol	INJ34	9	-7.60	-5.53	-6.75	1.04	0.68
	Ol	INJ7	2	-7.29	-6.42	-6.86	0.43	0.43
	Ol	INJ16	1	-	-	-	-	-
	Ol	INJ38	1	-	-	-	-	-
	Tot. Ol		***13***	***-7.60***	***-5.53***	***-6.73***	***1.04***	***0.64***
	Opx	INJ4	1	-	-	-	-	-
	Opx	INJ7	2	-7.74	-7.24	-7.49	0.25	0.25
	Opx	INJ16	2	-8.16	-6.53	-7.34	0.81	0.81
	Opx	INJ18	1	-	-	-	-	-
	Opx	INJ35	1	-	-	-	-	-
	Tot. Opx		***7***	***-8.16***	***-6.53***	***-7.34***	***0.81***	***0.48***
El Hierro	Ol	XML3	1	-	-	0.01	-	-
	Ol	XML9	1	-	-	3.91	-	-
	Ol	XML11	2	0.82	4.85	2.83	2.01	2.01
	Tot. Ol		***4***	***0.01***	***4.85***	***2.40***	***2.42***	***2.03***
	Opx	XML6	6	-1.89	1.45	-0.30	1.67	1.23
	Opx	XML7	1	-	-	1.09	-	-
	Opx	XML11	3	-0.71	11.01	3.32	5.86	5.44
	Tot. Opx		***10***	***-1.89***	***11.01***	***0.92***	***6.45***	***3.52***
	Cpx	XML7	2	-1.91	-1.34	-1.63	0.29	0.29
	Cpx	XML11	4	-2.12	-1.89	-1.99	0.12	0.09
	Tot. Cpx		***6***	***-2.12***	***-1.34***	***-1.87***	***0.39***	***0.25***

Reported $\delta^{13}C_{CO2}$‰ values correspond to the mean isotopic compositions for all of the fluid inclusions within the same host mineral; Ol = olivine; Opx = orthopyroxene; Cpx = clinopyroxene; n = number of FI analyzed; Min = Minimum; Max = Maximum; Ave = Average; Error = (Max.-Min.)/2; Tot. = total.

In both the localities, calculated $\delta^{13}C_{CO2}$‰ values were higher, on average, for fluid inclusions in Ol compared to those in Opx and Cpx, and, in turn, $\delta^{13}C_{CO2}$‰ values in Opx were, on average, higher than those in Cpx. This suggests a possible dependence of the Raman spectral features and the calculated $\delta^{13}C_{CO2}$‰ on the FI host mineral phase. This hypothesis, however, requires further investigation. For 95% of the analyses, the precision of $\delta^{13}C_{CO2}$‰ values was better than ±2‰ but was generally lower for FI trapped in El Hierro mantle xenoliths. Similar precision is one order of magnitude better than that achieved by previous studies, [33-38] suggesting that Raman micro-spectroscopy could be a valid C_{CO2} "mass-spectrometric" technique.

The C_{CO2} isotopic compositions calculated for FI in mantle xenoliths from the Lake Tana region fall within the "MORB-like Upper Mantle" field (-8‰<$\delta^{13}C$<-4‰ [50]; Fig. 3a), and this is consistent with the inferred trapping conditions of the CO_2 fluids studied by Frezzotti et al. (2010) [40] for the

Ethiopian lithospheric mantle environment. Carbon isotopic composition determined for FI in mantle xenoliths from El Hierro, however, was unexpectedly higher than those reported for the "MORB-like Upper Mantle" field (Fig. 3b). [39]

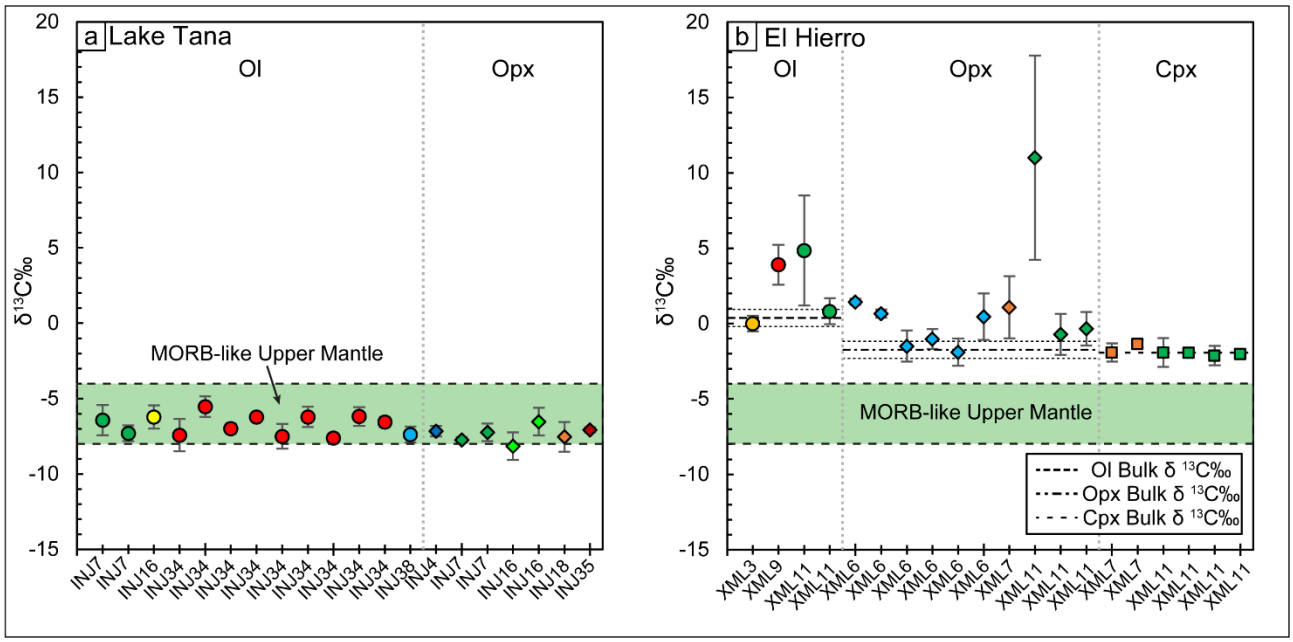

Figure 3. Raman-calculated $\delta^{13}C_{CO2}$ values for CO_2 fluid inclusions trapped in Ol (circles), Opx (diamonds) and Cpx (triangles) in peridotite samples from (a) the Lake Tana region (Ethiopia), and (b) El Hierro (Canary Islands). Analysed inclusions are divided by sample and are provided with the error bars. The thick horizontal dashed black lines additionally observable for El Hierro measurements represent the mean bulk $\delta^{13}C_{CO2}$ values obtained by mass spectrometry for comparison. The thin dotted black lines represent the error interval for bulk Ol and Opx for El Hierro. The green field delimitates the "MORB-like Upper Mantle" carbon isotopic range (-8‰<δ^{13}C<-4‰ [50]). Ol = olivine; Opx = orthopyroxene; Cpx = clinopyroxene.

Despite the good analytical reproducibility (< 4‰) and high precision of the C_{CO2} isotopic compositions (≤≈2.00‰), $\delta^{13}C_{CO2}$‰ values were obtained without validation of the analytical procedure by analyzing a $\delta^{13}C_{CO2}$‰ standard for comparison. For this reason, the accuracy of the C_{CO2} isotopic composition has been tested on fluid inclusions trapped in mantle xenoliths from El Hierro by performing bulk $\delta^{13}C_{CO2}$‰ measurements. The C_{CO2} isotopic signature of the CO_2 fluids was determined by conventional ratio mass spectrometry for Ol, Opx and Cpx from 4 peridotite xenoliths from El Hierro (Table 4). Measured CO_2 abundances ranged from $1.3x10^{-8}$ mol/g to $5.5x10^{-8}$ mol/g (mean=$3.5x10^{-8}\pm2.1x10^{-8}$ mol/g) in Ol, from $2.5x10^{-7}$ mol/g to $5.1x10^{-7}$ mol/g (mean=$3.5x10^{-7}\pm9.8x10^{-8}$ mol/g) in Opx, and were $9.5x10^{-7}$ mol/g in Cpx. Corresponding CO_2 $\delta^{13}C$ values ranged (Table 4; Fig. 3b) from -0.19‰ and 0.96‰ (mean= 0.38‰±0.58‰; 1σ=±0.58‰) for Ol and from -2.38‰ to -1.23‰ (mean=-1.75±0.58‰; 1σ=±0.45‰) for Opx, and are equal to -1.94‰ in Cpx.

Table 4 CO_2 abundances and carbon isotopic composition measured for Ol, Opx and Cpx in four mantle xenoliths from El Hierro (Canary Islands).

		CO_2 concentration				**$\delta^{13}C_{CO2}$**		
Host	**Sample**	**Ave.**	**1σ**	**Min**	**Max**	**Ave**	**Error**	**1σ**
		mol/g	mol/g	‰	‰	‰	‰	‰
Ol	XML11	5.5E-08	-	-	-	0.96	-	-
Ol	XML7	1.3E-08	-	-	-	-0.19	-	-
Tot. Ol		***3.5E-08***	***2.1E-08***	***-0.19***	***0.96***	***0.38***	***0.58***	***0.58***
Opx	XML6	2.7E-07	-	-	-	-1.43	-	-
Opx	XML11	2.8E-07	-	-	-	-1.23	-	-
Opx	1.3	5.1E-07	-	-	-	-1.94	-	-
Opx	XML7	3.6E-07	-	-	-	-2.38	-	-
Tot. Opx		***3.54E-07***	***9.74E-08***	***-2.38***	***-1.23***	***-1.75***	***0.58***	***0.45***
Cpx	1.3	9.47E-07	-			-1.94		-

Ol = olivine; Opx = orthopyroxene; Cpx = clinopyroxene; Min = Minimum; Max = Maximum; Ave = average; Error = (Max-Min)/2.

Notably, the majority (65%) of the $\delta^{13}C_{CO2}$‰ values determined by Raman micro-spectroscopy in all mineral phases agree with the bulk average $\delta^{13}C_{CO2}$‰ values obtained by mass spectrometry (Fig. 3a). Among these, Raman-based C_{CO2} isotopic compositions of FI in Ol and Opx are characterised by comparable (i.e., overlapping) but slightly lower precision (Raman-based $\delta^{13}C_{CO2}$‰ analytical error≈±1.80‰ vs bulk $\delta^{13}C_{CO2}$‰ analytical error=±0.58‰; Fig. 3b), while those in Cpx have the same order of precision as bulk mass spectrometric analyses (Raman based $\delta^{13}C_{CO2}$‰ analytical error=±0.38‰ in Cpx, average bulk $\delta^{13}C_{CO2}$‰ analytical error=±0.58‰; Fig. 3b). Moreover, with both the techniques, measured $\delta^{13}C_{CO2}$‰ values were, on average, higher in Ol and lower in Opx and Cpx.

Results presented here represent a significant advance in the application of Raman micro-spectroscopy for determining the carbon isotopic composition of CO_2 in natural FI. Present results indicate that this technique not only can determine $\delta^{13}C_{CO2}$‰ values with sufficient accuracy to reliably discriminate between natural $\delta^{13}C_{CO2}$‰ reservoirs, [12, 41, 42] and also have the potential to trace variations in the isotopic composition at the mineral scale by examining FI from different growth zones within crystals.

A subordinate number (35%) of FI in Ol and Opx in mantle xenoliths from El Hierro (Canary Islands) measures on average higher $\delta^{13}C_{CO2}$‰ values compared to the average bulk C_{CO2} isotopic compositions obtained for the FI trapped in the same mineral phases (Fig. 3b). These analyses are generally characterised by analytical errors ranging from ≈±0.30‰ to ≈±7.00‰ (cf. Table S.4), and

contribute to lowering of both the precision (up to ≈±7.00‰) and the accuracy of the $\delta^{13}C_{CO2}$‰ values based on Raman micro-spectroscopy (Table 3). It may not be possible to avoid such erratic effects to Raman measurements and calculated isotopic compositions.

Summary and conclusions

In the present study, the applicability of Raman micro-spectroscopy to measure the carbon isotopic composition of natural CO_2 FI is evaluated. Raman micro-spectrometric analyses on CO_2 fluid inclusions trapped in mantle peridotitic xenoliths from the Lake Tana region (Ethiopia) and El Hierro (Canary Islands) have been performed.

Results show that 95% of the $\delta^{13}C_{CO2}$‰ values, calculated for 40 fluid inclusions from both localities, are characterised by an analytical error of ≤≈2.00‰. This constitutes a significant improvement of the C_{CO2} isotopic composition precision compared to that reported in previous studies, [33-38] allowing the discrimination between different natural CO_2 reservoirs in the Earth system.

Mass spectrometric $\delta^{13}C_{CO2}$‰ analysis of fluid inclusions trapped in mantle xenoliths from El Hierro confirmed that, in most of the cases, Raman-based $\delta^{13}C_{CO2}$‰ values reflect the C_{CO2} isotopic composition of fluids within single fluid inclusions at the mineral scale. Despite the limitations of Raman micro-spectroscopy due to erratic and unpredictable analytical errors, the achieved C_{CO2} isotopic composition precision and accuracy prove that this technique represents an acceptable *in situ* and non-destructive complementary method to classical mass spectrometry.

Overall, the presented work proves that Raman micro-spectroscopy is a promising technique for the *in situ* determination of the C_{CO2} isotopic compositions in mantle fluid inclusions.

References

1. P. Deines, Early Organic Evolution, Schidlowski M., Golubic S., Kimberley M.M., McKirdy D.M., Trudinger P.A. (eds). Springer, Berlin, Heidelberg; https://doi.org/10.1007/978-3-642-76884-2_10 (1992).

2. Mason, E., Edmonds, M., and Turchyn, A. V. Remobilization of crustal carbon may dominate volcanic arc emissions. Science 357(6348), 290-294; https://doi.org/10.1126/science.aan5049 (2017).

3. Plank, T., and Manning, C. E. Subducting carbon. *Nature* **574**(7778), 343-352; https://doi.org/10.1038/s41586-019-1643-z (2019).

4. Aiuppa, A., Fischer, T. P., Plank, T., and Bani, P. CO_2 flux emissions from the Earth's most actively degassing volcanoes, 2005–2015. *Sci. Rep*, **9**(1), 1-17; https://doi.org/10.1038/s41598-019-41901-y (2019).

5. Craig, H. Isotopic standards for carbon and oxygen and correction factors for mass-spectrometric analysis of carbon dioxide. *Geochim. Cosmochim. Acta* **12**, 133-149; https://doi.org/10.1016/0016-7037(57)90024-8 (1957).

6. Deines, P., and Gold, D. P. The isotopic composition of carbonatite and kimberlite carbonates and their bearing on the isotopic composition of deep-seated carbon. *Geochim. Cosmochim. Acta* **37**(7), 1709-1733; https://doi.org/10.1016/0016-7037(73)90158-0 (1973).

7. Pineau, F., and Javoy, M. Carbon isotopes and concentrations in mid-oceanic ridge basalts. *Earth Planet. Sci. Lett.* **62**(2), 239-257; https://doi.org/10.1016/0012-821X(83)90087-0 (1983).

8. Exley, R. A., Mattey, D. P., Clague, D. A., and Pillinger, C. T. Carbon isotope systematics of a mantle "hotspot": a comparison of Loihi Seamount and MORB glasses. *Earth Planet. Sci. Lett.* **78**(2-3), 189-199; https://doi.org/10.1016/0012-821X(86)90060-9 (1986).

9. Boutton, T. W. Stable carbon isotope ratios of natural materials: I. Sample preparation and mass spectrometric analysis. In *Carbon Isotope Techniques*, D. C. Coleman and B. Fry, Eds. (Academic Press Inc., San Diego), pp. 155–185 (1991a).

10. Boutton, T. W. Stable carbon isotope ratios of natural materials: 2. Atmospheric, terrestrial, marine, and freshwater environments. In *Carbon Isotope Techniques*, D. C. Coleman and B. Fry, Eds. (Academic Press Inc., San Diego), pp. 155–185 (1991b).

11. Deines, P. The carbon isotope geochemistry of mantle xenoliths. *Earth Sci. Rev.* **58**, 247-278; https://doi.org/10.1016/S0012-8252(02)00064-8 (2002).

12. Sharp, Z. "Principles of Stable Isotope Geochemistry, 2nd Edition." (2017). https://doi.org/10.25844/h9q1-0p82

13. Roedder, E. Fluid inclusions. Reviews in Mineralogy, vol. 12. Mineral. Soc. Am., Washington, DC, pp. 503–532, Chap. 12. (1984).

14. Andersen, T., and Neumann, E. R. Fluid inclusions in mantle xenoliths. *Lithos* **55**(1-4), 301-320; https://doi.org/10.1016/S0024-4937(00)00049-9 (2001).

15. Frezzotti, M. L., and Touret, J. L.. CO_2, carbonate-rich melts, and brines in the mantle. *Geosci. Front.* **5**(5), 697-710; https://doi.org/10.1016/j.gsf.2014.03.014 (2014).

16. McKinney, C. R., McCrea, J. M., Epstein, S., Allen, H. A., and Urey, H. C. Improvements in mass spectrometers for the measurement of small differences in isotope abundance ratios. *Rev. Sci. Instrum.* **21**(8), 724-730; https://doi.org/10.1063/1.1745698 (1950).

17. Muccio, Z., and Jackson, G. P. Isotope ratio mass spectrometry. *Analyst*, **134**(2), 213-222; https://doi.org/10.1039/B808232D (2009).

18. Correale, A., Paonita, A., Rizzo, A., Grassa, F., and Martelli, M. The carbon-isotope signature of ultramafic xenoliths from the Hyblean Plateau (southeast Sicily, Italy): Evidence of mantle heterogeneity. *Geochem., Geophy. Geosy.* **16**, 600-611; https://doi.org/10.1002/2014GC005656 (2015).

19. Gennaro, M. E., Grassa, F., Martelli, M., Renzulli, A., and Rizzo, A. L. Carbon isotope composition of CO_2-rich inclusions in cumulate-forming mantle minerals from Stromboli volcano (Italy). *J. Volcanol. Geoth. Res.* **346**, 95-103; https://doi.org/10.1016/j.jvolgeores.2017.04.001 (2017).

20. Rizzo, A. L., Pelorosso, B., Coltorti, M., Ntaflos, T., Bonadiman, C., Matusiak-Małek, M., ... and Bergonzoni, G. Geochemistry of noble gases and CO_2 in fluid inclusions from lithospheric mantle beneath Wilcza Góra (Lower Silesia, southwest Poland). *Front. Earth Sci.* **6**, 215; https://doi.org/10.3389/feart.2018.00215 (2018).

21. Des Marais, D. J., and Moore, J. G. Carbon and its isotopes in mid-oceanic basaltic glasses. *Earth Planet. Sci. Lett.* **69**, 43-57; https://doi.org/10.1016/0012-821X(84)90073-6 (1984).

22. Mattey, D. P., Carr, R. H., Wright, I. P., and Pillinger, C. T. Carbon isotopes in submarine basalts. *Earth Planet. Sci. Lett.* **70**, 196-206; https://doi.org/10.1016/0012-821X(84)90005-0 (1984).

23. Burke, E. A. Raman microspectrometry of fluid inclusions. *Lithos*, **55**, 139-158; https://doi.org/10.1016/S0024-4937(00)00043-8 (2001).

24. Frezzotti, M. L., Tecce, F., and Casagli, A. Raman spectroscopy for fluid inclusion analysis. *J. of Geochem. Explor.* **112**, 1-20; https://doi.org/10.1016/j.gexplo.2011.09.009 (2012).

25. Dubessy, J., Caumon, M. C., Rull, F., and Sharma, S. Instrumentation in Raman spectroscopy: elementary theory and practice. *In Raman spectroscopy applied to earth sciences and cultural heritage, 12, 83-172.* (2012).

26. Bodnar, R. J., and Frezzotti, M. L. Microscale chemistry: Raman analysis of fluid and melt inclusions. *Elements* **16**(2), 93-98; https://doi.org/10.2138/gselements.16.2.93 (2020).

27. Gordon, H. R., and McCubbin Jr, T. K. The 2.8-micron bands of CO_2. *J. Mol. Spectrosc.* **19**, 137-154; https://doi.org/10.1016/0022-2852(66)90237-2 (1966).

28. Finsterhölzl, H. Raman Spectra of Carbon Dioxide and Its Isotopic Variants in the Fermi Resonance Region: Part III. Analysis of Rovibrational Intensities for $^{12}C^{16}O_2$, $^{13}C^{16}O_2$, $^{12}C^{18}O_2$ and $^{12}C^{16}O^{18}O$. *Ber. Bunsenges. Phys. Chem.* **86**(9), 797-805; https://doi.org/10.1002/bbpc.19820860907 (1982).

29. Schrötter H.W., Klöckner H.W. Raman Scattering Cross Sections in Gases and Liquids. In: *Raman Spectroscopy of Gases and Liquids*, Weber A. (eds). Topics in Current Physics, vol 11. Springer, Berlin, Heidelberg. https://doi.org/10.1007/978-3-642-81279-8_4 (1979).

30. Dhamelincourt, P., Beny, J. M., Dubessy, J., and Poty, B. Analyse d'inclusions fluides à la microsonde MOLE à effet Raman. *B. Mineral.* **102**, 600-610; https://doi.org/10.3406/bulmi.1979.7309 (1979).

31. Bertrán, J. F. Study of the Fermi doublet ν_1—$2\nu_2$ in the Raman spectra of CO_2 in different phases. *Spectrochim. Acta A.-M.* **39**, 119-121; https://doi.org/10.1002/jrs.1250200705 (1983).

32. Dubessy, J., Poty, B., and Ramboz, C. Advances in COHNS fluid geochemistry based on micro-Raman spectrometric analysis of fluid inclusions. *Eur. J. Mineral.* **1**, 517-534; DOI: 10.1127/ejm/1/4/0517 (1989).

33. Rosasco, G. J., Roedder, E., and Simmons, J. H. Laser-excited Raman spectroscopy for non-destructive partial analysis of individual phases in fluid inclusions in minerals. *Science* 557-560; https://www.jstor.org/stable/1740436 (1975).

34. Marshall, D., Pfeifer, H. R., and Sharp, Z. A re-evaluation of Raman as a tool for the determination of ^{12}C and ^{13}C in geological fluid inclusions. *Analysis* **22**, M38-M41 (1994).

35. Arakawa, M., Yamamoto, J., and Kagi, H. Developing micro-Raman mass spectrometry for measuring carbon isotopic composition of carbon dioxide. *Appl. Spectrosc.* **61**, 701-705; https://doi.org/10.1366/000370207781393244 (2007).

36. Li, J., Li, R., Zhao, B., Wang, N., and Cheng, J. Quantitative analysis and measurement of carbon isotopic compositions in individual fluid inclusions by micro-laser Raman spectrometry. *Anal. Methods*. **8**, 6730-6738. https://doi.org/10.1039/C6AY01897A (2016).

37. Li, J., Li, R., Zhao, B., Guo, H., Zhang, S., Cheng, J., and Wu, X. Quantitative measurement of carbon isotopic composition in CO_2 gas reservoir by Micro-Laser Raman spectroscopy. *Spectrochim. Acta A.-M.* **195**, 191-198; https://doi.org/10.1016/j.saa.2018.01.082 (2018).

38. Yokokura, L., Hagiwara, Y., and Yamamoto, J. Pressure dependence of micro-Raman mass spectrometry for carbon isotopic composition of carbon dioxide fluid. *J. Raman Spectrosc.* **51**, 997-1002; https://doi.org/10.1002/jrs.5864 (2020).

39. Oglialoro, E., Frezzotti, M. L., Ferrando, S., Tiraboschi, C., Principe, C., Groppelli, G., and Villa, I. M. Lithospheric magma dynamics beneath the El Hierro Volcano, Canary Islands: insights from fluid inclusions. *Bull. Volcanol.* **79**(10), 70. https://doi.org/10.1007/s00445-017-1152-6 (2017).

40. Frezzotti, M. L., Ferrando, S., Peccerillo, A., Petrelli, M., Tecce, F., and Perucchi, A. Chlorine-rich metasomatic H2O–CO2 fluids in amphibole-bearing peridotites from Injibara (Lake Tana region, Ethiopian plateau): nature and evolution of volatiles in the mantle of a region of continental flood basalts. *Geoch. Cosmochim. Acta* **74**(10), 3023-3039; https://doi.org/10.1016/j.gca.2010.02.007 (2010).

41. Hayes, J. M. An introduction to isotopic calculations. Woods Hole Oceanographic Institution, Woods Hole, MA, 2543; (2004).

42. Zare, R. N., Kuramoto, D. S., Haase, C., Tan, S. M., Crosson, E. R., and Saad, N. M. High-precision optical measurements of 13C/12C isotope ratios in organic compounds at natural abundance. *P. Natl. Acad. Sci. Usa*, **106**(27), 10928-10932; https://doi.org/10.1073/pnas.0904230106 (2009).

43. McCreery, R. L. Raman spectroscopy for chemical analysis. *Meas.t sci. technol.* **12**(5), 653; (2001).

44. Pelletier, M. J. Quantitative Analysis Using Raman Spectrometry. *Appl. Spectrosc*. **57**, 20A-42A; https://www.osapublishing.org/as/abstract.cfm?URI=as-57-1-20A (2003).

45. Barton, S. J., Ward, T. E., and Hennelly, B. M. Algorithm for optimal denoising of Raman spectra. *Anal. Methods* **10**(30), 3759-3769; https://doi.org/10.1039/C8AY01089G (2018).

46. Yuan, X., and Mayanovic, R. A. An empirical study on Raman peak fitting and its application to Raman quantitative research. *Appl. Spectrosc*. **71**, 2325-2338; https://doi.org/10.1177/0003702817721527 (2017).

47. Wojdyr, M. Fityk: a general-purpose peak fitting program. *J. Appl. Crystallogr*. **43**, 1126-1128; https://doi.org/10.1107/S0021889810030499 (2010).

48. Remigi, S., Mancini, T., Ferrando, S., and Frezzotti, M. L. Inter-Laboratory Application of Raman CO_2 Densimeter Equations: Experimental Procedure and Statistical Analysis Using Bootstrapped Confidence Intervals. *Appl. Spectrosc.* 0003702820987601. https://doi.org/10.1177/0003702820987601 (2021).

49. Fall, A., Tattitch, B., and Bodnar, R. J. Combined microthermometric and Raman spectroscopic technique to determine the salinity of H_2O–CO_2–NaCl fluid inclusions based on clathrate melting. *Geochim. Cosmochim. Acta*. **75**(4), 951-964. https://doi.org/10.1016/j.gca.2010.11.021 (2011).

50. Mattey, D. P., Exley, R. A., and Pillinger, C. T. Isotopic composition of CO_2 and dissolved carbon species in basalt glass. *Geochim. Cosmochim. Acta*. **53**, 2377-2386; https://doi.org/10.1016/0016-7037(89)90359-1 (1989).

6.1 Supplementary Material

6.1.1 Supplementary note S.1

The areas of the peaks identifying a certain gas specie in a Raman spectrum depend by the mass of the gas within the system. [1-5] For fluid inclusions studies, the relation between the peaks' areas in a Raman spectrum with the relative molar proportion of a gas it is expressed by the equation [eq. S.1]: [5]

$$X_i = [A_i/(\sigma_i * \zeta_i)]/\sum[A_n/(\sigma_n * \zeta_n)] \qquad \text{[eq. S.1]}$$

Where X_i is the molar fraction of the gas component i, A_i and A_n the peak area of component i and all the components n measured within the CO_2 Raman spectrum; $\sigma_i, \sigma_n, \zeta_i$ and ζ_n are the Raman scattering independent cross section and the instrumental efficiency for the gas component i and for all the gas components n, respectively.

In the case of the Raman spectrum of the CO_2, from [eq. S.1] it is possible to derive the equation [eq. S.3] for the calculation of the ratio of the relative concentrations of the $^{12}CO_2$ and the $^{13}CO_2$ isotopologues within a certain CO_2 fluid inclusion as:

$$\frac{X_{13CO2}}{X_{12CO2}} = \frac{A_{13CO2\ \nu1}}{A_{12CO2\ \nu1}} * \frac{F_{12CO2\ \nu1}}{F_{13CO2\ \nu1}} \qquad \text{[eq. S.2]}$$

Since for the upper bands of the two CO_2 isotopologues, the $\frac{F_{12CO2\ \nu1}}{F_{13CO2\ \nu1}}$ ratio is equal to 1, $\frac{X_{13CO2}}{X_{12CO2}} = \frac{A_{13CO2}}{A_{12CO2}}$. [5, 6]

This relation could be used to express the concentration of the $^{13}C_{CO2}/^{12}C_{CO2}$ within the analysed fluid inclusion and, thus, to calculate the CO_2 isotopic signature of single fluid inclusions according to equation [eq. S.3]:

$$\delta^{13}C_{CO2} = \left\{\left[\frac{\left(\frac{A_{13CO2\ \nu1}}{A_{12CO2\ \nu1}}\right)_{FI}}{\left(\frac{C_{13CO2}}{C_{12CO2}}\right)_{PDB}}\right] - 1\right\} * 1000 \qquad \text{[eq. S.3]}$$

where $\left(\frac{C_{13CO2}}{C_{12CO2}}\right)_{PDB}$ is the carbon isotopic ratio of the standard Vienna Pee Dee Belemnite.

6.1.2 Supplementary note S.2

For all the acquired spectra, the baseline has been corrected based on the least-squares method, by manually specifying the points of the spectral background which had to be removed. [7] At the base of the $^{13}CO_2$ ν_1 and the $^{12}CO_2$ ν_1, the baseline points to be removed have been placed where a change in the polarity of the spectrum was observed. In the case of the $^{13}CO_2$ ν_1, these were placed around 1365±0.2 and 1372±0.2 cm^{-1}, while for the $^{12}CO_2$ one at about 1371±0.03 and 1399±0.03 cm^{-1} (Fig.9g). Once the baseline has been removed, the bands fitting has been performed using a Split-Pseudo Voight fitting function which allows minimizing any over- and/or underestimation of the band areas of symmetric vibrations due to small asymmetries of the profiles. [8, 9] In order to achieve the best fitting as possible, bands parameters such as the shape, the intensity and the full width at half maximum (FWHM) have been corrected in order to minimize the fitting residuals and, thus, reaching the best R^2 coefficients as possible, indicating a good overlapping between raw and modelled bands (Fig.9c, d, e, f, and g). For the $^{12}CO_2$ ν_1 the best R^2 coefficients (mostly around 0.998 and 0.999, whit few exceptions at 0.995) have been obtained, interpolating the adopted Split-Pseudo Voight curve with all the sampling points corresponding to the top and the flanks of the bands (Fig.9c, d and e), with the exception of the highest sampled point at the top.

For the $^{13}CO_2$ ν_1, instead, the best R^2 (mostly around 0.997 and 0.999, with few exceptions at 0.995) have been reached by interpolating the curve with all the sampling points at the top of the bands and at least the first and the last sampling points at their bases (Fig.9g).

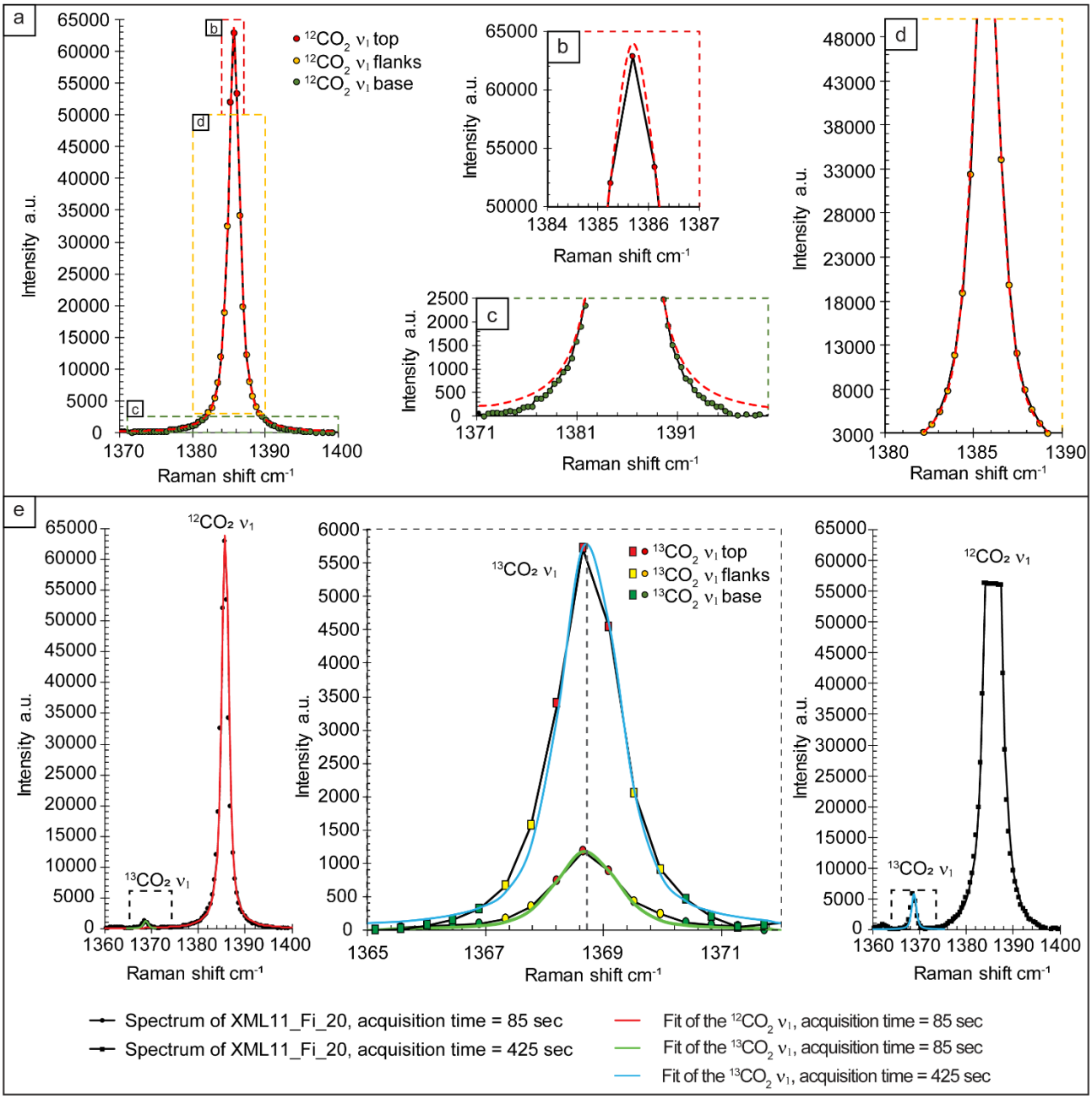

Fig.9 Figure showing an example fitting of the $^{12}CO_2$ and the $^{13}CO_2$ ν_1 isotopologues. With the adopted Raman analytical protocols, the $^{12}CO_2$ ν_1 is defined by 67 of sampling points, while the $^{13}CO_2$ ν_1 by 13 sampling points for both SS and DS sets of measurements. a) Example of fitting of the $^{12}CO_2$ ν_1 isotopologue. The enlargements on the top (b), the flanks (c) and the base (d) of the band show in detail how chosen fitting curve and the fitting procedure model these three regions of the band. g) Example of fitting of the $^{13}CO_2$ ν_1. a.u. = arbitrary units; cm^{-1} = Raman shift; ν_1 = upper band.

6.1.3 References

1. Schrötter H.W., Klöckner H.W. Raman Scattering Cross Sections in Gases and Liquids. In: *Raman Spectroscopy of Gases and Liquids*, Weber A. (eds). Topics in Current Physics, vol 11. Springer, Berlin, Heidelberg. https://doi.org/10.1007/978-3-642-81279-8_4 (1979).

2. Dhamelincourt, P., Beny, J. M., Dubessy, J., and Poty, B. Analyse d'inclusions fluides à la microsonde MOLE à effet Raman. *B. Mineral.* **102**, 600-610. (1979)

3. Bertrán, J. F. Study of the Fermi doublet ν_1—$2\nu_2$ in the Raman spectra of CO_2 in different phases. *Spectrochim. Acta A.-M.* **39**, 119-121; https://doi.org/10.1002/jrs.1250200705 (1983).

4. Dubessy, J., Poty, B., and Ramboz, C. Advances in COHNS fluid geochemistry based on micro-Raman spectrometric analysis of fluid inclusions. *Eur. J. Mineral.* **1**, 517-534; DOI: 10.1127/ejm/1/4/0517 (1989).

5. Burke, E. A. Raman microspectrometry of fluid inclusions. *Lithos*, **55**, 139-158; https://doi.org/10.1016/S0024-4937(00)00043-8 (2001).

6. Li, J., Li, R., Zhao, B., Wang, N., and Cheng, J. Quantitative analysis and measurement of carbon isotopic compositions in individual fluid inclusions by micro-laser Raman spectrometry. *Anal. Methods*. **8**, 6730-6738. https://doi.org/10.1039/C6AY01897A (2016).

7. McCreery, R. L. Raman spectroscopy for chemical analysis. *Meas.t sci. technol.* **12**(5), 653; (2001).

8. Wojdyr, M. Fityk: a general-purpose peak fitting program. *J. Appl. Crystallogr.* **43**, 1126-1128; https://doi.org/10.1107/S0021889810030499 (2010).

9. Yuan, X., and Mayanovic, R. A. An empirical study on Raman peak fitting and its application to Raman quantitative research. *Appl. Spectrosc.* **71**, 2325-2338; https://doi.org/10.1177/0003702817721527 (2017).

6.1.4 Supplementary Tables

Table S.1 Summary of the petrographic and chemical characteristics of selected 42 fluid inclusions trapped in olivine, orthopyroxene and clinopyroxene trapped in mantle peridotites from Lake Tana region (Ethiopia) and El Hierro (Canary Islands)

Locality	Sample	Host mineral	FI	Size	Depth	Density	Gas components	
							CO_2	N_2
					µm	g/cm^3	mol%	mol%
Lake Tana region	INJ34	Ol	INJ34_FI14	8	10	0.89	100	-
Lake Tana region	INJ34	Ol	INJ34_FI15	17	8	0.95	100	-
Lake Tana region	INJ34	Ol	INJ34_FI16	12	12	0.74	100	-
Lake Tana region	INJ34	Ol	INJ34_FI17	8	10	1.06	100	-
Lake Tana region	INJ34	Ol	INJ34_FI18	8	9	0.74	100	-
Lake Tana region	INJ34	Ol	INJ34_FI19	11	14	1.06	100	-
Lake Tana region	INJ34	Ol	INJ34_FI20	7	5	0.87	100	-
Lake Tana region	INJ34	Ol	INJ34_FI21	10	6	1.01	100	-
Lake Tana region	INJ34	Ol	INJ34_FI22	6	8	0.92	100	-
Lake Tana region	INJ7	Ol	INJ7_FI23	10	6	0.98	100	-
Lake Tana region	INJ7	Ol	INJ7_FI24	14	8	0.99	100	-
Lake Tana region	INJ16	Ol	INJ16_FI25	8	7	0.99	100	-
Lake Tana region	INJ38	Ol	INJ38_FI26	10	9	0.91	100	-
Lake Tana region	INJ4	Opx	INJ4_FI2	8	15	0.84	100	-
Lake Tana region	INJ16	Opx	INJ16b2_FI5	5	18	0.84	100	-
Lake Tana region	INJ16	Opx	INJ16_FI8	12	7	0.73	100	-
Lake Tana region	INJ18	Opx	INJ_18_FI7	6	7	0.98	100	-
Lake Tana region	INJ7	Opx	INJ7_FI9	7	12	1.07	100	-
Lake Tana region	INJ7	Opx	INJ7_FI10	12	11	1.07	100	-
Lake Tana region	INJ35	Opx	INJ35_FI11	15	8	1.07	100	-
El Hierro	XML3	Ol	XML3A_FI2	14	13	0.82	100	-
El Hierro	XML9	Ol	XML9A_FI16	8	12	0.93	100	-
El Hierro	XML11	Ol	XML11_FI17	21	14	0.94	100	-
El Hierro	XML11	Ol	XML11_FI23	10	9	0.91	100	-
El Hierro	XML11	Ol	XML11_FI24	12	10	0.91	100	-
El Hierro	XML11	Ol	XML11_FI22	15	10	0.84	100	-
El Hierro	XML6	Opx	XML6_FI3	7	10	1.04	100	-
El Hierro	XML6	Opx	XML6_FI4	6.5	11	1.03	100	-
El Hierro	XML6	Opx	XML6_FI5	8	13	1.05	100	-
El Hierro	XML6	Opx	XML6_FI6	10	19	1.06	100	-
El Hierro	XML6	Opx	XML6_FI7	8	16	1.05	100	-
El Hierro	XML6	Opx	XML6_FI8	7	11	1.05	100	-
El Hierro	XML7	Opx	XML7A_FI10	15	16	1.03	100	-
El Hierro	XML11	Opx	XML11_FI18	15	5	1.02	100	-
El Hierro	XML11	Opx	XML11_FI20	19	17	1.05	100	-
El Hierro	XML11	Opx	XML11_FI21	7	9	0.97	100	-
El Hierro	XML7	Cpx	XML7_FI44	10	9	0.76	100	-
El Hierro	XML7	Cpx	XML7_FI45	18	5	0.97	100	-
El Hierro	XML11	Cpx	XML11_FI46	15	10	0.97	100	-
El Hierro	XML11	Cpx	XML11_FI47	14	8	0.91	100	-
El Hierro	XML11	Cpx	XML11_FI48	15	10	1.05	100	-
El Hierro	XML11	Cpx	XML11_FI49	12	7	0.97	100	-

Ol = olivine; Opx = orthopyroxene; Cpx = clinopyroxene; FI = fluid inclusion.

Table S.2 Complete dataset reporting measured $^{12}CO_2$ ν_1 and $^{13}CO_2$ ν_1 areas and $^{13}CO2$ ν_1/$^{12}CO2$ ν_1 area ratios for 42 analysed fluid inclusions trapped in olivine, orthopyroxene and clinopyroxene in peridotites from Lake Tana region region (Ethiopia) and El Hierro (Canary Islands).

Locality	Sample	Host mineral	FI	Set of measures	Ac. Time $^{12}C_{CO2v1}$ s	$A_{12CO2v1}$ meas	Ac. Time $^{13}C_{CO2v1}$ s	$A_{13CO2v1}$ meas	$A_{13CO2v1}$ norm	$A_{13CO2v1}$/ $A_{12CO2v1}$
						132337		1475	1475	0.01115
Lake Tana region	INJ34	Ol	INJ34_FI14	SS	200	136852	200	1530	1530	0.01118
						136625		1525	1525	0.01116
						132337		7377	1475	0.01115
Lake Tana region	INJ34	Ol	INJ34_FI14	DS	200	136852	1000	7642	1528	0.01117
						136625		7613	1523	0.01114
						132182		1474	1474	0.01115
Lake Tana region	INJ34	Ol	INJ34_FI15	SS	200	142894	200	1594	1594	0.01115
						139548		1559	1559	0.01117
						132182		7379	1476	0.01116
Lake Tana region	INJ34	Ol	INJ34_FI15	DS	200	142894	1000	7988	1598	0.01118
						139548		7801	1560	0.01118
						156677		1749	1749	0.01116
Lake Tana region	INJ34	Ol	INJ34_FI16	SS	120	170160	120	1899	1899	0.01116
						167696		1871	1871	0.01115
						156677		10195	2039	0.01301
Lake Tana region	INJ34	Ol	INJ34_FI16	DS	120	170160	600	9494	1899	0.01116
						167696		9362	1872	0.01116
						142595		1592	1592	0.01117
Lake Tana region	INJ34	Ol	INJ34_FI17	SS	120	135828	120	1514	1514	0.01115
						152971		1705	1705	0.01115
						142595		7961	1592	0.01117
Lake Tana region	INJ34	Ol	INJ34_FI17	DS	120	135828	600	7585	1517	0.01117
						152971		8541	1708	0.01117
						149134		1663	1663	0.01115
Lake Tana region	INJ34	Ol	INJ34_FI18	SS	120	143608	120	1601	1601	0.01115
						146753		1639	1639	0.01117
						149134		8307	1661	0.01114
Lake Tana region	INJ34	Ol	INJ34_FI18	DS	120	143608	600	8013	1603	0.01116
						146753		8188	1638	0.01116
						154318		1722	1722	0.01116
Lake Tana region	INJ34	Ol	INJ34_FI19	SS	90	147640	90	1649	1649	0.01117
						144890		1619	1619	0.01117
						154318		7578	1516	0.00982
Lake Tana region	INJ34	Ol	INJ34_FI19	DS	90	147640	450	8244	1649	0.01117
						144890		8074	1615	0.01114
						159748		1518	1518	0.00950
Lake Tana region	INJ34	Ol	INJ34_FI20	SS	120	144695	120	1507	1507	0.01042
						142387		1588	1588	0.01116
						159748		8904	1781	0.01115
Lake Tana region	INJ34	Ol	INJ34_FI20	DS	120	144695	600	8069	1614	0.01115
						142387		7941	1588	0.01115
						151868		1697	1697	0.01118
Lake Tana region	INJ34	Ol	INJ34_FI21	SS	190	148511	190	1658	1658	0.01116
						122826		1371	1371	0.01117
						151868		8474	1695	0.01116
Lake Tana region	INJ34	Ol	INJ34_FI21	DS	190	148511	950	7785	1557	0.01048
						122826		6219	1244	0.01013
						163389		1824	1824	0.01116
Lake Tana region	INJ34	Ol	INJ34_FI22	SS	65	172803	65	1929	1929	0.01116
						181653		2029	2029	0.01117
						163389		9129	1826	0.01117
Lake Tana region	INJ34	Ol	INJ34_FI22	DS	65	172803	325	9646	1929	0.01116
						181653		10135	2027	0.01116
						152751		1705	1705	0.01116
Lake Tana region	INJ7	Ol	INJ7_FI23	SS	100	156122	100	1739	1739	0.01114
						153346		1714	1714	0.01118
						152751		8529	1706	0.01117
Lake Tana region	INJ7	Ol	INJ7_FI23	DS	100	156122	500	8706	1741	0.01115
						153346		8569	1714	0.01118

						158205		8818	1764	0.01115
Lake Tana region	INJ7	Ol	INJ7_FI24	DS	140	162838	700	8695	1739	0.01068
						175798		7752	1550	0.00882
						141787		1585	1585	0.01118
Lake Tana region	INJ16	Ol	INJ16_FI25	SS	60	132105	60	1475	1475	0.01116
						129121		1441	1441	0.01116
						141787		7919	1584	0.01117
Lake Tana region	INJ16	Ol	INJ16_FI25	DS	60	132105	300	7365	1473	0.01115
						129121		7199	1440	0.01115
						154716		1608	1608	0.01040
Lake Tana region	INJ38	Ol	INJ38_FI26	SS	70	151164	70	1688	1688	0.01116
						159076		1566	1566	0.00985
						154716		8625	1725	0.01115
Lake Tana region	INJ38	Ol	INJ38_FI26	DS	70	151164	350	8436	1687	0.01116
						159076		8870	1774	0.01115
						159137		1775	1775	0.01115
Lake Tana region	INJ4	Opx	INJ4_FI2	SS	60	164707	60	1837	1837	0.01115
						161026		1797	1797	0.01116
						159137		8868	1774	0.01115
Lake Tana region	INJ4	Opx	INJ4_FI2	DS	60	164707	300	9189	1838	0.01116
						161026		8989	1798	0.01116
						144390		1611	1611	0.01116
Lake Tana region	INJ16	Opx	INJ16b2_FI5	SS	40	147449	40	1642	1642	0.01114
						152190		1696	1696	0.01114
						144390		8054	1611	0.01116
Lake Tana region	INJ16	Opx	INJ16b2_FI5	DS	40	147449	200	8206	1641	0.01113
						152190		8358	1672	0.01098
						128053		1429	1429	0.01116
Lake Tana region	INJ16	Opx	INJ16_FI8	SS	100	134101	100	1498	1498	0.01117
						140657		1570	1570	0.01116
						128053		7149	1430	0.01117
Lake Tana region	INJ16	Opx	INJ16_FI8	DS	100	134101	550	7486	1497	0.01116
						140657		7849	1570	0.01116
						152587		1704	1704	0.01116
Lake Tana region	INJ18	Opx	INJ_18_FI7	SS	90	161095	90	1795	1795	0.01114
						164850		1833	1833	0.01112
						152587		9541	1704	0.01117
Lake Tana region	INJ18	Opx	INJ_18_FI7	DS	90	161095	500	10058	1796	0.01115
						164850		10287	1837	0.01114
						151008		1684	1684	0.01115
Lake Tana region	INJ7	Opx	INJ7_FI9	SS	35	158133	35	1764	1764	0.01115
						159229		1778	1778	0.01117
						151008		8420	1684	0.01115
Lake Tana region	INJ7	Opx	INJ7_FI9	DS	35	158133	175	8814	1763	0.01115
						159229		8878	1776	0.01115
						157949		1762	1762	0.01115
Lake Tana region	INJ7	Opx	INJ7_FI10	SS	45	156851	45	1749	1749	0.01115
						151772		1694	1694	0.01116
						157949		8818	1764	0.01117
Lake Tana region	INJ7	Opx	INJ7_FI10	DS	45	156851	225	8749	1750	0.01116
						151772		8484	1697	0.01118
						141479		1580	1580	0.01117
Lake Tana region	INJ35	Opx	INJ35_FI11	SS	180	148380	180	1656	1656	0.01116
						141203		1574	1574	0.01115
						141479		7895	1579	0.01116
Lake Tana region	INJ35	Opx	INJ35_FI11	DS	180	148380	900	8277	1655	0.01116
						141203		7877	1575	0.01116
						151149		1696	1696	0.01122
El Hierro	XML3	Ol	XML3A_FI2	SS	120	148770	120	1671	1671	0.01123
						148758		1672	1672	0.01124
						151149		8494	1699	0.01124
El Hierro	XML3	Ol	XML3A_FI2	DS	120	148770	600	8363	1673	0.01124
						148299		8327	1665	0.01123
						169443		1817	1817	0.01072
El Hierro	XML9	Ol	XML9A_FI16	SS	50	171523	50	1815	1815	0.01058
						168596		1669	1669	0.00990
						169443		7636	1909	0.01127
El Hierro	XML9	Ol	XML9A_FI16	DS	50	171523	200	7750	1938	0.01130
						168596		7608	1902	0.01128
						159998		1815	1815	0.01135
El Hierro	XML11	Ol	XML11_FI17	SS	360	144044	360	1436	1436	0.00997
						130946		1399	1399	0.01069
						159998		7163	1791	0.01119
El Hierro	XML11	Ol	XML11_FI17	DS	360	144044	1440	6470	1617	0.01123
						130946		5753	1438	0.01098

						136308		1534	1534	0.01125
El Hierro	XML11	Ol	XML11_FI23	SS	60	144374	60	1588	1588	0.01100
						140158		1568	1568	0.01119
						136308		9202	1534	0.01125
El Hierro	XML11	Ol	XML11_FI23	DS	60	144374	360	9752	1625	0.01126
						140158		9027	1504	0.01073
						146610		1624	1624	0.01108
El Hierro	XML11	Ol	XML11_FI24	SS	90	139126	90	1542	1542	0.01108
						136791		1612	1612	0.01178
						146610		9959	1660	0.01132
El Hierro	XML11	Ol	XML11_FI24	DS	90	139126	540	9382	1564	0.01124
						136791		9286	1548	0.01131
						96775		1088	1088	0.01124
El Hierro	XML11	Ol	XML11_FI22	SS	240	96520	240	1087	1087	0.01126
						93540		1051	1051	0.01124
						96775		5432	1086	0.01123
El Hierro	XML11	Ol	XML11_FI22	DS	240	96520	1200	5432	1086	0.01126
						93540		5210	1042	0.01114
						172241		1938	1938	0.01125
El Hierro	XML6	Opx	XML6_FI3	SS	60	172346	60	1939	1939	0.01125
						171159		1927	1927	0.01126
						172241		10676	2135	0.01240
El Hierro	XML6	Opx	XML6_FI3	DS	60	172346	300	9327	1865	0.01082
						171159		9624	1925	0.01125
						172229		1940	1940	0.01126
El Hierro	XML6	Opx	XML6_FI4	SS	60	174704	60	1909	1909	0.01093
						176960		1992	1992	0.01126
						172229		9681	1936	0.01124
El Hierro	XML6	Opx	XML6_FI4	DS	60	174704	300	9822	1964	0.01124
						176960		9952	1990	0.01125
						175103		1969	1969	0.01125
El Hierro	XML6	Opx	XML6_FI5	SS	80	178105	80	1998	1998	0.01122
						177662		1993	1993	0.01122
						175103		9829	1966	0.01123
El Hierro	XML6	Opx	XML6_FI5	DS	80	178105	400	9979	1996	0.01121
						177662		9975	1995	0.01123
						174532		1958	1958	0.01122
El Hierro	XML6	Opx	XML6_FI6	SS	55	170493	55	1915	1915	0.01123
						168384		1891	1891	0.01123
						174532		9794	1959	0.01122
El Hierro	XML6	Opx	XML6_FI6	DS	55	170493	275	9570	1914	0.01123
						168384		9209	1842	0.01094
						171025		1916	1916	0.01120
El Hierro	XML6	Opx	XML6_FI7	SS	53	172261	53	1933	1933	0.01122
						167967		1885	1885	0.01122
						171025		9636	1927	0.01127
El Hierro	XML6	Opx	XML6_FI7	DS	53	172261	265	9601	1920	0.01115
						167967		9410	1882	0.01120
						165101		1854	1854	0.01123
El Hierro	XML6	Opx	XML6_FI8	SS	60	156275	60	1756	1756	0.01124
						141405		1592	1592	0.01126
						165101		9040	1808	0.01095
El Hierro	XML6	Opx	XML6_FI8	DS	60	156275	300	8520	1704	0.01090
						141405		7942	1588	0.01123
						139805		1572	1572	0.01124
El Hierro	XML7	Opx	XML7A_FI10	SS	70	129917	70	1459	1459	0.01123
						120769		1362	1362	0.01128
						139805		7829	1566	0.01120
El Hierro	XML7	Opx	XML7A_FI10	DS	70	129917	350	6977	1395	0.01074
						120769		6763	1353	0.01120
						153188		1749	1749	0.01142
El Hierro	XML11	Opx	XML11_FI18	SS	180	152639	180	1720	1720	0.01127
						149462		1703	1703	0.01140
						153188		5145	1715	0.01120
El Hierro	XML11	Opx	XML11_FI18	DS	180	152639	540	4829	1610	0.01055
						149462		5041	1680	0.01124
						168902		1899	1899	0.01124
El Hierro	XML11	Opx	XML11_FI20	SS	85	174710	85	1959	1959	0.01121
						174982		1965	1965	0.01123
						168902		9495	1899	0.01124
El Hierro	XML11	Opx	XML11_FI20	DS	85	174710	425	9786	1957	0.01120
						174982		9209	1842	0.01053
						165049		1855	1855	0.01124
El Hierro	XML11	Opx	XML11_FI21	SS	65	152056	65	1706	1706	0.01122
						138526		1557	1557	0.01124

						165049		9266	1853	0.01123
El Hierro	XML11	Opx	XML11_FI21	DS	65	152056	325	8206	1641	0.01079
						138526		7440	1488	0.01074
						140807		1578	1578	0.01121
El Hierro	XML7	Cpx	XML7_FI44	SS	90	134272	90	1506	1506	0.01122
						134935		1514	1514	0.01122
						140807		7897	1579	0.01122
El Hierro	XML7	Cpx	XML7_FI44	DS	90	134272	450	7525	1505	0.01121
						134935		7571	1514	0.01122
						132665		1487	1487	0.01121
El Hierro	XML7	Cpx	XML7_FI45	SS	160	150949	160	1693	1693	0.01122
						145166		1629	1629	0.01122
						132665		7445	1489	0.01122
El Hierro	XML7	Cpx	XML7_FI45	DS	160	150949	800	8471	1694	0.01122
						145166		8143	1629	0.01122
						141407		1586	1586	0.01122
El Hierro	XML11	Cpx	XML11_FI46	SS	100	157930	100	1769	1769	0.01120
						152559		1712	1712	0.01123
						141407		7922	1584	0.01120
El Hierro	XML11	Cpx	XML11_FI46	DS	100	157930	500	8481	1696	0.01074
						152559		8364	1673	0.01096
						140978		1581	1581	0.01122
El Hierro	XML11	Cpx	XML11_FI47	SS	100	132626	100	1487	1487	0.01121
						132355		1485	1485	0.01122
						140978		7899	1580	0.01121
El Hierro	XML11	Cpx	XML11_FI47	DS	100	132626	500	7436	1487	0.01121
						132355		7422	1484	0.01122
						160019		1794	1794	0.01121
El Hierro	XML11	Cpx	XML11_FI48	SS	100	146762	100	1645	1645	0.01121
						121375		1362	1362	0.01122
						160019		8196	1639	0.01024
El Hierro	XML11	Cpx	XML11_FI48	DS	100	146762	500	8233	1647	0.01122
						121375		6807	1361	0.01122
						141653		1589	1589	0.01122
El Hierro	XML11	Cpx	XML11_FI49	SS	90	143550	90	1610	1610	0.01121
						139312		1562	1562	0.01121
						141653		7944	1589	0.01122
El Hierro	XML11	Cpx	XML11_FI49	DS	90	143550	450	8049	1610	0.01121
						139312		7810	1562	0.01121

For each of the 42 fluid inclusions two sets of measurements composed by three spectra each have been acquired (84 sets of measurements, 252 spectra). In red sets of spectra not considered for further calculations. Ol = olivine; Opx = orthopyroxene; Cpx = clinopyroxene; FI = fluid inclusion; Ac. time $^{12}C_{CO2v1}$ = acquisition times adopted for the $^{12}CO_2$ upper band; $A_{12CO2v1}$ = $^{12}CO_2$ upper band area; Ac. time $^{13}C_{CO2v1}$ = acquisition times adopted for the $^{13}CO_2$ upper band; $A_{13CO2v1}$ = $^{13}CO_2$ upper band area; $A_{13CO2v1}/A_{12CO2v1}$ = $^{13}CO_2/^{12}CO_2$ upper bands area ratios; meas = measured; norm = normalised; SS = single spectra; DS = distinct spectra.

Table S.3 Calculated $^{13}CO_2$ ν_1/$^{12}CO_2$ ν_1 area ratios and $^{13}CO_2$ ν_1/$^{12}CO_2$ ν_1 statistical treatment for the evaluation of area ratios' reproducibility.

							$A_{13CO2v1}/A_{12CO2v1}$			
Locality	**Sample**	**Host mineral**	**FI**	**Set of measures**	**Ac. times $^{13}C_{CO2v1}$ s**	**$A_{13CO2v1}/A_{12CO2v1}$**	**Ave.**	**1σ**	***Variance‰***	***Reproducibility‰***
									‰	‰
Lake Tana region	INJ34	Ol	INJ34_FI14	SS	200	0.01115 0.01118 0.01116	0.011162	0.000014	3.07	1.27
Lake Tana region	INJ34	Ol	INJ34_FI14	DS	1000	0.01115 0.01117 0.01114	0.011154	0.000010	2.15	0.93
Lake Tana region	INJ34	Ol	INJ34_FI15	SS	200	0.01115 0.01115 0.01117	0.011157	0.000009	1.82	0.80
Lake Tana region	INJ34	Ol	INJ34_FI15	DS	1000	0.01116 0.01118 0.01118	0.011175	0.000007	1.40	0.66
Lake Tana region	INJ34	Ol	INJ34_FI16	SS	120	0.01116 0.01116 0.01115	0.011159	0.000003	0.68	0.28
Lake Tana region	INJ34	Ol	INJ34_FI17	SS	120	0.01117 0.01115 0.01115	0.011154	0.000008	1.64	0.75
Lake Tana region	INJ34	Ol	INJ34_FI17	DS	600	0.01117 0.01117 0.01117	0.011167	0.000001	0.28	0.12
Lake Tana region	INJ34	Ol	INJ34_FI18	SS	120	0.01115 0.01115 0.01117	0.011156	0.000009	1.74	0.77
Lake Tana region	INJ34	Ol	INJ34_FI18	DS	600	0.01114 0.01116 0.01116	0.011153	0.000009	1.67	0.77
Lake Tana region	INJ34	Ol	INJ34_FI19	SS	90	0.01116 0.01117 0.01117	0.011167	0.000006	1.35	0.55
Lake Tana region	INJ34	Ol	INJ34_FI20	DS	600	0.01115 0.01115 0.01115	0.011152	0.000003	0.56	0.25
Lake Tana region	INJ34	Ol	INJ34_FI21	SS	190	0.01118 0.01116 0.01117	0.011168	0.000006	1.23	0.53
Lake Tana region	INJ34	Ol	INJ34_FI22	SS	65	0.01116 0.01116 0.01117	0.011164	0.000003	0.68	0.29
Lake Tana region	INJ34	Ol	INJ34_FI22	DS	325	0.01117 0.01116 0.01116	0.011166	0.000006	1.40	0.58
Lake Tana region	INJ7	Ol	INJ7_FI23	SS	100	0.01116 0.01114 0.01118	0.011161	0.000014	3.08	1.28
Lake Tana region	INJ7	Ol	INJ7_FI23	DS	500	0.01117 0.01115 0.01118	0.011165	0.000009	2.02	0.83
Lake Tana region	INJ7	Ol	INJ7_FI24	SS	140	0.01115 0.01115 0.01116	0.011155	0.000005	1.06	0.46
Lake Tana region	INJ16	Ol	INJ16_FI25	SS	60	0.01118 0.01116 0.01116	0.011167	0.000008	1.56	0.68
Lake Tana region	INJ16	Ol	INJ16_FI25	DS	300	0.01117 0.01115 0.01115	0.011158	0.000009	1.75	0.81
Lake Tana region	INJ38	Ol	INJ38_FI26	DS	350	0.01115 0.01116 0.01115	0.011154	0.000005	1.07	0.45

Lake Tana region	INJ4	Opx	INJ4_FI2	SS	60	0.01115 0.01115 0.01116	0.011157	0.000004	0.71	0.32
Lake Tana region	INJ4	Opx	INJ4_FI2	DS	300	0.01115 0.01116 0.01116	0.011156	0.000008	1.75	0.73
Lake Tana region	INJ16	Opx	INJ16b2_FI5	SS	40	0.01116 0.01114 0.01114	0.011146	0.000009	1.85	0.81
Lake Tana region	INJ16	Opx	INJ16_FI8	SS	100	0.01116 0.01117 0.01116	0.011164	0.000007	1.36	0.58
Lake Tana region	INJ16	Opx	INJ16_FI8	DS	550	0.01117 0.01116 0.01116	0.011164	0.000002	0.46	0.19
Lake Tana region	INJ18	Opx	INJ_18_FI7	SS	90	0.01116 0.01114 0.01112	0.011141	0.000019	4.12	1.68
Lake Tana region	INJ18	Opx	INJ_18_FI7	DS	500	0.01117 0.01115 0.01114	0.011153	0.000009	1.98	0.85
Lake Tana region	INJ7	Opx	INJ7_FI9	SS	35	0.01115 0.01115 0.01117	0.011157	0.000007	1.33	0.60
Lake Tana region	INJ7	Opx	INJ7_FI9	DS	175	0.01115 0.01115 0.01115	0.011150	0.000002	0.37	0.17
Lake Tana region	INJ7	Opx	INJ7_FI10	SS	45	0.01115 0.01115 0.01116	0.011156	0.000006	1.17	0.50
Lake Tana region	INJ7	Opx	INJ7_FI10	DS	225	0.01117 0.01116 0.01118	0.011167	0.000010	2.19	0.90
Lake Tana region	INJ35	Opx	INJ35_FI11	SS	180	0.01117 0.01116 0.01115	0.011158	0.000007	1.53	0.63
Lake Tana region	INJ35	Opx	INJ35_FI11	DS	900	0.01116 0.01116 0.01116	0.011158	0.000002	0.35	0.15
El Hierro	XML3	Ol	XML3A_FI2	SS	120	0.01122 0.01123 0.01124	0.011230	0.000009	2.00	0.83
El Hierro	XML3	Ol	XML3A_FI2	DS	600	0.01124 0.01124 0.01123	0.011237	0.000005	1.05	0.44
El Hierro	XML9	Ol	XML9A_FI1(	DS	200	0.01127 0.01130 0.01128	0.011281	0.000012	2.64	1.08
El Hierro	XML11	Ol	XML11_FI24	DS	540	0.01132 0.01124 0.01131	0.011292	0.000037	7.26	3.29
El Hierro	XML11	Ol	XML11_FI22	SS	240	0.01124 0.01126 0.01124	0.011246	0.000008	1.73	0.73
El Hierro	XML11	Ol	XML11_FI22	DS	1200	0.01123 0.01126 0.01114	0.011207	0.000049	10.32	4.39
El Hierro	XML6	Opx	XML6_FI3	SS	60	0.01125 0.01125 0.01126	0.011253	0.000002	0.40	0.16
El Hierro	XML6	Opx	XML6_FI4	DS	300	0.01124 0.01124 0.01125	0.011245	0.000003	0.54	0.22
El Hierro	XML6	Opx	XML6_FI5	SS	80	0.01125 0.01122 0.01122	0.011227	0.000013	2.70	1.18
El Hierro	XML6	Opx	XML6_FI5	DS	400	0.01123 0.01121 0.01123	0.011220	0.000010	2.08	0.92
El Hierro	XML6	Opx	XML6_FI6	SS	55	0.01122 0.01123 0.01123	0.011226	0.000007	1.33	0.60

El Hierro	XML6	Opx	XML6_FI7	SS	53	0.01120 0.01122 0.01122	0.011216	0.000009	1.80	0.76
El Hierro	XML6	Opx	XML6_FI7	DS	265	0.01127 0.01115 0.01120	0.011206	0.000050	10.88	4.44
El Hierro	XML6	Opx	XML6_FI8	SS	60	0.01123 0.01124 0.01126	0.011242	0.000014	3.07	1.28
El Hierro	XML7	Opx	XML7A_FI10	SS	70	0.01124 0.01123 0.01128	0.011249	0.000020	4.12	1.77
El Hierro	XML11	Opx	XML11_FI18	SS	180	0.01142 0.01127 0.01140	0.011361	0.000067	13.42	5.93
El Hierro	XML11	Opx	XML11_FI20	SS	85	0.01124 0.01121 0.01123	0.011229	0.000013	2.73	1.13
El Hierro	XML11	Opx	XML11_FI21	SS	65	0.01124 0.01122 0.01124	0.011233	0.000011	2.24	0.99
El Hierro	XML7	Cpx	XML7_FI44	SS	90	0.01121 0.01122 0.01122	0.0112138	0.000006	1.29	0.54
El Hierro	XML7	Cpx	XML7_FI44	DS	450	0.01122 0.01121 0.01122	0.0112157	0.000006	1.23	0.50
El Hierro	XML7	Cpx	XML7_FI45	SS	160	0.01121 0.01122 0.01122	0.0112162	0.000006	1.35	0.55
El Hierro	XML7	Cpx	XML7_FI45	DS	800	0.01122 0.01122 0.01122	0.0112221	0.000003	0.51	0.25
El Hierro	XML11	Cpx	XML11_FI46	SS	100	0.01122 0.01120 0.01123	0.0112160	0.000009	1.91	0.81
El Hierro	XML11	Cpx	XML11_FI47	SS	100	0.01122 0.01121 0.01122	0.0112154	0.000002	0.52	0.22
El Hierro	XML11	Cpx	XML11_FI47	DS	500	0.01121 0.01121 0.01122	0.0112116	0.000004	0.89	0.38
El Hierro	XML11	Cpx	XML11_FI48	SS	100	0.01121 0.01121 0.01122	0.0112134	0.000006	1.30	0.53
El Hierro	XML11	Cpx	XML11_FI49	SS	90	0.01122 0.01121 0.01121	0.0112153	0.000002	0.36	0.15
El Hierro	XML11	Cpx	XML11_FI49	DS	450	0.01122 0.01121 0.01121	0.0112144	0.000001	0.29	0.12

Total number of sets of measures remaining: SS = 35, 105 spectra; DS = 26, 78 spectra. Ol = olivine; Opx = orthopyroxene; Cpx = clinopyroxene; FI = fluid inclusion; Ac. time $^{13}C_{CO2v1}$ = acquisition times adopted for the $^{13}CO_2$ upper band; $A_{13CO2v1}/A_{12CO2v1}$ = $^{13}CO_2/^{12}CO_2$ upper bands area ratios; Ave. = average; SS = single spectra; DS = distinct spectra.

Table S.4 Complete dataset reporting calculated $^{13}CO_2$ ν_1/$^{12}CO_2$ ν_1 area ratios and $\delta^{13}C_{CO2}$‰ values.

Locality	Sample	Host mineral	FI	Set of measures	$A_{13CO2\nu1}/A_{12CO2\nu1}$	Ave	$\delta^{13}C_{CO2}$	Ave	Error	1σ
							‰	‰	‰	‰
					0.01115		-8.11			
Lake Tana region	INJ34	Ol	INJ34_FI14	SS	0.01118	0.011162	-5.06	-6.71	1.52	1.26
					0.01116		-6.97			
					0.01115		-7.84			
Lake Tana region	INJ34	Ol	INJ34_FI14	DS	0.01117	0.011154	-6.13	-7.41	1.07	0.92
					0.01114		-8.26			
					0.01115		-7.85			
Lake Tana region	INJ34	Ol	INJ34_FI15	SS	0.01115	0.011157	-7.58	-7.16	0.90	0.80
					0.01117		-6.04			
					0.01116		-6.45			
Lake Tana region	INJ34	Ol	INJ34_FI15	DS	0.01118	0.011175	-5.06	-5.53	0.69	0.65
					0.01118		-5.07			
					0.01116		-6.69			
Lake Tana region	INJ34	Ol	INJ34_FI16	SS	0.01116	0.011159	-6.89	-6.98	0.34	0.28
					0.01115		-7.36			
					0.01117		-6.31			
Lake Tana region	INJ34	Ol	INJ34_FI17	SS	0.01115	0.011154	-7.83	-7.36	0.81	0.74
					0.01115		-7.94			
					0.01117		-6.33			
Lake Tana region	INJ34	Ol	INJ34_FI17	DS	0.01117	0.011167	-6.05	-6.22	0.14	0.12
					0.01117		-6.29			
					0.01115		-7.89			
Lake Tana region	INJ34	Ol	INJ34_FI18	SS	0.01115	0.011156	-7.64	-7.23	0.86	0.76
					0.01117		-6.17			
					0.01114		-8.57			
Lake Tana region	INJ34	Ol	INJ34_FI18	DS	0.01116	0.011153	-6.92	-7.50	0.83	0.76
					0.01116		-7.00			
					0.01116		-6.90			
Lake Tana region	INJ34	Ol	INJ34_FI19	SS	0.01117	0.011167	-6.17	-6.21	0.67	0.55
					0.01117		-5.56			
					0.01115		-7.95			
Lake Tana region	INJ34	Ol	INJ34_FI20	DS	0.01115	0.011152	-7.47	-7.60	0.28	0.24
					0.01115		-7.40			
					0.01118		-5.45			
Lake Tana region	INJ34	Ol	INJ34_FI21	SS	0.01116	0.011168	-6.67	-6.18	0.61	0.53
					0.01117		-6.41			
					0.01116		-6.83			
Lake Tana region	INJ34	Ol	INJ34_FI22	SS	0.01116	0.011164	-6.68	-6.55	0.34	0.29
					0.01117		-6.15			
					0.01117		-5.61			
Lake Tana region	INJ34	Ol	INJ34_FI22	DS	0.01116	0.011166	-6.53	-6.38	0.69	0.58
					0.01116		-7.00			
					0.01116		-6.47			
Lake Tana region	INJ7	Ol	INJ7_FI23	SS	0.01114	0.011161	-8.52	-6.82	1.53	1.27
					0.01118		-5.45			
					0.01117		-6.28			
Lake Tana region	INJ7	Ol	INJ7_FI23	DS	0.01115	0.011165	-7.50	-6.42	1.01	0.83
					0.01118		-5.49			

					0.01115		-7.51				
Lake Tana region	INJ7	Ol	INJ7_FI24	SS	0.01115	0.011155	-7.71	-7.29	0.53	0.46
					0.01116		-6.66				
					0.01118		-5.27				
Lake Tana region	INJ16	Ol	INJ16_FI25	SS	0.01116	0.011167	-6.57	-6.22	0.78	0.68
					0.01116		-6.82				
					0.01117		-5.95				
Lake Tana region	INJ16	Ol	INJ16_FI25	DS	0.01115	0.011158	-7.69	-7.09	0.87	0.81
					0.01115		-7.64				
					0.01115		-7.83				
Lake Tana region	INJ38	Ol	INJ38_FI26	DS	0.01116	0.011154	-6.77	-7.38	0.53	0.45
					0.01115		-7.54				
					0.01115		-7.41				
Lake Tana region	INJ4	Opx	INJ4_FI2	SS	0.01115	0.011157	-7.35	-7.15	0.35	0.32
					0.01116		-6.70				
					0.01115		-8.17				
Lake Tana region	INJ4	Opx	INJ4_FI2	DS	0.01116	0.011156	-7.06	-7.22	0.87	0.72
					0.01116		-6.43				
					0.01116		-7.03				
Lake Tana region	INJ16	Opx	INJ16b2_FI5	SS	0.01114	0.011146	-8.86	-8.16	0.92	0.80
					0.01114		-8.57				
					0.01116		-7.07				
Lake Tana region	INJ16	Opx	INJ16_FI8	SS	0.01117	0.011164	-5.72	-6.52	0.68	0.58
					0.01116		-6.76				
					0.01117		-6.32				
Lake Tana region	INJ16	Opx	INJ16_FI8	DS	0.01116	0.011164	-6.51	-6.53	0.23	0.19
					0.01116		-6.77				
					0.01116		-6.50				
Lake Tana region	INJ18	Opx	INJ_18_FI7	SS	0.01114	0.011141	-8.69	-8.59	2.04	1.67
					0.01112		-10.59				
					0.01117		-6.37				
Lake Tana region	INJ18	Opx	INJ_18_FI7	DS	0.01115	0.011153	-7.88	-7.53	0.98	0.84
					0.01114		-8.34				
					0.01115		-7.65				
Lake Tana region	INJ7	Opx	INJ7_FI9	SS	0.01115	0.011157	-7.54	-7.17	0.66	0.60
					0.01117		-6.33				
					0.01115		-7.63				
Lake Tana region	INJ7	Opx	INJ7_FI9	DS	0.01115	0.011150	-7.97	-7.74	0.18	0.17
					0.01115		-7.60				
					0.01115		-7.43				
Lake Tana region	INJ7	Opx	INJ7_FI10	SS	0.01115	0.011156	-7.72	-7.24	0.58	0.49
					0.01116		-6.56				
					0.01117		-6.35				
Lake Tana region	INJ7	Opx	INJ7_FI10	DS	0.01116	0.011167	-7.24	-6.22	1.09	0.89
					0.01118		-5.06				
					0.01117		-6.38				
Lake Tana region	INJ35	Opx	INJ35_FI11	SS	0.01116	0.011158	-6.95	-7.08	0.76	0.63
					0.01115		-7.91				
					0.01116		-6.86				
Lake Tana region	INJ35	Opx	INJ35_FI11	DS	0.01116	0.011158	-7.20	-7.06	0.17	0.15
					0.01116		-7.13				
					0.01122		-1.73				
El Hierro	XML3	Ol	XML3A_FI2	SS	0.01123	0.011230	-0.36	-0.61	1.00	0.83
					0.01124		0.27				
					0.01124		0.17				
El Hierro	XML3	Ol	XML3A_FI2	DS	0.01124	0.011237	0.45	0.01	0.52	0.44
					0.01123		-0.59				
					0.01127		2.59				
El Hierro	XML9	Ol	XML9A_FI16	DS	0.01130	0.011281	5.24	3.91	1.33	1.08
					0.01128		3.91				

					0.01120		-2.93				
El Hierro	XML6	Opx	XML6_FI7	SS	0.01122	0.011216	-1.61	-1.89	0.90	0.76
					0.01122		-1.14				
					0.01127		2.78				
El Hierro	XML6	Opx	XML6_FI7	DS	0.01115	0.011206	-8.07	-2.74	5.42	4.43
					0.01120		-2.94				
					0.01123		-0.89				
El Hierro	XML6	Opx	XML6_FI8	SS	0.01124	0.011242	0.08	0.46	1.54	1.28
					0.01126		2.19				
					0.01124		0.33				
El Hierro	XML7	Opx	XML7A_FI10	SS	0.01123	0.011249	-0.59	1.09	2.06	1.77
					0.01128		3.53				
					0.01142		16.17				
El Hierro	XML11	Opx	XML11_FI18	SS	0.01127	0.011361	2.60	11.01	6.78	5.99
					0.01140		14.25				
					0.01124		0.54				
El Hierro	XML11	Opx	XML11_FI20	SS	0.01121	0.011229	-2.19	-0.71	1.37	1.13
					0.01123		-0.47				
					0.01124		0.21				
El Hierro	XML11	Opx	XML11_FI21	SS	0.01122	0.011233	-1.73	-0.34	1.12	0.99
					0.01124		0.51				
					0.01121		-2.82				
El Hierro	XML7	Cpx	XML7_FI44	SS	0.01122	0.0112138	-1.89	-2.08	0.64	0.54
					0.01122		-1.53				
					0.01122		-1.84				
El Hierro	XML7	Cpx	XML7_FI44	DS	0.01121	0.0112157	-2.56	-1.91	0.61	0.50
					0.01122		-1.34				
					0.01121		-2.56				
El Hierro	XML7	Cpx	XML7_FI45	SS	0.01122	0.0112162	-1.84	-1.87	0.68	0.55
					0.01122		-1.21				
					0.01122		-1.18				
El Hierro	XML7	Cpx	XML7_FI45	DS	0.01122	0.0112221	-1.16	-1.34	0.27	0.25
					0.01122		-1.69				
					0.01122		-1.59				
El Hierro	XML11	Cpx	XML11_FI46	SS	0.01120	0.0112160	-2.99	-1.89	0.96	0.81
					0.01123		-1.08				
					0.01122		-1.71				
El Hierro	XML11	Cpx	XML11_FI47	SS	0.01121	0.0112154	-2.23	-1.94	0.26	0.22
					0.01122		-1.88				
					0.01121		-2.80				
El Hierro	XML11	Cpx	XML11_FI47	DS	0.01121	0.0112116	-2.11	-2.28	0.44	0.38
					0.01122		-1.92				
					0.01121		-2.23				
El Hierro	XML11	Cpx	XML11_FI48	SS	0.01121	0.0112134	-2.71	-2.12	0.65	0.53
					0.01122		-1.42				
					0.01122		-1.74				
El Hierro	XML11	Cpx	XML11_FI49	SS	0.01121	0.0112153	-2.01	-1.95	0.18	0.15
					0.01121		-2.10				
					0.01122		-1.89				
El Hierro	XML11	Cpx	XML11_FI49	DS	0.01121	0.0112144	-2.01	-2.02	0.14	0.12
					0.01121		-2.17				

$\delta^{13}C_{CO2}$‰ values have been calculated for the remaining 35 SS and the 26 DS sets of measures. For fluid inclusions where both SS and DS sets of measurements are present, the calculated $\delta^{13}C_{CO2}$‰ values having the worst accuracy (in red) have not being considered as representative for the fluid

inclusions isotopic composition. Ol = olivine; Opx = orthopyroxene; Cpx = clinopyroxene; FI = fluid inclusion; $A_{13CO2v1}/A1_{3CO2v1}$ = $^{13}CO_2/^{12}CO_2$ upper bands area ratios; Ave = Average.

7. INTER-LABORATORY APPLICATION OF RAMAN CO_2 DENSIMETER EQUATIONS: EXPERIMENTAL PROCEDURE AND STATISTICAL ANALYSIS USING BOOTSTRAPPED CONFIDENCE INTERVALS (*MANISCRIPT 2*)

S. Remigi [a,*], T. Mancini [b], S. Ferrando [c], M.-L. Frezzotti [a,*]

[a] *Dipartimento di Scienze dell'Ambiente e della Terra, Università Milano - Bicocca, Piazza della Scienza 4, 20126, Milano, Italia. E-mail: s.remigi@campus.unimib.it; maria.frezzotti@unimib.it*

[b] *Department of Economic, Social and Political Science, University of Southampton, University Road, SO17 1BJ, Southampton, United Kingdom. E-mail: T.Mancini@soton.ac.uk*

[c] *Dipartimento di Scienze della Terra, Università di Torino, Via Valperga Caluso, 35, 10125, Torino, Italia. E-mail: simona.ferrando@unito.it*

** Corresponding authors. Dipartimento di Scienze dell'Ambiente e della Terra, Università Milano - Bicocca, Piazza della Scienza 4, 20126, Milano, Italia.*

E-mail: s.remigi@campus.unimib.it; maria.frezzotti@unimib.it

Abstract

Raman spectroscopy has been used extensively to calculate CO_2 fluid density in many geological environments, based on the measurement of the Fermi diad split (Δ; cm^{-1}) in the CO_2 spectrum. While recent research has allowed the calibration of several Raman CO_2 densimeters, there is a limit to the inter-laboratory application of published equations. These calculate two classes of density values for the same measured Δ, with a deviation of 0.09 ± 0.02 g/cm^3 on average. To elucidate the influence of experimental parameters on the calibration of Raman CO_2 densimeters, we propose a bottom-up approach beginning with the calibration of a new equation to evaluate a possible instrument-dependent variability induced by experimental conditions. Then, we develop bootstrapped confidence intervals for density estimates of existing equations to move the statistical analysis from a sample-specific to a population level.

We find that Raman densimeter equations calibrated based on spectra acquired with similar spectral resolution calculate CO_2 density values lying within standard errors of equations and are suitable for the inter-laboratory application. The statistical analysis confirms that equations

calibrated at similar spectral resolution calculate CO_2 densities equivalent at 95% confidence, and each Raman densimeter does have a limit of applicability, statistically defined by a minimum Δ value, below which the error in calculated CO_2 densities is too high.

Keywords: Raman spectroscopy, Carbon dioxide, Raman densimeter equation, CO_2 density

DOI: https://doi.org/10.1177/0003702820987601

Introduction

Raman spectroscopy represents an attractive and popular technique to characterize a range of chemical and physical properties of Earth's fluids trapped as inclusions due to its non-destructive nature and high spatial resolution [1-3]. In particular, the calculation of the density of CO_2 fluids by Raman spectroscopy exploits the existing relation between the fluid density and the spectral position difference of the two main CO_2 bands in the Raman spectrum [4-11] (Fig. 1a).

Due to its linear symmetry, the CO_2 molecule is characterized by four vibrational modes: a symmetric stretching mode ν_1, an asymmetric stretching mode ν_3, and two bending modes $2\nu_{2a}$ and $2\nu_{2b}$ having the same vibrational frequencies. The symmetric stretching mode ν_1 has nearly the same energy and symmetry of the two bending modes $2\nu_2$. Thus, when activated, these become mutually repellent to one another and degenerate. This anharmonic coupling originates a vibrational resonance, known as "Fermi resonance" effect [12], which results in the splitting apart of two bands ($\nu_1 - 2\nu_2$, defined as "Fermi diad"; Fig.1a), having frequencies at 1388.2 (upper band) and 1285.4 cm^{-1} (lower band), respectively, at ambient conditions [13].

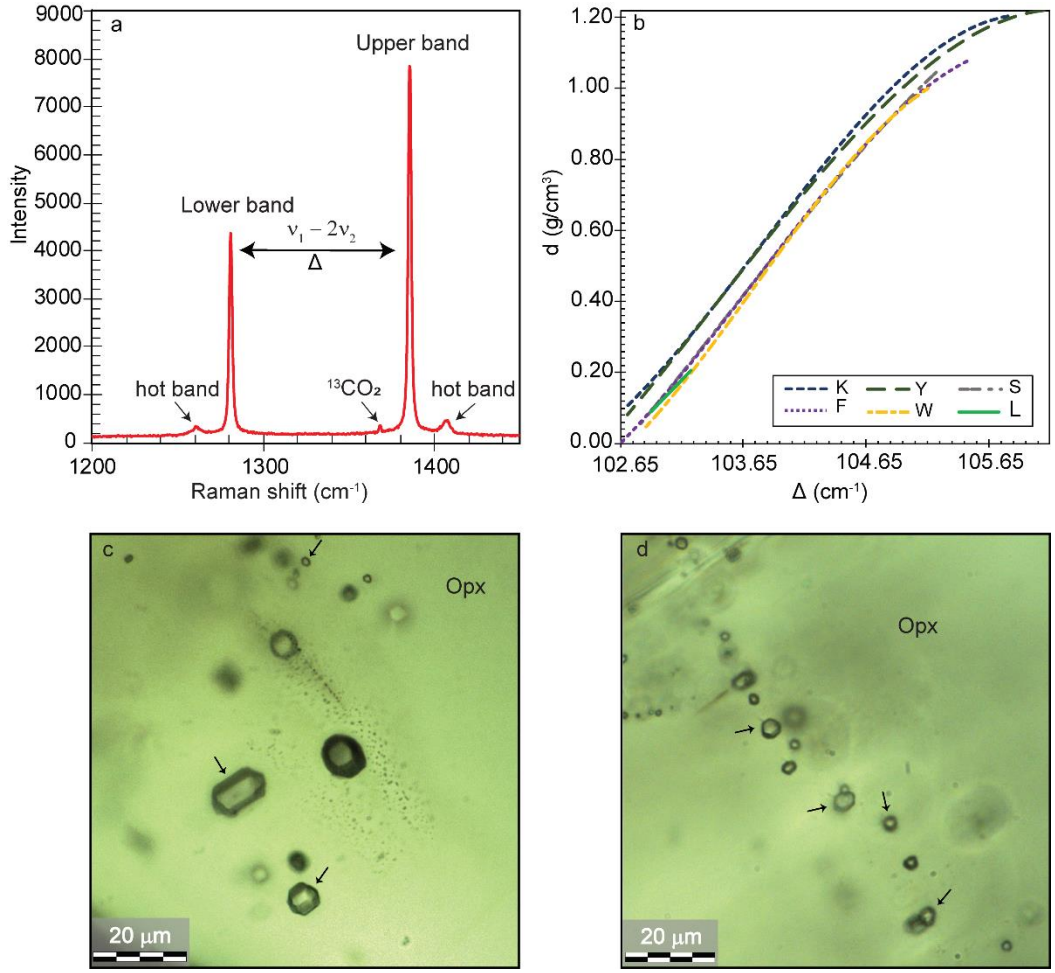

Fig.1 (previous page) a) CO_2 Raman spectrum of one fluid inclusion in a peridotite from El Hierro, Canary Islands. It is characterized by: the upper and lower bands, at 1384.93 cm^{-1} and 1279.76 cm^{-1}, composing the "Fermi diad" (v_1-$2v_2$); the two hot bands arising from the transitions originated due to the thermal energy of the molecules, at 1406.78 cm^{-1} and 1260.81 cm^{-1}; the $^{13}CO_2$ peak at 1367.45 cm^{-1}. The Fermi diad frequencies are shifted compared to those at ambient conditions due to the higher density of the fluid analyzed from mantle depth. b) Graphical expression of Raman densimeter empirical equations on a Δ – density plot. The linear equations of Rosso and Bodnar (1995) [11] and Lamadrid et al. (2017) [19] have been not considered since they are not comparable with all the other densimeter regressions. K = Kawakami et al. (2003) [14]; Y = Yamamoto and Kagi (2006) [15]; S = Song et al. (2009) [16]; F = Fall et al. (2011) [17]; W = Wang et al. (2011)[18]; L = Lamadrid et al. (2017) [19]. c) and d) Microphotographs of selected CO_2 fluid inclusions in orthopyroxene from spinel-harzburgite XML11. Black arrows indicate analysed fluid inclusions. Δ = distance of the Fermi diad split in cm^{-1}; I = intensity in arbitrary units (a.u.); d = density; Opx = orthopyroxene.

Raman CO_2 densimeter equations formalize the linear relation between the Fermi diad split (Δ; cm^{-1}) and CO_2 density (d; g/cm^3) [11,14-19]. These are empirically calibrated using CO_2 with known density calculated either by microthermometry of natural or synthetic fluid inclusions or using the equation of state (EOS) of CO_2 in optical pressure cells. Each densimeter equation is represented by a polynomial function, where the degree of the best fitting curve has been chosen based on the calculation of the root mean square error [19,20]. Although equations well fit descriptive statistics of data, published Raman densimeters calculate two distinct classes of density values for each Δ value measured in spectra, having a standard deviation of 0.09 ± 0.02 g/cm^3 on average (Fig. 1b). Each given CO_2 density value corresponds to Fermi diad splits showing an average wavenumber discrepancy of 0.2 cm^{-1} between the two classes of densimeters [14-19]. As a result, the application of Raman CO_2 densimeter equations to measure the density of CO_2 fluids in inclusions is limited to single laboratories. This difficulty suggests an instrument-dependent source of variability and poses the question of the reliability of the equations.

In the present study, we calibrate a new equation using Raman spectra of CO_2 inclusions in mantle rocks. The new equation calculates densities consistent with Kawakami et al. (2003) [14] and Yamamoto and Kagi (2006) [15], revealing a critical influence of the experimental parameters on spectra graphical output. An advanced statistic algorithm based on bootstrap [21] to calculate confidence interval is applied to evaluate the reliability of six CO_2 Raman densimeter polynomial equations, including the present study. Unknown data distributions, such as the Δ - d values, need robust statistical methods to move the analysis from a sample-specific level to a population setting, allowing generalization.

Present results demonstrate that densimeter equations calibrated applying a similar spectral resolution during Raman analysis calculate statistically equivalent density data at the 95% confidence. The bootstrap analysis extends the applicability of the densimeter equations to inter-

laboratory analysis by defining a set of rules guiding practitioners on how to choose and use published Raman densimeter equations to calculate CO_2 fluid density in fluid inclusions.

Materials and Methods

To calibrate the Raman densimeter equation, we performed Raman and microthermometric analyses in pure CO_2 fluid inclusions in olivine and orthopyroxene of peridotite xenoliths from El Hierro (Canary Islands) [22]. Inclusions are analysed in double-polished rock sections of about 150 µm thickness.

Microthermometry

Microthermometry of fluid inclusions has been performed with a Linkam THM 600 heating-freezing stage system coupled with a Leitz petrographic microscope (40X objective) at the Università di Milano - Bicocca. The system has been daily calibrated based on the measurement of H_2O and CO_2 triple point temperatures (*Tp*), using synthetic fluid inclusion standards SYNFLINC, with an error of ± 0.1°C. The temperatures of CO_2 phase transitions have been recorded through several freezing-heating cycles, with heating rates variable from 0.1 to 0.5°C/min in the temperature intervals close to phase transitions. Measured homogenization temperatures both to the liquid (*ThL)* and vapor phase (*ThV*) have been used to calculate densities with the CO_2 equation of state proposed by Dusheck et al. (1990) [23], with a standard error of ± 0.01 g/cm^3.

Raman spectroscopy

Raman analyses have been performed with the Horiba Jobin Yvon LabRam HRVIS Raman System at the Centro "G. Scansetti", Dipartimento di Scienze della Terra, Università di Torino. The system is equipped with a Horiba Jobin Yvon HR800 spectrometer, connected to an air-cooled 1024*256 px CCD detector, and provided with a wheel of six filters for laser attenuation and an Olympus BX41 microscope for petrographic observations in transmitted and reflected light. CO_2 spectra were recorded using a green Nd 532.06 nm laser source at 80 mW, with a 100X magnification. The experimental conditions were: a confocal hole of 200 µm, a slit width of 300 µm, and a 600 gr/mm grating, covering the spectral range between 105.35 and 1804.57 cm^{-1}, which correspond to a spectral resolution per pixel of 1.66 cm^{-1}. The Raman system has been further equipped with a Linkam THM 600 heating-freezing stage to analyze at a temperature (*T*) of 32°C (i.e., above the CO_2 critical *T* at 31.1°C) those inclusions characterized by the coexistence of vapor

(*V*) and liquid (*L*) phases at room temperature (18°C). Inclusions' spectra have been acquired through cycles of three accumulations, from 20 to 40 seconds each.

Most Raman spectra have been duplicated by setting a similar Raman analytical setup with the Horiba Jobin Yvon LabRAM HR Evolution Raman System, at the Dipartimento di Scienze dell'Ambiente e della Terra, Università di Milano – Bicocca. The system has a focal length of 800 mm, and it is connected to an air-cooled 1024*256 px CCD detector and a wheel of nine neutral density filters. An Olympus BXFM microscope allows analyses in transmitted and reflected light. CO_2 spectra were recorded using a green Nd 532.06 nm laser source, powered at 150 mW by mean of the 50% neutral density filter, with a 100X magnification. The analytical set up was: a confocal hole of 100 µm and a 600 gr/mm grating, allowing the coverage of a spectral range between 101.35 and 1548.92 cm^{-1}, corresponding to a spectral resolution of about 1.40 cm^{-1}/px. Spectra have been acquired by one accumulation of 30 seconds each.

In both laboratories, analyses have been performed at constant room temperature (e.g., within 1°C interval). The calibration of the two Raman systems has been daily performed to the zero line (the laser line emission) with a synthetic diamond standard vibrating at 1331.82 cm^{-1}, according to the ASTM 1840 – 96 (2007) normative [24,25]. For the Raman system at the Università di Torino, the correction of the instrumental linearity [19,26] has been performed by additionally checking the main band of the silicon standard at 520.70 cm^{-1}. Measured drift between the silicon and diamond spectral region resulted in less than 1 cm^{-1}, and has been corrected by the adjustment of the *Koeff.* parameter in the LabSpec 5 software, as recommended by Lamadrid et al. (2017) [19]. In the case of the spectrometers of the last generation, like the Raman system at the Università Milano - Bicocca, the correction of the instrumental linearity is automatically achieved by the automatic correction of the *Koeff*., by a sequential auto-calibration process to the zero line with the chosen standard in the CO_2 region (i.e., diamond; 1331.82 cm^{-1}).

With both instruments, the accuracy of the central band position attributions to monitor the variation of the band positions in Raman spectra as a function of the analyzed phases' physical-chemical characteristics, such as the fluid density, is in the order of 0.1 cm^{-1} [27]. For this reason, CO_2 spectra have been treated with baseline correction and band fitting with a Pseudo Voight function [28] by the freeware software Fityk 0.9.8 [29]. The fitting allows improving the measurement accuracy up to 30 times [15,30,31].

Bootstrapped confidence intervals

Five published CO_2 Raman densimeter polynomial equations [14-18] and the one proposed in the present study have been statistically evaluated by the computation of 95% confidence intervals of the fitted densities via the bootstrap approach. The linear equations of Rosso and Bodnar (1995) and Lamadrid et al. (2017) [11,19] have not been considered. The bootstrap algorithm, implemented in Rstudio 3.5.3, allowed computing the assumptions free 95% confidence intervals on the density estimates, enabling the analysis of the estimation accuracy of the different empirical equations and the statistical comparison among them.

The bootstrap [21] is a general nonparametric approach to statistical inference that allows constructing confidence limits on parameter estimates without assuming an underlying distribution. Among the different forms of bootstrapping – percentile bootstrap, time-series bootstrap, and regression bootstrap – we focused on regression bootstrap to construct confidence intervals on the dependent variable. In particular, given the following relation (Eq. 1):

$$d_i = \beta_0 + \beta_1 \Delta_i + \beta_2 \Delta_i^2 + \beta_3 \Delta_i^3 + \varepsilon_i \quad (1)$$

the 95% confidence intervals for the estimated d will be produced.

The literature recognizes two general approaches to bootstrap (Eq. 1) by considering the covariates as either random or fixed[32]. The densities used in Eq. 1 are observed from the Δs computed by each equation. Being each equation specific for a certain set of Δ, it is assumed that the Δs are fixed observations. At the same time, the response variable has a random component arising from the error associated with each equation. Being this the case, the 95% confidence intervals of the response variable will be constructed using the residual bootstrapping, described below [32]:

1) Estimate the regression coefficients β_0, β_1, β_2, and β_3 from the observed values and compute the fitted values and residuals defined as:

   - $\widehat{d_\iota} = \hat{\beta}_0 + \hat{\beta}_1 \Delta_i + \hat{\beta}_2 \Delta_i^2 + \hat{\beta}_3 \Delta_i^3$
   - $\varepsilon_i = d_i - \hat{d}_i$

2) Sample with replacement the residuals from the original regression and compute the bootstrapped values of the response variable:

- $\boldsymbol{\varepsilon_b^*} = [\varepsilon_{b1}^*, \varepsilon_{b1}^*, \dots, \varepsilon_{bn}^*]'$

- Define $d_{bi}^* = \hat{d}_i + \varepsilon_{bi}^*$, and compute $\boldsymbol{d_b^*} = [d_{b1}^*, d_{b2}^*, \dots, d_{bn}^*]'$

3) Regress $\boldsymbol{d_b^*}$ on the fixed regressors, and obtain the bootstrapped regression coefficients:

- $\boldsymbol{\beta_b^*} = [\beta_{b0}^*, \beta_{b1}^*, \beta_{b2}^*, \beta_{b3}^*]$

Points 1), 2), and 3) are repeated *B* times ($b \in [1; B]$) obtaining *B* coefficient estimates and, for each observation *i*, *B* bootstrapped prediction errors. For the scope of the paper, we will focus only on the construction of the 95% confidence intervals of the response variable. Once the *B* bootstrapped prediction errors are obtained, the 95% confidence intervals of the predicted response variable are constructed by selecting the 0.025 and 0.095 percentiles of the bootstrapped prediction errors and by adding these lower and upper bounds to each $\hat{d}_i$.

The 95% confidence interval (*CI*) is defined as a range of values that have been calculated from the data that, 95% of the time, includes the true value of the parameter, which is going to be estimated about the considered population [33]. This means that the *CI* could be used to provide a range of values that will contain the true population estimate.

In addition, a CI gives an indication of how precise the estimate is likely to be, with the margin of error as a measure of precision. If the CI is narrow, the margin of error is small; thus, the estimate is relatively precise; on the contrary, a wide CI implies a large margin of error; thus, the estimate has low precision [33]. Based on this, CI can be used to attribute the accuracy of the estimated fitted values and/or regressors coefficients.

The confidence interval can also be adopted to compare the estimation and predictive ability of two models: if the CIs for two models significantly overlap, then it constitutes an indication of (statistical) equivalence, at a given significance level, between the two [34].

Finally, it is essential to highlight that, if the regression bootstrap allows constructing CIs without assuming an underlying distribution of the dependent variable, by keeping the Δ fixed, it assumes that:

1) The error terms are independent and identically distributed (*iid*), and consequentially - when resampling - we have [35]:

$$P(\varepsilon_{bi}^* = \varepsilon_i) = \frac{1}{n}, \qquad \forall n = 1, \dots, n$$

which means that all the residuals have the same probability *P* to be randomly selected without any sampling biases.

2) The model in Eq. 1 is correctly specified [32].

Results

Calibration of the Raman CO_2 densimeter equation

Selected CO_2 inclusions for the calibration of the Raman densimeter equation have prismatic to rounded shapes, and sizes ranging from 2 to 20 µm in diameter or length (Fig.1c and d; cf., Supplementary Material, Table S.1). Some inclusions have elongated prismatic shapes with widths not exceeding 1-1.5 µm. Depths location within the rock sections range from 8 to 43 µm, with most of the inclusions observed at depths comprised between 15 and 25 µm from the sample surface (cf., Supplementary Material, Table S.1).

Data acquisition: microthermometry and Raman spectroscopy

CO_2 melting temperatures (*Tm*) are recorded at -56.6 ± 0.1°C. Homogenization temperatures to the liquid phase (*ThL*) range from -32.5 to 31.0 ± 0.1°C. Two fluid inclusions homogenize to the vapor phase (*ThV*) at 30.5 ± 0.1 and 30.9 ± 0.1°C. Corresponding CO_2 densities are calculated with the equation of state of Dusheck et al. (1990) [23] and range from 0.37 to 1.08 ± 0.01 g/cm^3 (cf., Supplementary Material, Table S.1).

In Raman spectra of 40 pure fluid inclusions, CO_2 upper bands' central positions are distributed from 1386.42 to 1389.88 cm^{-1}, and lower bands' central positions between 1281.57 and 1286.11 cm^{-1} (cf., Supplementary Material, Table S.2). Based on the fitted centre positions of the upper and lower CO_2 bands of acquired spectra, measured Δs vary from 103.44 to 105.13 cm^{-1} on increasing fluid density. Intensities of CO_2 upper bands are comprised between 110 and 9350 counts (in arbitrary units), with most values above 1000 counts. The lower band intensities are between 64 and 4688 counts (in arbitrary units), also in this case, with most values above 1000 counts. The band full widths at half maximum (*FWHM*) range from 2.00 to 5.06 cm^{-1} for the upper bands, and from 2.20 to 4.80 cm^{-1} for the lower bands (cf., Supplementary Material, Table S.2).

For comparison, we measured the Fermi diad splits' distance in a few CO_2 spectra collected with a higher spectral per pixel resolution (i.e., 1800 gr/mm grating). We note that measured Δs resulted in being about 0.2 cm^{-1} greater on average (cf. Supplementary material, Figure S.1).

Band fitting accuracy

The selection of CO_2 Raman bands to calibrate a densimeter equation is generally based on a minimum intensity value, selected between 500 and 1000 counts by the different authors[14]. The accuracy of the central band position, however, is not only a function of band intensity (*I*) but also of its full width at half maximum (*FWHM*) [2,28]. Therefore, for the present study, spectra selection for band best-fit has also been performed by considering the ratio between *FWHM* and *I* in single bands – defined as "band shape factor" (*BSF = FWHM/I*).

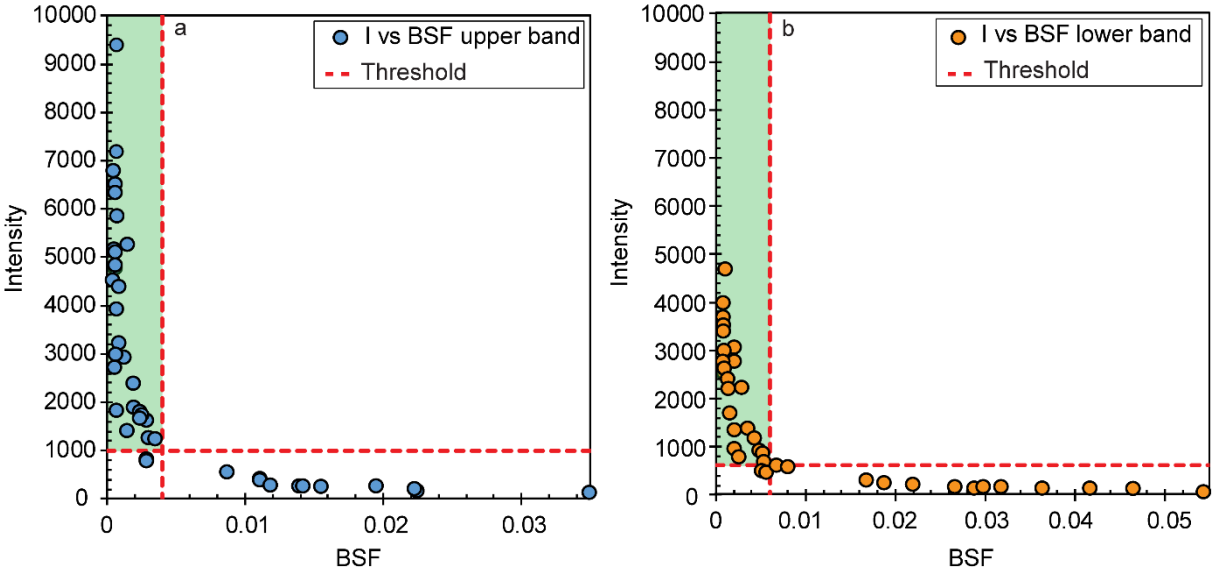

Fig.2 (previous page) Intensities (*I*) versus band shape factors (*BSF*) of fitted CO_2 upper (a) and lower bands (b). The horizontal and vertical dotted red lines cross into the points where the hyperboles invert their slope and represent the threshold value for selecting accurate spectra.

Calculated *BSFs* show a strong anticorrelation between band intensity and *FWHM* and vary from 0.0003 to 0.0349 for the CO_2 upper bands and from 0.0006 to 0.0545 for the lower bands (cf., Supplementary Material, Table S.2). The *BSF* plots relative to *I* (Figures 2a and b)~~,~~ graphically illustrate this relationship for the two CO_2 bands forming the Fermi doublet. In both diagrams, data plots define hyperbolic distributions, suggesting a minimum *I* over which and maximum *FWHM* below which the bands can be selected for best-fit. The threshold values have been set at the points where the hyperboles invert their slopes (crossing ~~of~~ red lines in Fig. 2a and b). The data plotting below the threshold values correspond to CO_2 upper bands (green field in Fig. 2a) having

intensities ≥ 1000 counts and a *BSF* ≤ 0.004, and lower bands (green field in Fig. 2b) ≥ 600 counts and *BSF* ≤ 0.006. At higher *BSF* values, band intensities exponentially decrease with increasing *FWHM*, for both the upper and lower bands, inducing an increase of uncertainty in central position assignment.

It was expected that both the CO_2 upper bands and lower bands in the same spectrum would have similar *BSF*. Based on this approach, we removed 13 spectra from the database (cf., Supplementary Material, Table S.2). Unconsidered spectra were collected in CO_2 inclusions of density variable from 0.42 to 1.02 g/cm^3, excluding a correlation between *BSF* variability and fluid density. Conversely, these inclusions share several textural characteristics, including a location deeper than 25 µm within the sample, a size not exceeding 5 µm in length, and, often, an elongated shape (width of about 1-1.5 µm; Fig. 1c and d). Thus, one possible explanation is that confocal Raman spectroscopy analyses performed in tiny fluid inclusions located deep within the sample may have contributed to insufficient spectral output quality. The penetration profile for a laser source depends mainly on its wavelength, sample optical properties, and hole size [2,36], and it decreases with increasing depth. For this reason, a small volume of fluid located deep within the sample will be excited by the laser only to a lesser extent compared to the surrounding host mineral. As a consequence, the graphical resolution of spectra acquired beyond a certain depth would rapidly decrease [27,30,36].

Calculation of CO_2 densimeter equation

The interpolation of the selected measured Δs and corresponding microthermometric densities (cf., Table 1) allows formulating an empirical third-order polynomial equation for the calculation of the CO_2 densities (Eq. 2):

$$d = -0.01472000\Delta^3 + 4.51148969\Delta^2 - 460.27795107\Delta + 15631.28847817 \quad (2)$$

with trend analysis determination coefficient, R^2, equal to 0.994. The resulting regression is shown in Fig. 3a.

Table 1 Summary of the independently calculated densities (*d*) and *Δ* values of the twenty-seven selected fluid inclusions. Homogenization temperatures (*Th*) are also reported.

Host	**FI n°**	***d* (g/cm^3)**	***Th* (°C)**		***Δ* (cm^{-1})**
Opx	XML3B_120	0.37	30.5	*V*	103.44
Opx	XML3B_125	0.47	30.95	*L*	103.62
Opx	XML3B_122	0.62	29.2	*L*	103.97
Opx	XML3B_128	0.64	28.5	*L*	103.99
Ol	XML4B_112	0.68	26.5	*L*	104.07
Ol	XML4B_111	0.71	24.9	*L*	104.13
Ol	XML4B_102	0.71	24.9	*L*	104.07
Ol	XML4B_101	0.73	23.8	*L*	104.15
Ol	XML4B_109	0.73	23.6	*L*	104.17
Ol	XML4B_113	0.73	23.6	*L*	104.11
Ol	XML4B_100	0.73	23.6	*L*	104.12
Ol	XML4B_116	0.73	23.5	*L*	104.13
Ol	XML4B_110	0.76	23.2	*L*	104.23
Opx	XML3B_24	0.90	3.9	*L*	104.52
Opx	XML3B_26	0.92	2.1	*L*	104.65
Opx	XML3B_25	0.92	0.9	*L*	104.74
Ol	XML4B_16	0.94	-2.0	*L*	104.67
Opx	XML3B_28	0.94	-2.5	*L*	104.63
Opx	XML3B_23	0.95	-3.4	*L*	104.74
Ol	XML4B_12	0.95	-4.0	*L*	104.68
Opx	XML3B_27	1.02	-17.0	*L*	104.85
Ol	XML10C_8	1.04	-21.9	*L*	105.04
Ol	XML10C_13	1.05	-23.5	*L*	105.05
Ol	XML10C_10	1.05	-24.5	*L*	105.06
Opx	XML11B_6	1.06	-25.9	*L*	105.07
Opx	XML8A_19	1.07	-29.4	*L*	105.07
Opx	XML8A_17	1.08	-30.5	*L*	105.13

FI = Fluid inclusion; n° = number; Opx = orthopyroxene; Ol = olivine; *V* = vapor; *L* = liquid; *Δ* = distance of the Fermi diad split.

Equation 2 has been used to calculate the selected inclusions' densities: for the considered *Δ* intervals, Raman densities resulted between 0.37 and 1.08 g/cm^3. Calculated CO_2 densities have an almost perfect positive correlation with microthermometric inclusions densities, with a mathematical expression (Eq. 3):

$$d_{micro.} = 1.0002(d_{Rd}) + 0.0027 \quad (3)$$

where $d_{micro.}$ are CO_2 densities derived from microthermometric measurements, and d_{Rd} those calculated using the Raman densimeter equation. The resulting regression is shown in Figure 3b,

and it is characterized by a trend analysis determination coefficient equal to 0.994 and a standard error of ± 0.015 g/cm^3.

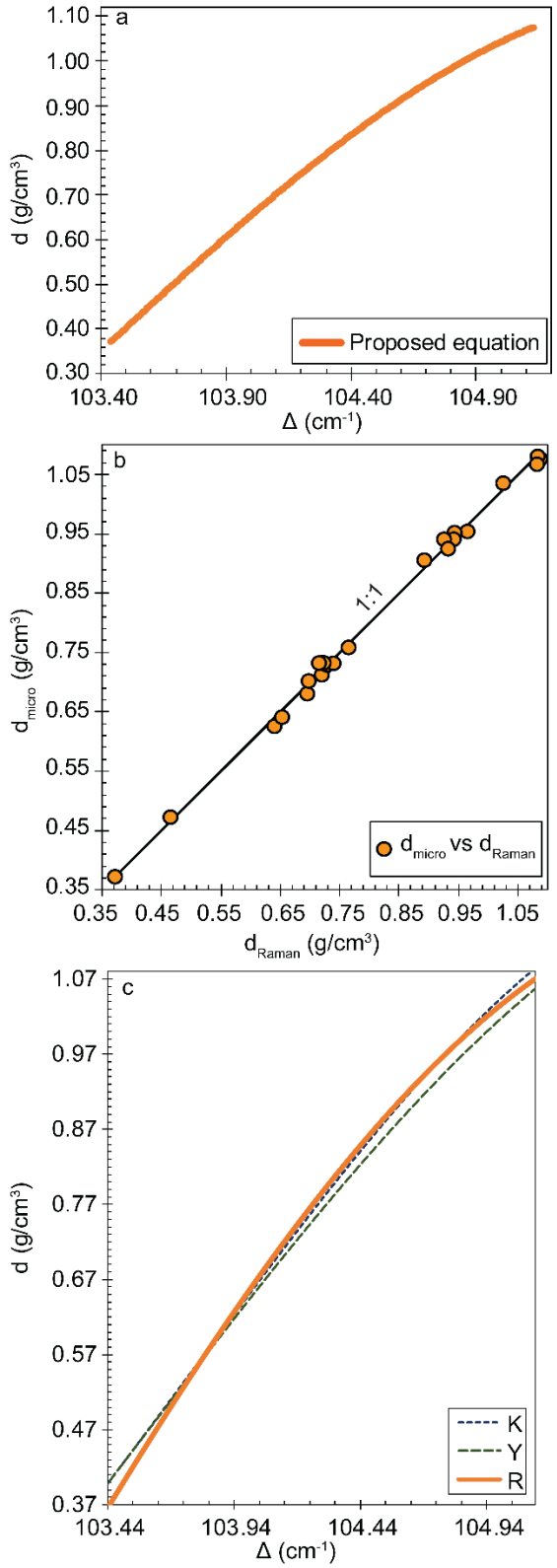

Fig.3 Graphical expression of proposed densimeter equation. a) Third order polynomial regression curve (orange) obtained by interpolating selected Δ - d relations. b) Regression of "microthermometric" densities (d_{micro}) versus

"Raman" densities (d_{Raman}). The solid black line shows the correlation between the d_{micro} and d_{Raman}. c) Graphical comparison of present study, R, Kawakami et al. (2003) [14], K, and Yamamoto and Kagi (2006) [15], Y, densimeter regressions on a $\Delta - d$ plot. Δ = distance of the Fermi diad split; d = density.

As illustrated in Figure 3c, when plotted on a Δ vs d diagram, the present regression curve groups with Kawakami et al. (2003) [14] and Yamamoto and Kagi (2006) [15] ones, calculating CO_2 density values lying within the standard errors of the equations ($\sigma = \pm 0.015$ g/cm^3) for density values equal or higher than 0.37 g/cm^3. Compared to Kawakami et al. (2003) [14] equation (K in Fig. 3c), it calculates densities that show a slight underestimation below 0.37 g/cm^3 (Δs equal to 103.44 cm^{-1}, Fig.3c). The larger discrepancy is -0.03 g/cm^3. This minimal difference progressively decreases and remains within an interval of 0.01 g/cm^3 from 0.54 to 1.08 g/cm^3 (Δ between 103.76 and 105.13 cm^{-1}; Fig. 3c).

Again, when compared with the regression curve of Yamamoto and Kagi (2006) [15] (Y in Fig. 3c), the present equation shows the same slight density underestimation below 0.37 g/cm^3 (Δs equal to 103.44 cm^{-1}); progressively, the density difference decreases crossing Yamamoto and Kagi (2006) [15] value at 0.59 g/cm^3 (Δ of 103.86 cm^{-1}; Fig. 3c). The present densimeter calculates density values lying within the analytical error of Yamamoto and Kagi (2006) 15 equation for higher densities. It reaches a maximum density difference of 0.03 g/cm^3 at 0.80 g/cm^3 (Δs equal to 104.33 cm^{-1}). The trend is reversed at 0.98 g/cm^3 (Δs equal to 104.81 cm^{-1}), where the density difference is 0.01 g/cm^3 at 1.08 g/cm^3 (Δs equal to 105.13 cm^{-1}; Fig. 3c).

Conversely, a robust disagreement is observed with the other set of densimeter equations, i.e., by Song et al. (2009), Fall et al. (2011), and Wang et al. (2011) [16-18]. These equations calculate density values all lying well below those calculated by the present equation, with an average standard deviation of -0.09 ± 0.02 g/cm^3 in the whole range of considered densities.

Confidence intervals of Raman densimeter equations

A bootstrap analysis was used to estimate confidence intervals of the predictions of density values of the six Raman densimeter equations considered in the present paper. The calibration data were selected from the original Δ and density data used by the different authors to calibrate densimeters.

Table 2 Empirical equations (orthogonal polynomial) used for residual bootstrapping.

Equation	independent new equations	*Std. Error* (g/cm^3)	*Adj.* R^2
Kawakami et al. (2003) [14]	$-0.118963\Delta^3 - 0.241733\Delta^2 + 2.359035\Delta + 0.727095$	0.02	0.998
Yamamoto and Kagi (2006) [15]	$-0.12567\Delta^3 - 0.448236\Delta^2 + 2.762602\Delta + 0.846051$	0.02	0.998
Song et al. (2009) [16]	$-0.022998\Delta^3 - 0.040964\Delta^2 + 1.260887\Delta + 0.662$	0.01	0.998
Fall et al. (2011) [17]	$-0.097391\Delta^3 - 0.183873\Delta^2 + 2.990265\Delta + 0.686497$	0.01	0.999
Wang et al. (2011) [18]	$-0.09871\Delta^3 - 0.13213\Delta^2 + 2.71578\Delta + 0.54435$	0.01	0.998
Present study	$0.031447\Delta^3 - 0.105221\Delta^2 + 1.014913\Delta + 0.844902$	0.02	0.985

Δ = distance between the Fermi diad split; *Std. Error* = standard error; *Adj.* R^2 = adjusted R^2.

The empirical equations used for the bootstrap approach fit orthogonal polynomials as opposed to raw polynomials to reduce possible problems arising from the correlation among the different covariates.

The bootstrap analysis allows constructing the 95% confidence intervals from which it is possible not only to compare the different equations found in the literature but also to define a limit of applicability to each empirical regression. The cut-off point has been defined where the relative distances (between lower and upper limits) of the computed *CIs* are below than 7.5%. Above this threshold, the fitted density values are assumed not reliable due to the high variability coupled with the observed exponential increase. Figure 4 shows the computed thresholds and the densities variability in % for the six regressions. For Kawakami et al. (2003) [14] (K in Fig. 4a), Yamamoto and Kagi (2006) [15] (Y in Fig. 4b) and the present study (R in Fig. 4c) equations, the thresholds are located at Δs equal to 103.59, 103.59, and 103.44 cm^{-1}, respectively. These correspond to fitted densities of 0.46 g/cm^3 for Kawakami et al. (2003) and Yamamoto and Kagi (2006) [14,15], and 0.37 cm^3 for the present study (Figs. 4 a,b, c). Above these fitted density values, most relative distances for the three considered equations are < 5%. In the case of the empirical regressions of Kawakami et al. (2003) and Yamamoto and Kagi (2006) [14,15], the calculated density variability below the threshold is above 30% (Fig. 4a and b). In the case of our equation, due to the considered dataset, no fitted densities fall above the threshold value (Fig. 4c).

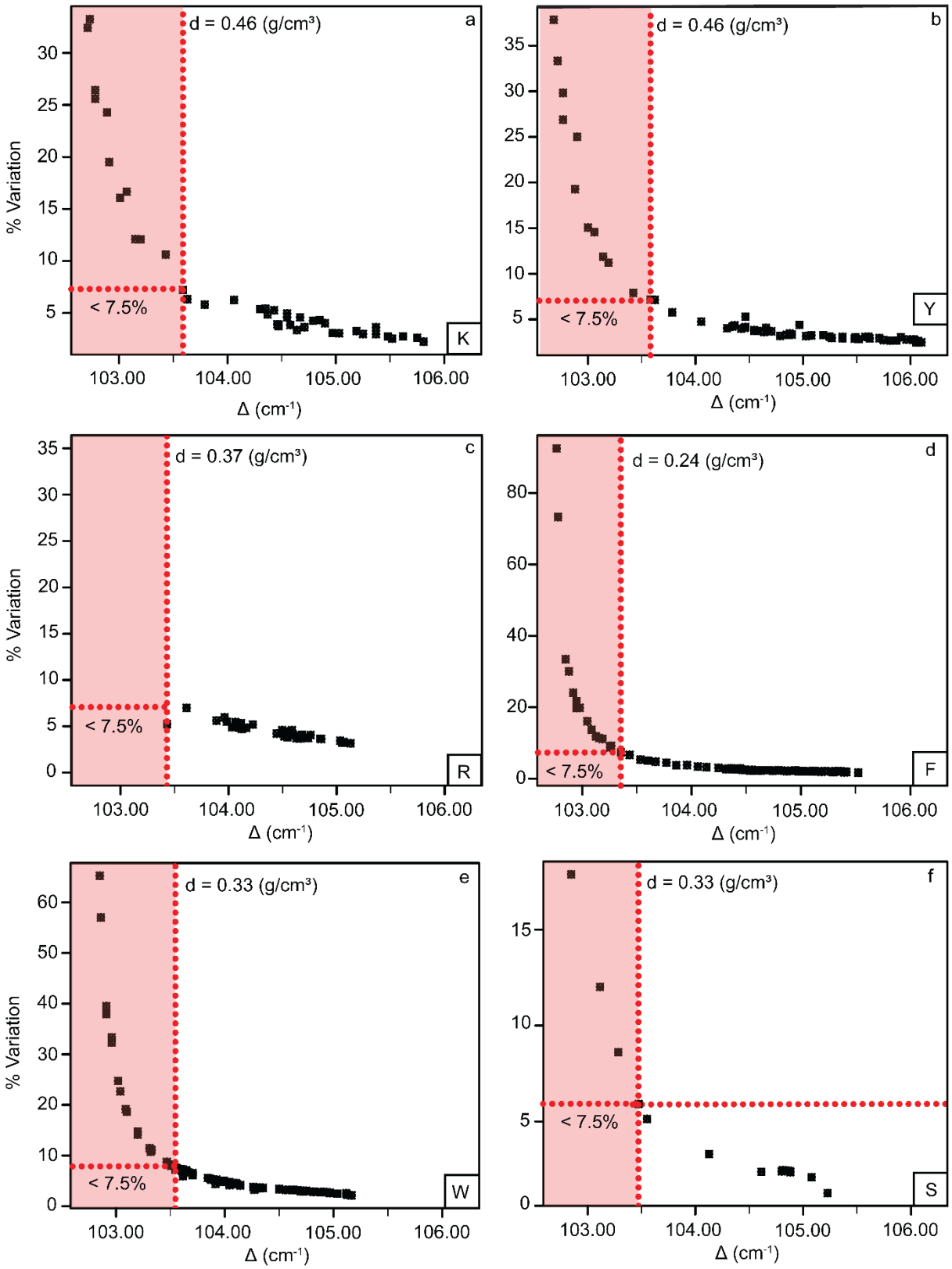

Fig.4 Plots of the percent variation (*%Variation*) of fitted densities (*Fitted d*) vs. *Δ* values, obtained after the residual bootstrapping for the equations of K, Y, and R (Fig.4 a, b, c; cf., Fig. 1b) and F, W and S (Fig.4 d, e, f; cf. Fig.1b). The red dotted lines represent the *Δ* - density threshold values above which the relative error of the fitted density values is lower than 7.5%; the red fields correspond to those *Δ* - densities below the minimum reliable values defined by the statistic thresholds. *Δ* = distance of the Fermi diad split.

For the empirical regressions of Fall et al. (2011) (F in Figs. 4d), Wang et al. (2011) (W in Fig. 4e), and Song et al. (2009) (S in Fig. 4f) [16-18], the 7.5% thresholds correspond to Δs equal to 103.33, 103.53, and 103.45 cm^{-1}, respectively. The relative density values are 0.24 g/cm^3 for Fall et al. (2011), and 0.33 g/cm^3 for Wang et al. (2011) and Song et al. (2009) [16-18] equations (Fig. 4d, e, and f). The relative errors before the thresholds exponentially increase for all the new equations, reaching the maximum variation of about 90% for Fall et al. (2011) (Fig. 4d), 60% for Wang et al. (2011) (Fig. 4e), and 15% for Song et al. (2009) (Fig. 4f) [16-18] equations.

Discussion

The influence of experimental procedure on the calibration of Raman CO2 densimeter equations

The present densimeter equation shows an excellent correlation with equations proposed by Kawakami et al. (2003) [14] and Yamamoto and Kagi (2006) (cf. Fig. 3c) [15]. Measured Δs calculate CO_2 density values lying within the standard errors of the equations.

In these three laboratories, Raman spectra were collected at similar spectral resolution: 1.66 cm^{-1}/px for the present study and 1.50 cm^{-1}/px for Kawakami et al. (2003) and Yamamoto and Kagi (2006) [14,15] (cf., Table 3). In addition, as summarized in Table 3, the applied experimental conditions include very similar spectrometer characteristics (i.e., the spectrometer focal length), the same CCD detector (1024*256 px) and a diffraction grating (600 gr/mm), and very close laser source wavelengths (i.e., 532 nm for the present study, and 514 nm [14,15]).

We note that the spectral resolution applied to calibrate the other discrete group of Raman densimeter equations by Song et al. (2009), Fall et al. (2011), and Wang et al. (2011) [16-18] is also similar, but considerably higher, between 0.30 and 0.43 cm^{-1}/px.

Table 3 Review of the analytical conditions adopted by different authors to calibrate Raman densimeter equations.

Densimeter equation	*Rosso and Bodnar (1995)* [11]	*Kawakami et al. (2003)* [14]	*Yamamoto and Kagi (2006)* [15]	*Song et al. (2009)* [16]	*Fall et al. (2011)* [17]	*Wang et al. (2011)* [18]	*Lamadrid et al. (2017)* [19]	*Present study*
Polynomial regression	Linear	Cubic	Cubic	Cubic	Cubic	Cubic	Linear	Cubic
Fluid inclusions	synthetic H_2O-CO_2	natural and synthetic pure CO_2	natural and synthetic pure CO_2	synthetic nearly pure CO_2	synthetic H_2O-CO_2 , variable salinity	synthetic pure CO_2	Optical cell pure CO_2	natural pure CO_2
Δ range (cm^{-1})	102.60 - 105.20	102.71 - 105.81	102.71 - 106.10	102.82 - 105.22	102.65 - 105.47	102.83 - 105.16	102.64 - 103.23	103.44 - 105.13
d range (g/cm^3)	0.03 - 1.00	0.10 - 1.22	0.10 -1.24	0.06 - 1.05	0.001 - 1.08	0.05 - 1.00	0.001 - 0.21	0.37 - 1.07
Equation of state	Sterner and Bodnar, 1991 [37]	Pitzner and Sterner, 1994 [38]	Pitzner and Sterner, 1994 [38]	Angus et al., 1976 [39]	Span and Wagner, 1996 [40]	Span and Wagner, 1996 [40]	Span and Wagner, 1996 [40]	Dusheck et al., 1990 [23]
Spectrometer	Dilor XY	Chromex 250is	Chromex 250is	Horiba HR	Horiba HR	Horiba HR	Horiba HR	Horiba HR
Laser (nm)	514.5	514.5	514.5	532.06	514.5	532.06	514.5	532.06
Slit (μm)	100	-	-	-	150	-	-	300
Dispersion grating (gr/mm)	1200	600	600	1800	2400	1800	1800	600
CCD	1024*256	1024*256	1024*256	1024*256	1024*256	1024*256	1024*256	1024*256
Spectral resolution (cm^{-1}/px)	0.84	1.5	1.5	0.3	0.3	0.43	0.575	1.66
Calibration standard	Ne lines	Naphtalene	Naphtalene	Diamond	Ne lines	Diamond and Benzonitrile	Ne lines	Diamond
d error (g/cm^3)	±0.02	±0.02	±0.02	±0.03	±0.035	±0.011	±0.0034	±0.015

Δ = distance of the Fermi diad split; *d* = density; - = not reported; CCD = Charge Coupled Device.

In conclusion, we suggest that spectral resolution represents the prevailing experimental parameter affecting the Raman spectra of CO_2 fluids having the same density and, consequently, the observed differences among the two groups of densimeters.

A similar observation is entirely consistent with the fundamentals of Raman spectroscopy. The spectral resolution determines the Raman spectrometer's ability to measure, for example, the *FWHM* of a thin band or to discriminate between overlapping bands [27,41] (e.g., number of points forming the bands). Five main parameters generally define it: 1) the spectrometer focal length, 2) the number of the pixels in the detector, 3) the laser wavelength, 4) the slit width, and 5) the diffraction grating. Among these, the diffraction grating is the most relevant one: the higher the number of grooves of the grating per mm, the higher the spectral resolution. When the spectral resolution is changed, both the band *FWHM* and *I* vary [42], reflecting on the band's centre position in the spectral graphical output. Thus, on fitting, bands obtained with a higher spectral resolution would show a lower shift of centre positions than those obtained with a lower spectral resolution. Since the distance of band centre positions depends on the spectra graphical output, the shift is constant for the all Δ values.

Statistical comparison of existing densimeters based on bootstrapped confidence intervals

The bootstrapping analysis predicts that Raman densimeter equations are not reliable to calculate CO_2 densities in the intervals where the relative distances of predicted *CI* are higher than 7.5%~~,~~ due to lower precision of fit. We note a general trend for each Raman densimeter equation best-fit dependent on the spectral resolution set to perform analyses. Predicted minimum density values to be considered reliable measurements are higher for those equations calibrated on Raman spectra acquired at medium spectral resolution conditions. Owing to this observation, we performed a statistical comparison of the new datasets independent regressions [34] (cf., Section 3.2). The distances of the Fermi diad split measured by one group of authors have been used to calculate CO_2 densities using the empirical regression estimated from the densities computed by another group of authors and successively compared with their *CIs* (Figs. 5 and 6). As an example, the Δs measured by Kawakami et al. (2003) [14] have been used to predict densities with the regression of Yamamoto and Kagi (2006) [15]; the resulting fitted density regression curve has been plotted against the *CIs* of Kawakami et al. (2003) (Fig. 5b) [14]. If the fitted values fall inside the 95% confidence intervals, one can conclude that the two equations are statistically equivalent at 95% confidence. To test and evaluate the influence of the analytical conditions on the calibration of densimeter equations, the

comparison was performed among equations resulting from Raman spectra collected with similar experimental conditions.

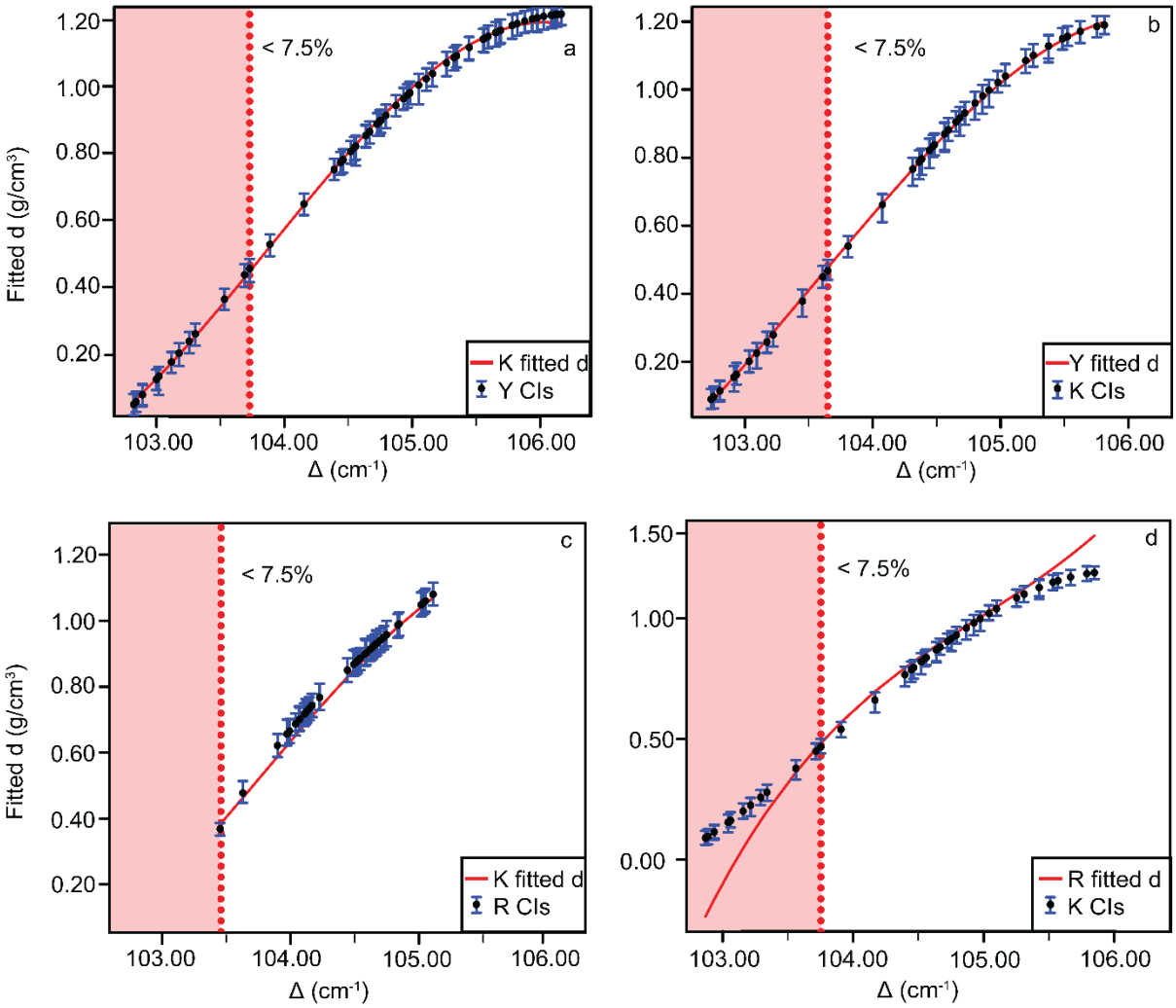

Fig.5 Statistical comparison of the dataset independent new empirical regressions, obtained after the residual bootstrapping for the "medium spectral resolution" equations (K, Y, and R). *Δs* measured by Y are used to calculate fitted densities (*Fitted d*) with K equation (a) and compared with Y's confidence intervals (*CIs*). *Δs* measured by K are used to calculate *Fitted d* with Y (b) and R (d) new equations and compared with K's *CIs*. *Δs* measured by R are used to calculate *Fitted d* with K equation (c) and compared with R's *CIs*. Red dotted line and red field as in Fig. 4; *Δ* = distance of the Fermi diad split. Abbreviations as in Fig. 1b.

The comparison between fitted densities and confidence intervals [34], shows an overlap of the 95% *CIs* between Kawakami et al. (2003), Yamamoto and Kagi (2006) [14-15] and the present study equations (Fig. 5a,b,c). This result indicates that these three "medium spectral resolution" equations are statistically equivalent at 95% of confidence. As illustrated in Fig. 5d, the statistical equivalence is limited to the range of the computed densities on which the equations are calibrated. Outside these ranges of density values, the proposed equations are no longer statistically equivalent.

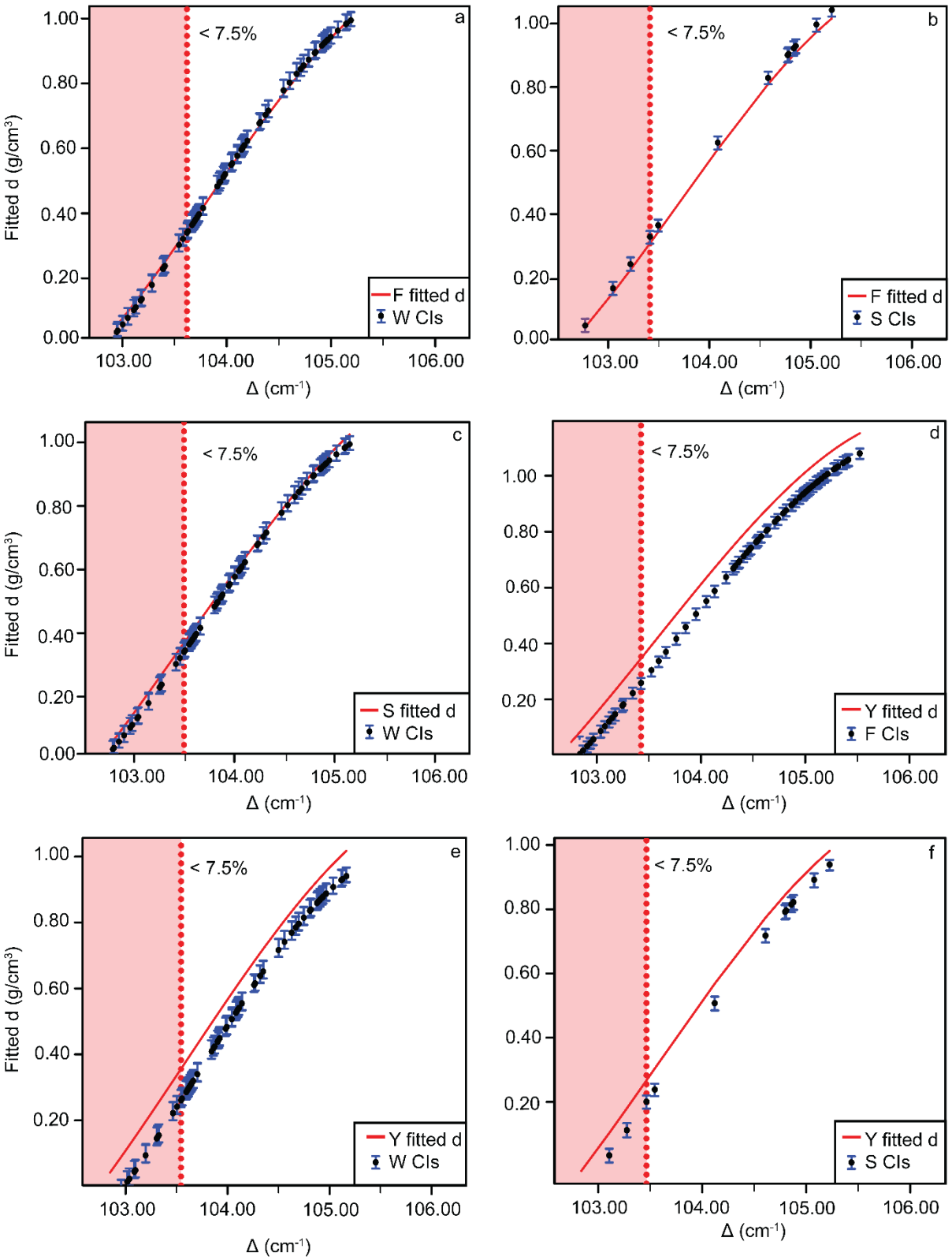

Fig.6 Statistical comparison of the dataset independent new empirical regressions, obtained after the residual bootstrapping for the "high spectral resolution" equations (F, W, and S; Fig.6 a,b,c) and the "medium and the high spectral resolution" equations (Y, F, W, and S; Fig.6 d,e,f). *Δs* measured by W (a) and S (b) are used to calculate fitted densities (*Fitted d*) with F new equation and compared with W and S's confidence intervals (*CIs*), respectively. *Δs* measured by W are used to calculate *Fitted d* by S new equation (c) and compared with W's *CIs*. *Δs* measured by F (d), W (e), and S (f) are used to calculate fitted densities (*Fitted d*) with Y new equation and, then, compared with F, W, and

S's confidence intervals (*CIs*), respectively. Red dotted line and red field as in Figs. 4; Δ = distance of the Fermi diad split. Abbreviations as in Fig. 1b.

The comparison between Fall et al. (2011), Wang et al. (2011) and Song et al. (2009) [16-18] calculated densities and *CIs* [34], shows - at 95% confidence - that also "high spectral resolution" equations are statistically equivalent in the density interval comprised between 0.33 and 1.00 g/cm^3 (Fig. 6 a,b and c). Conversely, the statistical analysis shows that equations calibrated using different Raman spectral resolutions are not statistically equivalent (Fig. 6 d, e, and f).

Thus, the bootstrap analysis provides a guide to select a CO_2 densimeter equation based on the applied experimental procedure. For spectra collected with a spectral resolution of 1.50 - 1.66 cm^{-1}/px, and for density values between 0.46 and 1.22 g/cm^3 (Δ from 103.59 to 105.81 cm^{-1}), any equation among those of Kawakami et al. (2003), Yamamoto and Kagi (2006) [14,15] and the present study could be used to calculate CO_2 densities with a confidence of 95% that the fitted values will be statistically equivalent. Also the equation proposed in the present study can be applied for the density interval between 0.37 and 1.08 g/cm^3 (Δ from 103.44 to 105.13 cm^{-1}). Conversely, when a spectral resolution of 0.30 - 0.43 cm^{-1}/px is applied, Fall et al. (2011), Wang et al. (2011) and Song et al. (2009) [16-18] densimeter equations should be used to calculate CO_2 densities with a confidence of 95% that the fitted values will be statistically equivalent.

Applicability of Raman CO_2 densimeter equations

The present results suggest no strong reason to avoid the inter-laboratory adoption of published Raman densimeter equations to calculate densities of CO_2 fluid inclusions once the spectral resolution (cm^{-1}/px) applied during analyses is considered. A firm agreement in calculated density values is observed within the two groups of equations, calibrated at high and medium spectral resolutions, and could be regarded as a reliable measurement for comparison. The statistical analysis further predicts that each Raman CO_2 densimeter equation does have a limit of applicability, statistically defined by a minimum Δ value, below which the error in calculated densities is too high. The minimum statistically accurate density values (< 7.5% *CI*) are different for each considered equation; they vary from 0.46 to 0.37 g/cm^3, and from 0.33 to 0.24 g/cm^3, depending on the spectral resolution applied and the interval of data considered (Fig. 4). The error exponentially increases at lower density values, standing above 20% at about 0.20 g/cm^3 for all equations (Fig. 4).

Minimum statistically accurate density values correspond to CO_2 fluids homogenizing to the vapor phase (*ThV; L+V→ V*) at temperatures variable from 31.0 to 30.0°C, and 29.6 - 24.8°C, close

to the critical point of CO_2 (P = 7.38 MPa; T = 31.1°C) (Supplementary Figure S.2). Therefore, the simulated increasing trend of error could reflect a considerably lower accuracy of *ThV* measurements performed to calibrate the equations [43]. The "apparent homogenization phenomenon" - proposed by Sterner (1992) [44] to highlight the underdetermination of phase transitions in fluid inclusions homogenizing by vapor expansion - can induce an error as high as 0.10 - 0.30 g/cm^3 in calculated CO_2 densities.

However, an applicability limit also applies to those densimeter equations calibrated based on measurements in optical gas cells, where CO_2 density is not determined by phase transitions [45]. In addition, it is evident that "high spectral resolution" densimeter equations calculate minimum statistically reliable density values that are lower than those of "medium spectral resolution" ones. Thus, other factors affecting the calibration of densimeter equations should be considered. In Raman spectra of CO_2, bands' position and width are a function of the molecular forces dominating the fluid volumes at different states and variable *P-T* conditions [46-49]. Consequently, not only the Fermi diad split (Δ) but also band intensity (I) and width (*FWHMs*) correlate with the fluid density [4-11]. Band line shape is also an essential but seldom discussed characteristics that could influence the determination of band intensity, central position, and area. Based on ab initio calculations, Cabaço et al. (2007) [47] reported some discrepancies between observed and theoretically expected CO_2 band central positions resulting from the variation of band profiles with fluid density. In the case of high-density liquid-like CO_2 (e.g., d = 1.2 - 0.5 g/cm^3), authors reported a progressive symmetric broadening of the upper and lower bands with increasing fluid density, allowing the accurate measurement of CO_2 bands' central positions. Conversely, below the critical density, gas-like (d = 0.34 g/cm^3) CO_2 narrower bands showed progressively increasing asymmetric profiles, resulting in more challenging to obtain a sufficiently accurate fitting of central positions. Although further investigation is required, it is probable that growing asymmetry of band profiles in spectra of low-density CO_2 could affect the accuracy of the band fitting, and hence of the calculated density values.

Conclusions

The present study demonstrates the possibility of inter-laboratories application of Raman densimeter equations to calculate the CO_2 density in fluid inclusions. A set of comments guiding the practitioners on how to choose and use a Raman densimeter equation to allow that the fitted values will be statistically equivalent at 95% confidence, includes:

- The selected Raman CO_2 densimeter equation should be calibrated with the same (or similar) spectral resolution conditions.

- The selected Raman CO_2 densimeter equation should be applied only within the range of the density dataset used to calibrate the equation.

- The selected Raman CO_2 densimeter equation should be further applied limited to the interval of CO_2 density lying above a minimum reliable density value predicted by the bootstrapping, corresponding to a cut-off point where the relative distances of the computed *CIs* are lower than 7.5%.

One main consequence of present results is that the Raman densimeter method could potentially be applied to calculate CO_2 densities near and above the critical density value, which encompass *P-T* conditions relevant for most geological processes in the crust and the mantle. We believe that method could become a more widespread analytical tool in the study of Earth's fluids in the near future and with the proposed improvements. On the contrary, the present results suggest caution in applying the Raman densimeters to CO_2 mass calculation in shrinkage bubbles of melt inclusions. Here, CO_2 has a considerably lower density, in the range from 0.02 to 0.30 g/cm^3 [50-53], in most cases below the minimum reliable density value predicted by our statistical analysis.

Acknowledgments

The present work is part of the Ph.D. thesis of S.R.. This research was funded by MIUR projects to M.L.F.: PRIN 2017 (n. 2017LMNLAW) and Dipartimenti di Eccellenza (2018-2022). S.F. acknowledges the support of the University of Torino - Ricerca locale 2018 and 2019, and of the ANVUR - Fondo Finanziamento delle Attività Base di Ricerca. Raman analytical facilities in Torino were provided by the Interdepartmental Centre "G. Scansetti" for Studies on Asbestos and Other Toxic Particulates and by the Compagnia di San Paolo, Torino. Raman analytical facilities in Milano - Bicocca were provided by The Dipartimento di Scienze dell'Ambiente e della Terra.

Declaration of Conflicting Interests

The Authors declare that there is no conflict of interests.

References

1. M. L. Frezzotti, S. Ferrando, F. Tecce, and D. Castelli. “Water content and nature of solutes in shallow-mantle fluids from fluid inclusions”. Earth Planet. Sci. Lett. 2012a. 351: 70-83. https://doi.org/10.1016/j.epsl.2012.07.023

2. M. L. Frezzotti, F. Tecce, and A. Casagli. “Raman spectroscopy for fluid inclusion analysis”. J. Geochem. Explor. 2012b. 112: 1-20. DOI: 10.1016/j.gexplo.2011.09.009

3. R. J. Bodnar, and M. L. Frezzotti. “Micro-scale Chemistry: Raman analyses of Fluid and Melt Inclusions”. Elements. 2020. 16**(**2): 93-98

4. C. G. Gray, and J. V. Kranendonk. “Calculation of the pressure broadening of rotational Raman lines due to multipolar and dispersion interaction”. Can. J. Phys. 1966. 44(10): 2411-2430. https://doi.org/10.1139/p66-197

5. C. H. Wang, and R. B. Wright. “Effect of density on the Raman scattering of molecular fluids. I. A detailed study of the scattering polarization, intensity, frequency shift, and spectral shape in gaseous N_2”. J. Chem. Phys. 1973. 59(4): 1706-1712. https://doi.org/10.1063/1.1680252

6. Y. Garrabos, R. Tufeu, B. Le Neindre, G. Zalczer, and D. Beysens. “Rayleigh and Raman scattering near the critical point of carbon dioxide”. J. Chem. Phys. 1980. 72(8): 4637-4651. https://doi.org/10.1063/1.439706

7. J. F. Bertrán. “Study of the Fermi doublet ν1—2ν2 in the Raman spectra of CO_2 in different phases”. Spectrochim. Acta, Part A. 1983. 39(2): 119-121. https://doi.org/10.1016/0584-8539(83)80066-X

8. Y. Garrabos, V. Chandrasekharan, M. A. Echargui, and F. Marsault-Herail. “Density effect on the Raman Fermi resonance in the fluid phases of CO_2”. Chem. Phys. Lett. 1989a. 160(3): 250-256. https://doi.org/10.1016/0009-2614(89)87591-8

9. Y. Garrabos, M. A. Echargui, and F. Marsault-Herail. “Comparison between the density effects on the levels of the Raman spectra of the Fermi resonance doublet of the $^{12}C^{16}O_2$ and $^{13}C^{16}O_2$ molecules”. J. Chem. Phys. 1989b. 91(10): 5869-5881. DOI: 10.1063/1.457455

10. J. C. Seitz, J. D. Pasteris, and I. M. Chou. “Raman spectroscopic characterization of gas mixtures; I, Quantitative composition and pressure determination of CH_4, N_2 and their mixtures”. Am. J. Sci. 1993. 293(4): 297-321. DOI: 10.2475/ajs.293.4.297

11. K. M. Rosso, and R. J. Bodnar. “Microthermometric and Raman spectroscopic detection limits of CO_2 in fluid inclusions and the Raman spectroscopic characterization of CO_2”. Geochim. Cosmochim. Acta. 1995. 59(19): 3961-3975. https://doi.org/10.1016/0016-7037(95)94441-H

12. E. Fermi. “Über den Ramaneffekt des kohlendioxyds”. Z. Phys. 1931. 71(3-4): 250-259.

13. H. R. Gordon, and T. K. McCubbin. “The 2.8-micron bands of CO_2”. J. Mol. Spectrosc. 1966. 19(1): 137-154. https://doi.org/10.1016/0022-2852(66)90237-2

14. Y. Kawakami, J. Yamamoto, and H. Kagi. “Micro-Raman densimeter for CO_2 inclusions in mantle-derived minerals”. Appl. Spectrosc. 2003. 57(11): 1333-1339. https://doi.org/10.1366/000370203322554473

15. J. Yamamoto, and H. Kagi. “Extended micro-Raman densimeter for CO_2 applicable to mantle-originated fluid inclusions”. Chem. Lett. 2006. 35(6): 610-611. https://doi.org/10.1246/cl.2006.610

16. Y. Song, I. M. Chou, W. Hu, B. Robert, and W. Lu. “CO_2 Density-Raman Shift Relation Derived from Synthetic Inclusions in Fused Silica Capillaries and Its Application”. Acta Geol. Sin. (Engl. Ed.). 2009. 83(5): 932-938. https://doi.org/10.1111/j.1755-6724.2009.00090.x

17. A. Fall, B. Tattitch, and R. J. Bodnar. “Combined microthermometric and Raman spectroscopic technique to determine the salinity of H_2O–CO_2–NaCl fluid inclusions based on clathrate melting”. Geochim. Cosmochim. Acta. 2011. 75(4): 951-964. https://doi.org/10.1016/j.gca.2010.11.021

18. X. Wang, I. M. Chou, W. Hu, R. C. Burruss, Q. Sun, and Y. Song. “Raman spectroscopic measurements of CO_2 density: Experimental calibration with high-pressure optical cell (HPOC) and fused silica capillary capsule (FSCC) with application to fluid inclusion observations”. Geochim. Cosmochim. Acta. 2011. 75(14): 4080-4093. https://doi.org/10.1016/j.gca.2011.04.028

19. H. M. Lamadrid, L. R. Moore, D. Moncada, J. D. Rimstidt, R. C. Burruss, and R. J. Bodnar. “Reassessment of the Raman CO_2 densimeter”. Chem. Geol. 2017. 450: 210-222. https://doi.org/10.1016/j.chemgeo.2016.12.034

20. Y. Hagiwara, J. Torimoto, and J. Yamamoto. “Pressure measurement and detection of small H_2O amounts in high-pressure H_2O–CO_2 fluid up to 141 MPa using Fermi diad splits and bandwidths of CO_2”. J. Raman Spectrosc. 2020. 51(6): 1003-1018. https://doi.org/10.1002/jrs.5865

21. B. Efron. “Bootstrap methods: Another look at the jackknife”. Ann. Stat. 1979. 7(1): 1-26

22. E. Oglialoro, M. L. Frezzotti, S. Ferrando, C. Tiraboschi, C. Principe, G. Groppelli, and I. M. Villa. “Lithospheric magma dynamics beneath the El Hierro Volcano, Canary Islands: insights from fluid inclusions”. Bull. Volcanol. (Heidelberg). 2017. 79(10): 70. DOI: 10.1007/s00445-017-1152-6

23. W. Duschek, R. Kleinrahm, and W. Wagner. “Measurement and correlation of the (pressure, density, temperature) relation of carbon dioxide II. Saturated-liquid and saturated-vapor densities and the vapor pressure along the entire coexistence curve”. J. Chem. Thermodyn. 1990. 22(9): 841-864. https://doi.org/10.1016/0021-9614(90)90173-N

24. ASTM, 2007. E1840–96: Standard Guide for Raman Shift Standards for Spectrometer Calibration.

25. D. Hutsebaut, P. Vandenabeele, and L. Moens. “Evaluation of an accurate calibration and spectral standardization procedure for Raman spectroscopy”. Analyst. 2005. 130(8): 1204-1214. https://doi.org/10.1039/B503624K

26. F. Lin, A. K. Sum, and R. J. Bodnar. “Correlation of methane Raman ν1 band position with fluid density and interactions at the molecular level”. J. Raman Spectrosc. 2007. 38(11): 1510-1515. https://doi.org/10.1002/jrs.1804

27. J. Dubessy, M. C. Caumon, F. Rull, and S. Sharma. “Instrumentation in Raman spectroscopy: elementary theory and practice”. In: J. Dubessy, M. C. Caumon, F. Rull. Raman spectroscopy applied to earth sciences and cultural heritage. London: European Mineralogical Union and the Mineralogical Society of Great Britain and Ireland, 2012. 12, 3, 83-172. https://hal.univ-lorraine.fr/hal-01342830

28. X. Yuan, and R. A. Mayanovic. “An empirical study on Raman peak fitting and its application to Raman quantitative research”. Appl. Spectrosc. 2017. 71(10): 2325-2338.

29. M. Wojdyr. “Fityk: a general-purpose peak fitting program”. J. Appl. Crystallogr. 2010. 43(5-1): 1126-1128. https://doi.org/10.1107/S0021889810030499

30. S. Fukura, T. Mizukami, S. Odake, and H. Kagi. “Factors determining the stability, resolution, and precision of a conventional Raman spectrometer”. Appl. Spectrosc. 2006. 60(8): 946-950. https://doi.org/10.1366/000370206778062165

31. J. Yamamoto, H. Kagi, Y. Kawakami, N. Hirano, and M. Nakamura. “Paleo-Moho depth determined from the pressure of CO_2 fluid inclusions: Raman spectroscopic barometry of mantle-and crust-derived rocks”. Earth Planet. Sci. Lett. 2007. 253(3-4): 369-377.

32. J. Fox. “Bootstrapping Regression Models. Appendix to an R and S-PLUS Companion to Applied Regression”. In: J. Fox. An R and S-PLUS Companion to Applied Regression. Sage Publication, 2002.

33. G. Cumming, and R. Calin-Jageman. Introduction to the new statistics: Estimation, open science, and beyond. New York: Routledge, 2016

34. M. Kuhn, and K. Johnson. Applied predictive modelling. New York: Springer, 2013. 13

35. N. Balakrishnan, and W. Chen. CRC handbook of tables for order statistics from inverse Gaussian distributions with applications. New York: Routledge, 2017

36. E. A. Burke. “Raman microspectrometry of fluid inclusions”. Lithos. 2001. 55(1-4): 139-158. DOI: 10.1016/S0024-4937(00)00043-8

37. S. M. Sterner, and R. J. Bodnar. “Synthetic fluid inclusions; X, Experimental determination of PVTX properties in the CO_2-H_2O system to 6 kb and 700 degrees”. Am. J. Sci. 1991. 291(1): 1-54. DOI:10.2475/ajs.291.1.1

38. K. S. Pitzer, and S. M. Sterner. “Equations of state valid continuously from zero to extreme pressures for H_2O and CO_2”. J. Chem. Phys. 1994. 101(4), 3111-3116.j https://doi.org/10.1063/1.467624

39. S. Angus, B. Armstrong, and K. M. De Reuck. “Carbon Dioxide - International Thermodynamic Tables of the Fluid State, Bd. 3”. In: S. Angus, B. Armstrong, and K. M. De Reuck. Oxford – New York: Pergamon Press Ltd. pure and mixed refrigerants, 1976.

40. R. Span, and W. Wagner. “A new equation of state for carbon dioxide covering the fluid region from the triple-point temperature to 1100 K at pressures up to 800 MPa”. J. Phys. Chem. Ref. Data. 1996. 25(6): 1509-1596. https://doi.org/10.1063/1.555991

41. F. Adar. “Raman Microscopy Analysis of Molecular Orientation in Organic Fibers”. Spectroscopy. 2013. 28(2): 14-22.

42. C. K. Mann, and T. J. Vickers. “Instrument-to-instrument transfer of Raman spectra”. Appl. Spectrosc. 1999. 53(7): 856-861. https://doi.org/10.1366/0003702991947441

43. E. Roedder. Fluid inclusions. Chantilly: Mineralogical Society of America (MSA), 1984. 12

44. S. M. Sterner. “Homogenization of fluid inclusions to the vapor phase; the apparent homogenization phenomenon”. Econ. Geol. 1992. 87(6): 1616-1623. https://doi.org/10.2113/gsecongeo.87.6.1616

45. T. Kobayashi, J. Yamamoto, T. Hirajima, H. Ishibashi, N. Hirano, Y. Lai, ... and S. Arai. “Conformity and precision of CO_2 densimetry in CO_2 inclusions: Microthermometry versus Raman microspectroscopic densimetry”. J. of Raman Spectrosc. 2012. 43(8), 1126-1133. https://doi.org/10.1002/jrs.3134

46. H. Nakayama, K. I. Saitow, M. Sakashita, K. Ishii, and K. Nishikawa. “Raman spectral changes of neat CO_2 across the ridge of density fluctuation in supercritical region”. Chem. Phys. Lett. 2000. 320(3-4): 323-327. https://doi.org/10.1016/S0009-2614(00)00249-9

47. M. I. Cabaço, S. Longelin, Y. Danten, and M. Besnard. “Local density enhancement in supercritical carbon dioxide studied by Raman spectroscopy”. J. Phys. Chem. A. 2007. 111(50): 12966-12971. https://doi.org/10.1021/jp0756707

48. M. I. Cabaço, M. Besnard, S. Longelin, and Y. Danten. “Evolution with the density of CO_2 clustering studied by Raman spectroscopy”. J. Mol. Liq. 2010. 153(1): 15-19. https://doi.org/10.1016/j.molliq.2009.09.007

49. Jr D. M. Sublett, E. Sendula, H. Lamadrid, M. Steele-MacInnis, G. Spiekermann, R. C. Burruss, and R. J. Bodnar. “Shift in the Raman symmetric stretching band of N_2, CO_2, and CH_4 as a function of temperature, pressure, and density”. J. Raman Spectrosc. 2019. 51(3): 1-14. https://doi.org/10.1002/jrs.5805

50. R. Esposito, R. J. Bodnar, L. V. Danyushevsky, B. De Vivo, L. Fedele, J. Hunter, A. Lima, and N. Shimizu. “Volatile evolution of magma associated with the Solchiaro eruption in the Phlegrean Volcanic District (Italy)”. J. Petrol. 2011. 52(12): 2431-2460. https://doi.org/10.1093/petrology/egr051

51. L. R. Moore, E. Gazel, R. Tuohy, A. S. Lloyd, R. Esposito, M. Steele-MacInnis, ..., and R. J. Bodnar. “Bubbles matter: An assessment of the contribution of vapor bubbles to melt inclusion volatile budgets”. Am. Mineral. 2015. 100(4): 806-823. https://doi.org/10.2138/am-2015-5036

52. E. M. Aster, P. J. Wallace, L. R. Moore, J. Watkins, E. Gazel, and R. J. Bodnar. “Reconstructing CO_2 concentrations in basaltic melt inclusions using Raman analysis of vapor bubbles”. J. Volcanol. Geoth. Res. 2016. 323: 148-162. https://doi.org/10.1016/j.jvolgeores.2016.04.028

53. P. Robidoux, M. L. Frezzotti, E. H. Hauri, and A. Aiuppa. “Shrinkage Bubbles: The C–O–H–S Magmatic Fluid System at San Cristóbal Volcano”. J. Petrol. 2018. 59(11): 2093-2122. https://doi.org/10.1093/petrology/egy092

7.1 Supplementary Material

7.1.1 Supplementary Tables

Table S.1 Summary of the main characteristics of seventy-two selected fluid inclusions.

Host	FI n.°	size (µm)	depth (µm)	Tm (°C)	Th (°C)		d (g/cm^3)
Opx	XML3B_120	8	43	-56.6	30.5	V	0.37
Opx	XML3B_121	7	40	-56.6	30.92	V	0.42
Opx	XML3B_125	6	33	-56.6	30.95	L	0.47
Opx	XML3B_122	4	43	-56.6	29.2	L	0.62
Opx	XML3B_124	4	42	-56.6	29.1	L	0.63
Opx	XML3B_128	9	35	-56.6	28.5	L	0.64
Ol	XML4B_112	8	32	-56.6	26.5	L	0.68
Ol	XML4B_111	8	32	-56.6	24.9	L	0.71
Ol	XML4B_102	6	26	-56.6	24.9	L	0.71
Ol	XML4B_101	12	27	-56.6	23.8	L	0.73
Ol	XML4B_100	10	31	-56.6	23.6	L	0.73
Ol	XML4B_116	8	17	-56.6	23.5	L	0.73
Ol	XML4B_113	7	32	-56.6	23.6	L	0.73
Ol	XML4B_109	6	33	-56.6	23.6	L	0.73
Ol	XML4B_110	8	32	-56.6	23.2	L	0.76
Opx	XML8C_29	4	26	-56.6	13.0	L	0.84
Opx	XML8C_26	4	27	-56.6	8.3	L	0.87
Opx	XML8C_30	10	24	-56.6	8.9	L	0.87

Opx	XML8C_23	6	27	-56.6	7.4	L	0.88
Opx	XML8C_28	14	23	-56.6	7.8	L	0.88
Opx	XML8C_25	5	25	-56.6	5.6	L	0.89
Opx	XML8C_24	5	23	-56.6	5.6	L	0.89
Opx	XML3B_24	2	25	-56.6	3.9	L	0.90
Opx	XML3B_41	2	25	-56.6	2.0	L	0.92
Opx	XML3B_26	2.5	26	-56.6	2.1	L	0.92
Opx	XML8C_27	4	30	-56.6	0.6	L	0.92
Opx	XML3B_39	4	30	-56.6	1.0	L	0.92
Ol	XML3B_25	3.5	26	-56.6	0.9	L	0.92
Ol	XML3B_28	3	25	-56.6	-2.5	L	0.94
Opx	XML4B_16	5	39	-56.6	-2.0	L	0.94
Opx	XML4B_12	4	10	-56.6	-4.0	L	0.95
Opx	XML3B_23	2.5	23.5	-56.6	-3.4	L	0.95
Opx	XML3B_27	4	30	-56.6	-17.0	L	1.02
Opx	XML3B_42	2.5	26	-56.6	-17.1	L	1.02
Ol	XML10C_8	4	15	-56.6	-21.9	L	1.04
Ol	XML10C_13	5	13	-56.6	-23.5	L	1.05
Ol	XML10C_16	3	17	-56.6	-24.5	L	1.05
Opx	XML11B_6	6	20	-56.6	-25.9	L	1.06
Opx	XML8A_19	20	14	-56.6	-29.4	L	1.07
Opx	XML8A_17	7	14	-56.6	-30.5	L	1.08

Ol	XML11B_7	4	18	-56.7	13.0	L	0.84
Ol	XML3B_31	5	40	-56.7	8.7	L	0.87
Opx	XML11B_11	5	15	-56.9	7.5	L	0.88
Ol	XML11B_12	3.5	17.5	-56.6	5.7	L	0.89
Ol	XML4B_15	2.5	12.5	-56.6	-3.8	L	0.95
Opx	XML3A_34	3	24	-57.1	-5.5	L	0.96
Ol	XML4B_13	8	10	-56.6	-5.4	L	0.96
Ol	XML4B_14	2	16	-56.7	-7.0	L	0.97
Opx	XML3A_35	5	26	-57.0	-11.5	L	0.99
Opx	XML10C_7	4	20	-56.6	-13.0	L	1.00
Ol	XML3A_33	3.5	22	-56.9	-15.5	L	1.01
Ol	XML10C_5	3	17	-56.6	-18.3	L	1.02
Ol	XML10C_1	5	21	-56.8	-23.7	L	1.05
Ol	XML10C_3	4	21	-56.6	-24.2	L	1.05
Opx	XML11B_14	6	15	-56.6	-24.3	L	1.05
Opx	XML11B_15	6.5	8	-56.6	-24.6	L	1.05
Opx	XML10C_2	3	22	-56.7	-26.2	L	1.06
Opx	XML10C_38	4	26	-56.6	-16.5	L	1.02
Ol	XML10C_10	3	17	-56.6	-16.5	L	1.02
Opx	XML10C_1b	5	21	-56.6	-24.0	L	1.05
Opx	XML10C_3b	4	21	-56.6	-24.0	L	1.05
Ol	XML4B_17	4.5	33	-56.6	-11.9	L	0.99

Opx	XML10C_2b	3	22	-56.6	-25.0	L	1.05
Opx	XML10C_11b	3	27	-56.6	-20.3	L	1.03
Ol	XML4B_13	8	10	-56.6	-10.0	L	1.05
Ol	XML4B_115	6	14.5	-56.6	25.2	L	0.71
Ol	XML4B_117	10	23	-56.6	21.4	L	0.76
Opx	XML11B_3	5	15	-56.6	-32.5	L	1.09
Opx	XML11B_1	4	10	-56.6	-32.1	L	1.08
Opx	XML11B_4	5	9	-56.6	12.1	L	0.85
Opx	XML4B_115b	5	14.5	-56.6	25.2	L	0.71
Opx	XML4B_117b	10	23	-56.6	21.4	L	0.76

Reported densities (d) are calculated based on recorded fluid inclusions' homogenization temperatures (Th), measured by microthermometry. Final melting temperatures are also reported (Tm). FI = fluid inclusion; n° = number; Opx = orthopyroxene; Ol = olivine; V = vapor; L = liquid.

Table S.2 Summary of the parameters (position, intensity and full width at half maximum) of the CO_2 Fermi diads measured after the fitting of collected CO_2 Raman spectra, and band shape factors calculated for the upper (BSF^+) and the lower (BSF^-) bands. Microthermometric density (d) is also reported.

FI n.°	d (g/cm^3)	Band$^+$ (cm^{-1})	Band$^-$ (cm^{-1})	I$^+$ (a.u.)	I$^-$ (a.u.)	FWHM$^+$	FWHM$^+$	BSF$^+$	BSF$^-$
XML3B_120	0.37	1389.41	1285.97	3208	1623	2.00	2.40	0.0006	0.0015
XML3B_121	0.42	1389.39	1285.98	799	434	2.33	2.50	0.0029	0.0058
XML3B_125	0.47	1389.73	1286.11	1734	931	2.00	2.20	0.0012	0.0024
XML3B_122	0.62	1388.80	1284.83	1314	792	2.22	2.22	0.0017	0.0028
XML3B_124	0.63	1389.15	1285.25	841	463	2.45	2.50	0.0029	0.0054
XML3B_128	0.64	1389.04	1285.05	2911	1705	2.40	2.40	0.0008	0.0014
XML4B_112	0.68	1388.31	1284.20	4576	2367	2.30	2.50	0.0005	0.0011
XML4B_111	0.71	1388.32	1284.11	4821	2477	2.35	2.30	0.0005	0.0009
XML4B_102	0.71	1388.44	1284.37	6449	3551	2.20	2.40	0.0003	0.0007
XML4B_101	0.73	1388.56	1284.38	6781	3692	2.37	2.25	0.0003	0.0006
XML4B_100	0.73	1387.99	1283.88	7156	3984	2.37	2.50	0.0003	0.0006
XML4B_116	0.73	1388.43	1284.31	6336	3406	2.37	2.40	0.0004	0.0007
XML4B_113	0.73	1388.30	1284.16	4878	2600	2.36	2.50	0.0005	0.0010
XML4B_109	0.73	1388.26	1284.09	5098	2736	2.00	2.30	0.0004	0.0008
XML4B_110	0.76	1388.16	1283.93	3902	2169	2.39	2.56	0.0006	0.0012
XML8C_29	0.84	1389.79	1285.34	276	136	3.92	4.08	0.0142	0.0301
XML8C_26	0.87	1389.60	1285.10	110	64	3.84	3.50	0.0349	0.0545
XML8C_30	0.87	1389.79	1285.24	303	144	3.60	3.86	0.0119	0.0268

XML8C_23	0.88	1389.35	1284.83	274	143	4.26	4.54	0.0155	0.0319
XML8C_28	0.88	1389.69	1285.16	347	174	3.76	3.86	0.0108	0.0222
XML8C_25	0.89	1389.45	1284.86	196	105	4.34	4.40	0.0221	0.0419
XML8C_24	0.89	1389.35	1284.75	163	89	3.64	4.16	0.0223	0.0467
XML3B_24	0.90	1386.95	1282.43	1798	888	4.06	4.56	0.0023	0.0051
XML3B_41	0.92	1389.75	1285.16	439	229	3.84	3.90	0.0088	0.0170
XML3B_26	0.92	1387.02	1282.40	1166	576	4.48	4.74	0.0038	0.0082
XML8C_27	0.92	1389.59	1284.96	272	134	3.78	3.88	0.0139	0.0290
XML3B_39	0.92	1389.88	1285.18	194	110	3.78	4.04	0.0195	0.0367
XML3B_25	0.92	1386.76	1282.03	2371	1196	4.29	4.56	0.0018	0.0038
XML3B_28	0.94	1386.77	1282.14	2869	1401	4.22	4.70	0.0015	0.0034
XML4B_16	0.94	1387.46	1282.79	1486	820	4.70	4.50	0.0032	0.0055
XML4B_12	0.95	1387.07	1282.39	5159	2724	5.06	4.80	0.0010	0.0018
XML3B_23	0.95	1386.73	1281.99	1655	901	4.50	4.60	0.0027	0.0051
XML3B_27	1.02	1386.42	1281.57	1605	849	4.70	4.60	0.0029	0.0054
XML3B_42	1.02	1389.70	1284.84	380	206	4.10	3.90	0.0108	0.0189
XML10C_8	1.04	1386.80	1281.77	9350	4688	4.40	4.52	0.0005	0.0010
XML10C_13	1.05	1387.30	1282.25	4314	2186	4.92	4.80	0.0011	0.0022
XML10C_10	1.05	1386.82	1281.76	5827	3024	4.20	4.72	0.0007	0.0016
XML11B_6	1.06	1387.98	1282.91	2669	1342	2.16	2.20	0.0008	0.0016
XML8A_19	1.07	1389.17	1284.10	1194	596	3.92	4.16	0.0033	0.0070
XML8A_17	1.08	1389.07	1283.94	1510	758	4.28	4.24	0.0028	0.0056

Red values correspond to the spectra which are not considered accurate based on the intensity and the band shape factor thresholds. FI = fluid inclusion; n° number; $Band^+$ = upper band position; $Band^-$ = lower band position; I^+ = upper band intensity; I^- = lower band intensity; $FWHM^+$ = upper band full width at half maximum; $FWHM^-$ = upper band full width at half maximum.

7.1.1 Supplementary Figure S.1

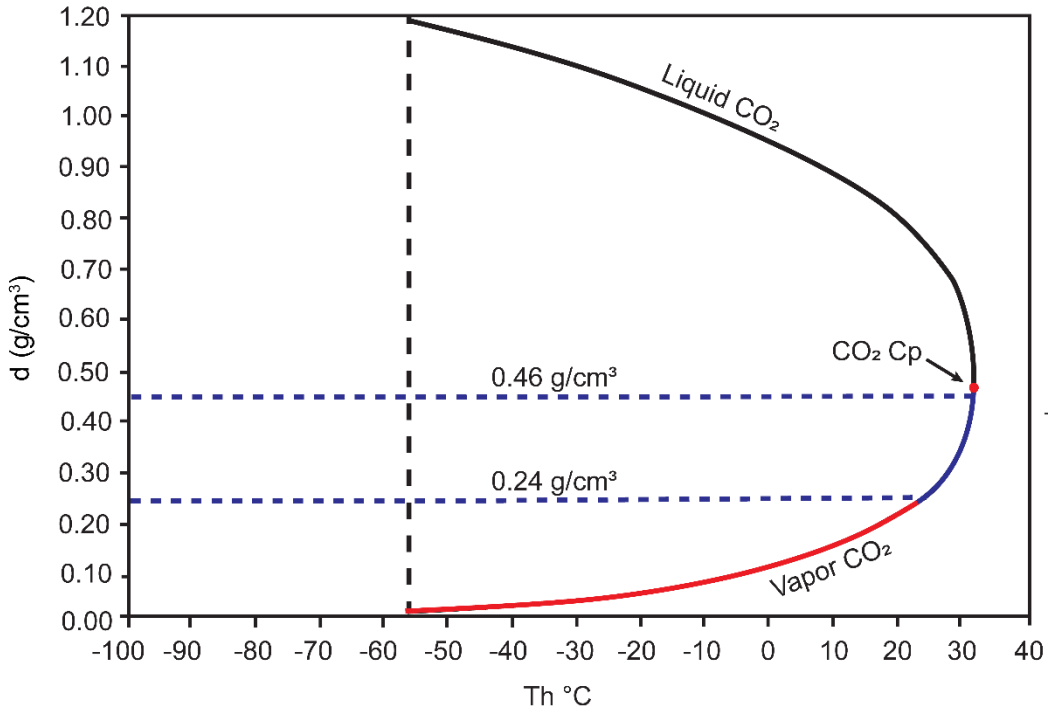

Fig. S.1 CO_2 density (d) vs homogenization temperature (Th) plot (modified after Van den Kerkhof and Thiery, 2001 [1]). The blue dotted lines correspond to the highest and the lowest threshold densities (i.e, 0.46 g/cm^3, and 0.24 g/cm^3, respectively) set after the residual bootstrapping. These define the Th – d interval (blue solid curve) comprising the thresholds set for all the other equations, corresponding to CO_2 fluids homogenizing to the vapor phase. The red dot corresponds to the CO_2 critical point (Cp, d = 0.466 g/cm^3 at 31.1 °C). The solid black curve defines the Th – d interval where CO_2 homogenizes to the liquid phase, while the red one the interval where CO_2 homogenizes to the vapor phase, below the threshold densities.

7.1.2 References

1. A. Van den Kerkhof, and R. Thiery. "Carbonic inclusions." *Lithos*. 2001. 55(1-4): 49-68.

8. AKNOWLEDGMENTS

Il mio più sincero grazie va alla Professoressa Maria Luce Frezzotti, senza la quale questa tesi non sarebbe mai stata scritta, né questo traguardo raggiunto. Con i suoi continui sproni, mi ha sempre motivata ad andare avanti, oltre ad avermi fatto toccare con mano cosa voglia dire essere innamorati della Scienza ed essere curiosi di scoprire quale storia le rocce ci possano raccontare.

To Professor Bob Bodnar and to all the collegues I met at the Virginia Tech, thank You. Thank You for hosting me in Your laboratory and for let me know Science from different points of view.

Un grazie di vero cuore va alla Professoressa Simona Ferrando che ha contribuito, forse più di quanto possa immaginare, alla mia crescita, oltre che avermi dato un prezioso aiuto durante questi anni (e sono tanti, fin dalla triennale).

Grazie al Professor Alessandro Aiuppa, al Dottor Andrea Rizzo e ad Andres, senza i quali i risultati di questo dottorato non avrebbero avuto una marcia in più.

Un sincero grazie pieno di stima va a Tullio, con il suo aiuto statistica e geologia si sono incontrate lungo questo percorso di dottorato e hanno prodotto un eccellente risultato.

Non posso non ringraziare, infine, il Pollo, una mascotte senza eguali nelle giornate passate in laboratorio Raman. Veronica può sicuramente capire ed approvare.

Sono passati quasi quattro anni dall'inizio di questo percorso. Tante persone mi hanno accompagnata lungo la strada. Alcune ci sono sempre state e rimangono tutt'ora al mio fianco, altre non possono essere qui fisicamente, e altre se ne sono andate. A tutti loro, comunque, un grazie, il più sincero e profondo, di cuore. Tutti loro hanno contribuito a fare di me ciò che sono.

Grazie mamma e papà, grazie Chicco, nonni e a tutta la mia famiglia. E sì, grazie anche ai miei angeli custodi… sarete sempre nel mio cuore e zio, manchi tanto quaggiù.

Grazie a tutti i miei amici, vecchi e nuovi. Grazie a quelle bestie di italiani che ho incontrato in America, siete davvero fantastici (come le nostre lasagne :-P).

Grazie ad Annarita… sei una persona speciale, un'amica come pochi. Grazie davvero per avermi portata a prendere quel caffè, quel 23 settembre 2019: ho conosciuto una grande e preziosa amica quel giorno.

Ad Andrea… ti amo.

9. APPENDIX

9.1 Peridotitic samples petrography and fluid inclusions studies

Fluid inclusions analysed for the present work of thesis have been selected in peridotitic mantle xenoliths collected from El Hierro (Canary Islands) and from the Lake Tana region (Ethiopia). In the following paragraphs a brief geological framework and a summary of the mantle xenoliths petrography and fluid inclusion studies are presented. More comprehensive petrographic and petrological studies can be found in previous works (Oglialoro et al., 2017; Ferrando et al., 2008; Frezzotti et al., 2010; Frezzotti et al., 2012b).

In the following chapters, minerals will be abbreviated according to Whitney and Evans (2010).

9.1.1 El Hierro (Canary Islands)

El Hierro is the westernmost and youngest Islands of the Canary Island archipelago (Becceril et al., 2016). Its sub-aerial magmatic activity started approximatively around 1.12 Ma in the NE part of the island (Carracedo et al., 2001), with the most recent eruption occurred on the 2011-2012 in the La Restinga area. The magmatic activity is characterised by intraplate oceanic volcanism, dominated by alkali-basalts and minor tholeiites and differentiated lavas.

The mantle xenoliths considered for the present work of thesis have been collected by Oglialoro et al. (2017) from the El Julan Cliff Valley (Fig.1), in massive lava flows dated at approximatively 40-30 ka (Oglialoro et al., 2017 and references therein).

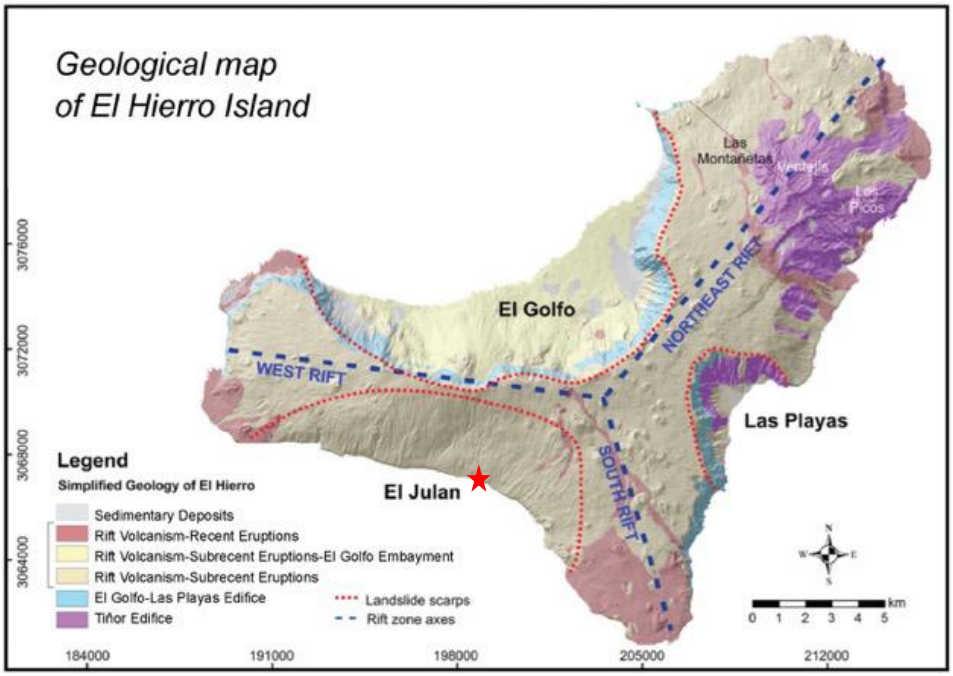

Fig.1 Geological map of El Hierro island (Canary Islands), modified after Oglialoro, 2017. The red star indicates the sampling locality where considered samples have been collected by Oglialoro et al. (2017).

9.1.1.1 Petrography and mineral chemistry

Mantle xenoliths have been described by Oglialoro et al. (2017). The studied peridotites have been classified as type I following the classification of Frey and Prinz (1978), and consist of three spinel-dunites (Ol: 92-94 vol%; Opx: 4-6 vol%; Cpx: 1-4 vol%), five spinel-harzburgites (Ol: 59-78 vol%; Opx: 18-38 vol%; Cpx: 2-4 vol%), and three spinel-lherzolites (Ol: 63-78 vol%; Opx: 11-26 vol%; Cpx: 11-12 vol%).

Most of the samples are characterised by protogranular texture with variable recrystallization degree (around 20% on average), while one spinel-lherzolite is characterised by porphyroclastic texture with a higher fraction of neoblasts. Two generations of olivine (Ol) and orthopyroxene (Opx) have been recognised: Ol I and Opx I porphyroclasts (Fig. 2a, c) consist of big (up to 25 mm) strained crystals, while Ol II and Opx II (Fig.2b) in strain-free interstitial grains or aggregates of polygonal grains with triple junctions. Opx I can contain exsolution lamellae of clinopyroxene (Cpx) + spinel (Spl), but in more recrystallized peridotites, it shows clear rims. Cpx and Spl are also present as small (1 mm on average; Fig.2a,b,c, and d) subhedral or interstitial grains. Olivines (Ol I and Ol II) are Fo-rich, with Mg-numbers (Mg# = Mg/(Mg + Fe_{tot})*100, molar) from 89 to 91, being higher in spinel-harzburgites. Orthopyroxenes (Opx I and Opx II) are En-rich, with Mg# similar to those of Ol I and II, from 90 to 91. Cpx is Cr-Diopside, and it is characterised by a wide Mg# range, from 89 to 93. Spl

is variable in composition, being a Mag-Spl solid solution, with Cr-number (Cr# = Cr/(Cr + Al)*100, molar) from 25 to 35. Moreover, some Spl grains are characterised by Chr-rich rims, having Cr# roughly from 40 to 50.

Studied peridotites have been equilibrated at mantle conditions, between 1.5-2 Gpa, at 900-1100°C.

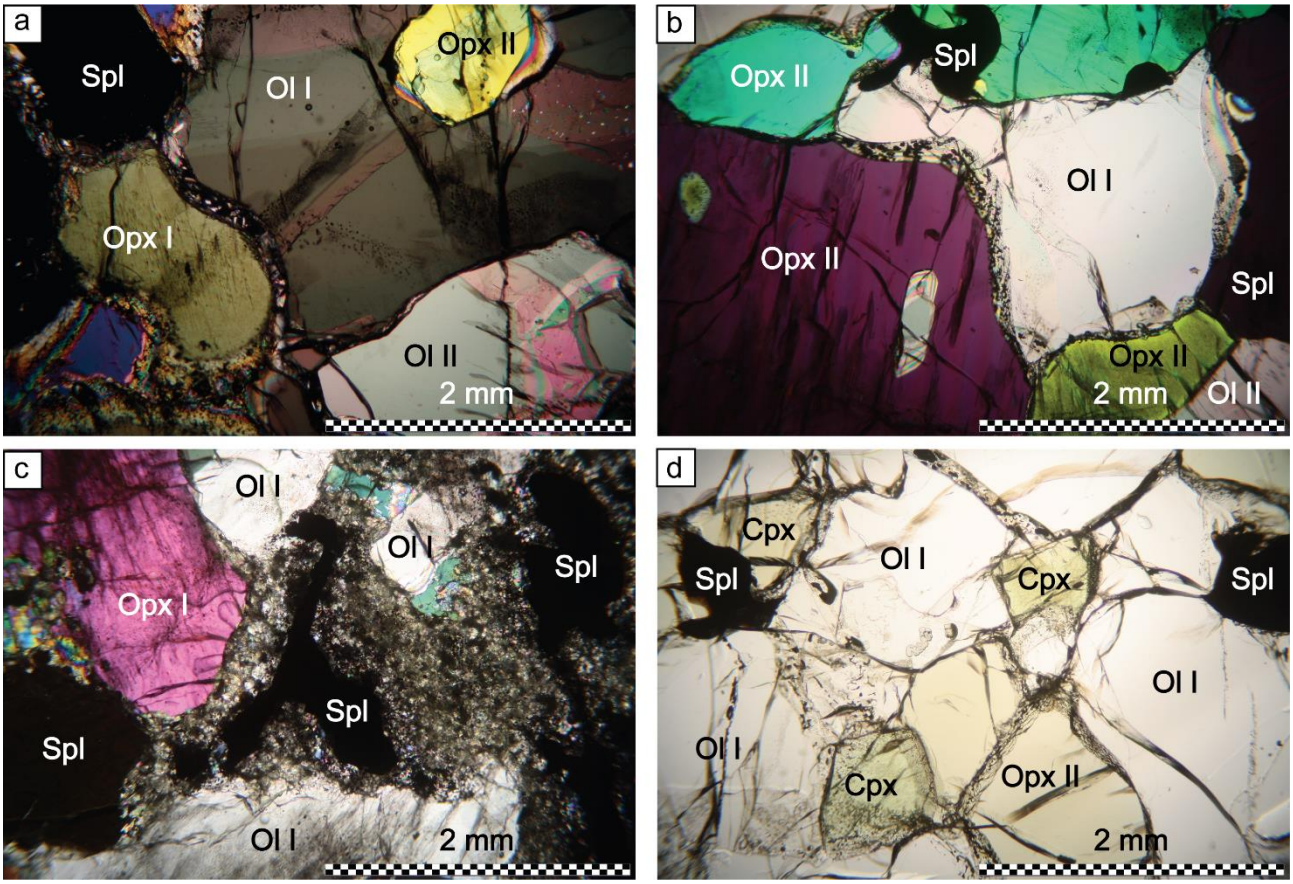

Fig.2 Microphotographs of peridotitic samples from El Hierro, Canary Islands. a) porphyroclasts of Ol I and Opx I, and Spl subhedral grains associated with neoblasts of Ol II and Opx II in a Spl-lherzolite (XML8); b) porphyroclasts of Ol I associated with neoblasts of Opx II and Spl subhedral grains in a Spl-harzburgite (XML11); c) porphyroclasts of Ol I and Opx I associated with Spl and surrounded by patches containing small crystals of Ol and glass in a Spl-harzburgite (XML4); d) porphyroclasts of Ol I associated with Cpx and Sp and Opx II neoblasts in a Spl-harzburgite (XML7).

Within the same suite of peridotitic xenoliths, a third generation of Ol and Opx with subordinate Cpx, carbonates crystals, carbonates and sulphates droplets and interstitial glass have been also observed in intragranular and interstitial microveins and patches (Fig.3a, and b; Tiraboschi et al., 2017). Intragranular veins in Ol I are also associated with globular inclusions of carbonates and

sulphates (Fig.9.3c, d). Carbonates are Mg-Cal, while the interstitial glass has variable SiO_2 content from 59 to 69 wt% and Mg# from 35 to 60 (Tiraboschi et al., 2017).

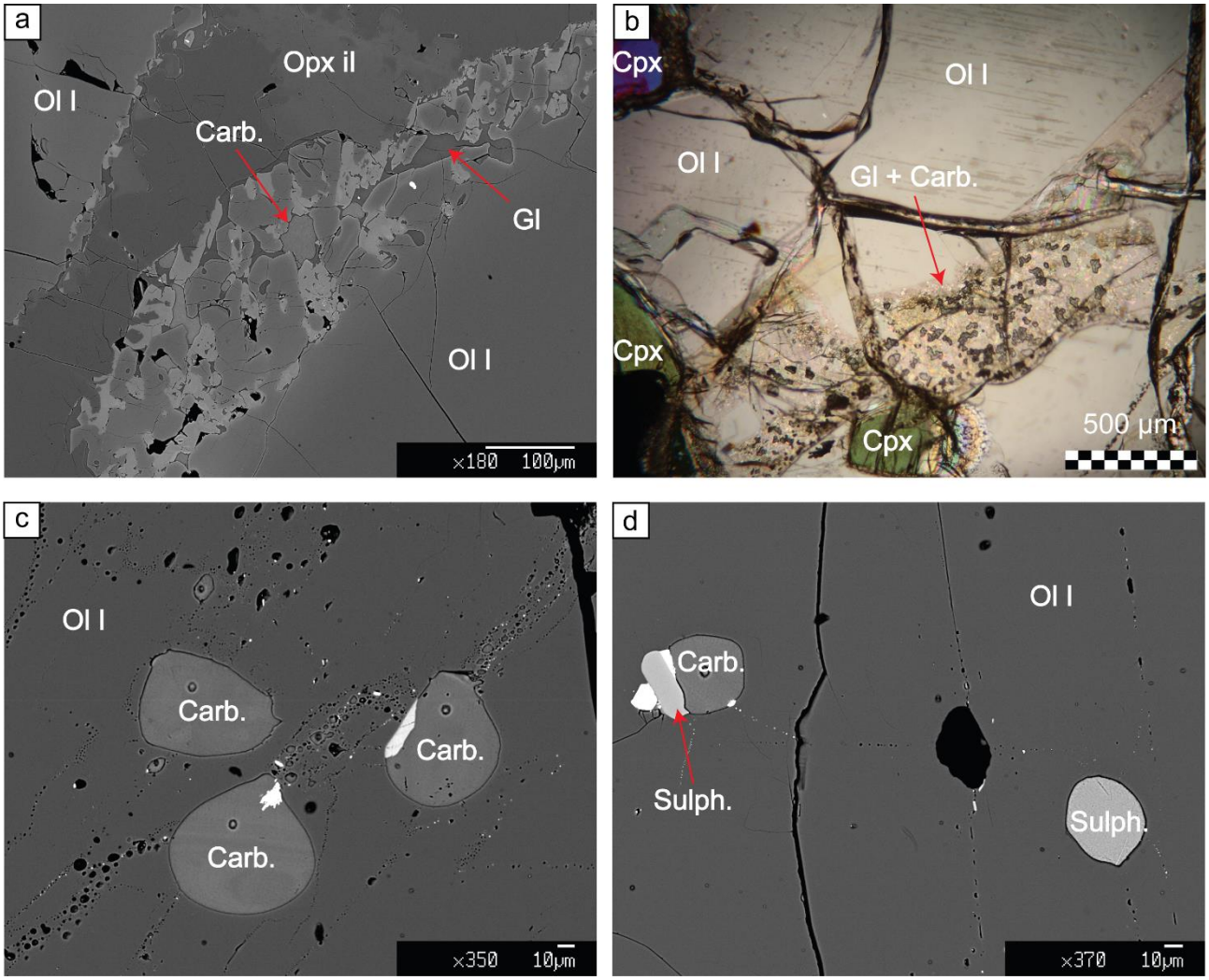

Fig.3 BSE images (a, c, and d) and microphotograph (b) of interstitial and intragranular microveins containing silicate glass and carbonates (a, and b) and globular inclusions containing carbonates and sulphates in Ol I (c, and d; modified after Tiraboschi et al., 2017) in peridotitic samples from El Hierro, Canary Islands. Gl = glass; Carb. = carbonates; Sulph. = sulphates.

9.1.1.2 Fluid inclusions study

Different generations of fluid inclusions have also been observed within all the rock-forming minerals. These have been previously studied by Oglialoro et al. (2017) and by Remigi et al. (2019). Fluid inclusions have been classified by Oglialoro et al. (2017) in two fluid inclusion assemblages (FIA): *Early Type I* and *Late Type II*. Further petrographic investigations have been also performed by Remigi et al. (2019):

1) *Early Type I* (FIA1): divided into *Type I*a, *Type I*b, and *Type Ic*. *Type Ia* fluid inclusions coexist in secondary intergranular trails with *Type Ib*, in Ol I and Opx I; they are also often found in association with carbonate-rich inclusions and intragranular and interstitial carbonate-silicate glass microveins. *Type 1a* fluid inclusions (Fig.4a) are mono-phase (L) CO_2-rich, and contain $CO_2 \pm N_2$ ($CO_2 \approx$ 82.0-100.0 mol%; $N_2 \approx$ 0.0-18.0 mol%). Fluid inclusions density is up to 1.19 g/cm^3. *Type Ib* fluid inclusions (Fig.4b) are multiphase solid (≥ 70 vol% of daughter minerals), consisting of Anh+ Sulfohalite+ Na-K chlorides+ Ap+ Dol+ Mg-Cal+ Spl+ Mgs+ Mg-sulf+ Tlc + $CO_2 \pm N_2$ (N_2 = 0.3-1.25 mol%)+ H_2O. *Type I*c fluid inclusions (Fig.4c) are rare and found as primary isolated clusters with negative crystal shapes within the rims of Opx II crystals. These are bi-phase (L+S) CO_2-rich and contain $CO_2+S^0 \pm SO_2$ ($SO_2 \approx$ 0.0-1.5 mol%). Fluid inclusions density ranges from 1.10 to 0.99 g/cm^3.

2) *Late Type II* (FIA2): *Type* II fluid inclusions are found in secondary intergranular trails in all the mineral phases (Fig.4d) and are often characterised by the presence of decrepitation microtextures. These consist of mono-phase (L) CO_2 fluid inclusions, having densities from 0.37 to 1.08 g/cm^3.

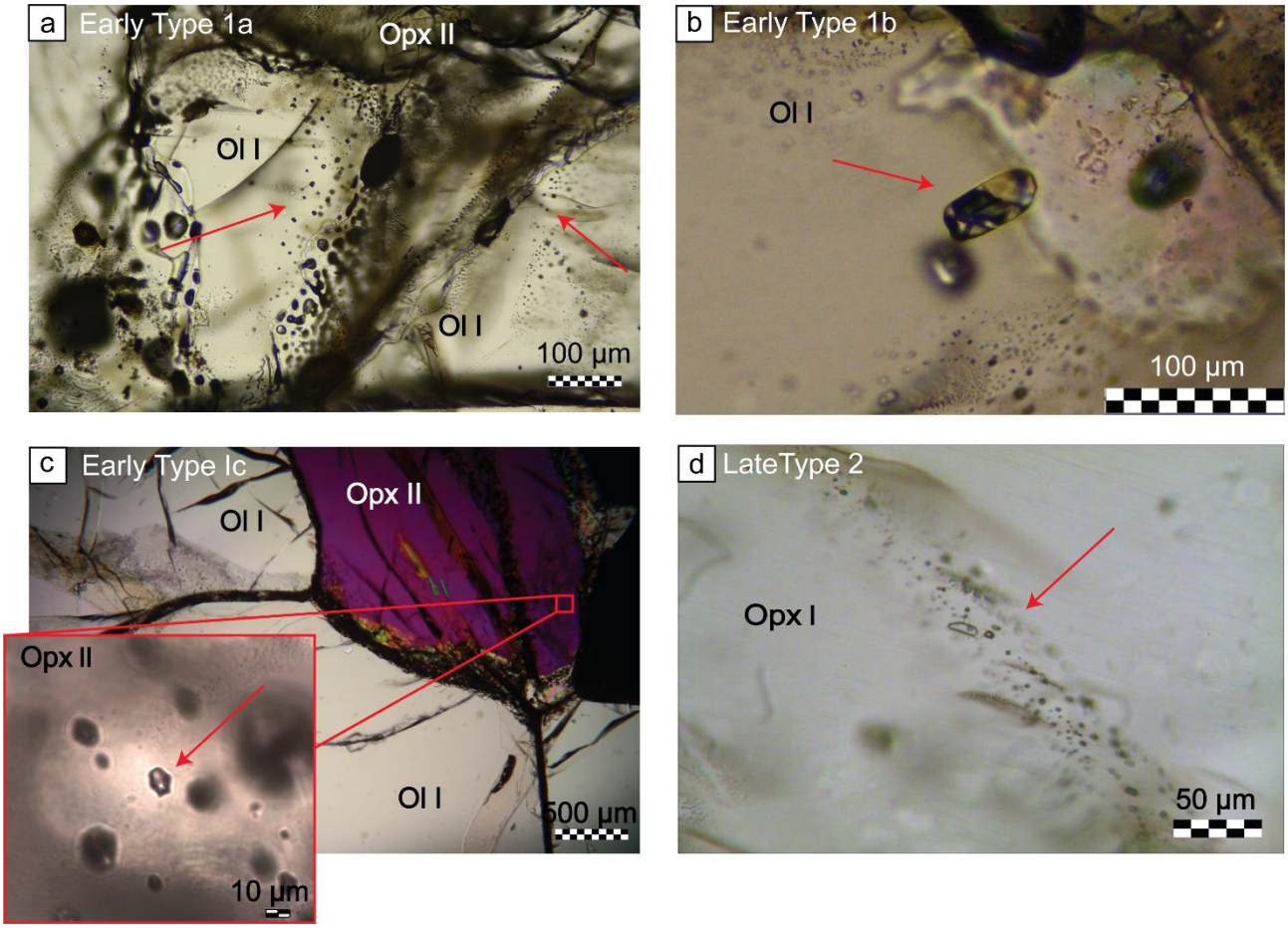

Fig.4 Photographs of studied fluid inclusions types in mantle peridotites from El Hierro (Canary Islands), modified after Remigi et al., 2019. a) *Early Type 1a*, CO_2 + N_2 and b) *Early Type 1b*

multiphase solid fluid inclusions trapped in Ol porphyroclast (Ol 1); c) *Early Type 1c* $CO_2 + S^0 \pm SO_2$ fluid inclusions trapped in metasomatic Opx (Opx II; crossed polarizers); d) *Late Type 2*, CO_2 pure fluid inclusions in Opx porphyroclast (Opx I).

9.1.2 Lake Tana region (Ethiopia)

The Lake Tana region is located in the north-western and more recent part (Miocene-Quaternary) of the Ethiopian Plateau. The region belongs to the Miocene-Quaternary volcanic deposits of the Ethiopian Volcanic Province (EVP; Gass, 1970; Mohr, 1983; Fig.5). The Quaternary volcanic activity in the region developed within the Tana graben, and it is characterised by fissure-type lava fields and small- to medium-sized tuff cones, tuff rings and maars. Erupted volcanics are mainly porphyritic, vesicular alkali basanites, with typical geochemical features of intraplate magmatism (Ferrando et al., 2008 and references therein).

The mantle xenoliths considered for the present work of thesis have been studied by Ferrando et al. (2008), and Frezzotti et al. (2010, and 2012b), and come from the Injibara Quaternary lavas, consisting of a massive, sub-aphyric and weakly vesiculated lava flow that erupted from a small scoria cone, located SW of Injibara.

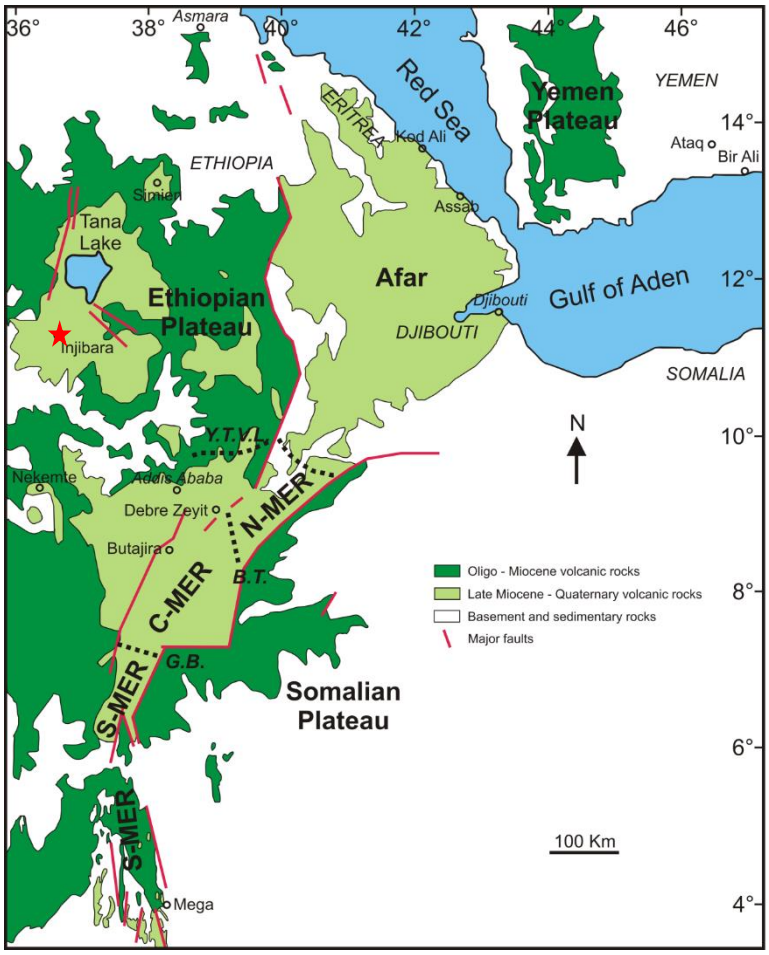

.

Fig.5 (Previous page) Geological sketch map of Ethiopian-Somalian-Yemen plateau, Afar and Main Ethiopian Rift, modified after Casagli et al., 2017. The red star indicates the sampling locality.

9.1.2.1 Petrography and mineral chemistry

Mantle xenoliths have been described by Ferrando et al. (2008). The studied peridotites consist of 22 spinel-lherzolites (Ol: 46-69 vol%; Opx: 19-31 vol%; Cpx: 9-22 vol%). Eleven samples show additional presence (up to 1 vol%) of Amp.

Based on textural features (after Mercier and Nicholas, 1974), the samples are distinguished in three groups: *Deformed spinel-lherzolite*, *Granular spinel-lherzolites* and *Transitional spinel-lherzolites*.

Deformed spinel-lherzolites are characterised by protogranular to porphyroclastic textures. Two generations of Ol and Opx have been recognised: Ol I and Opx I porphyroclasts consist of large (2-4 mm) deformed porphyroclasts, while Ol II and Opx II form polygonal neoblasts (up to 1 mm in size). Opx I contains Cpx-exsolution lamellae. Cpx is present as smaller (≈1 mm) interstitial and tabular grains, and it can contain Spl-exsolution lamellae. Spl is porphyroclastic or holly-leaf shaped. Where present, Amp occurs in contact with Cpx and contains relics of Spl.

Granular spinel-lherzolites are characterised by equigranular textures with minor porphyroclasts of Ol and Opx (<20%). Two generations of Ol and Opx are observed: Ol I and Opx I forms rare and deformed porphyroclasts (up to 4 mm in size), while Ol II and Opx II consist of undeformed polygonal neoblasts (up to 2 mm in size) with triple junctions. Ol I can include Cpx and blebs of Spl, while Opx I contains undeformed Cpx exsolution lamellae. Cpx is unevenly distributed in the rocks with the same petrographic features of Cpx in deformed xenoliths. Spl is present in two generations: Spl I forms holly-leaf rare crystals, up to 1 mm in size, with black borders, while Spl II forms tiny (≤0.5 mm) crystals located in triple junctions with Ol II and Opx II. Spl II defines a fine foliation. Where present, Amp has the same petrographic features as those observed for *Deformed spinel-lherzolites*, and it is always found in association with Spl I.

Transitional spinel-lherzolites are characterised by porphyroclastic texture with a tendency to equigranular. The mineral assemblage is the same observed for the other two types of spinel-lherzolites and it is also characterised by the same petrographic features.

Studied peridotites outline a progressive enrichment from the *Deformed spinel-lherzolites* to *Granular spinel-lherzolites.* In *Deformed spinel-lherzolites*, olivines (Ol I and Ol II) are Fo-rich and

have Mg# ranging from 89.2 to 89.6. Orthopyroxenes (Opx I and Opx II) are En-rich, with Mg# from 89.9 to 90.3. Cpx is Ti-poor, Cr-Na-rich diopside, with Mg# from 89.8 to 91. Spl has Mg# from 72.9 to 75.1, and Cr# from 15 to 19. Amp is Cr-rich Prg and has Mg# from 87.5 to 88.2, and it is Cl-rich.

In *Granular spinel-lherzolites*, Ol I has a Fo content ranging from $Fo_{89.3}$ to $Fo_{89.5}$, while Ol II from $Fo_{87.9}$ to $Fo_{89.2}$. Orthopyroxenes are En-rich: Opx I has Mg# from 89.8 to 90.0 (similar to Opx I and II in deformed peridotites), while Opx II from 88.8 to 89.6. Cpx is Di-rich, and it is characterised by Mg# of 88.8-90.5 (lower than that of Cpx in deformed peridotites). Spinels (Spl I and Spl II) have Mg# from 75.2 to 78.7 (higher than that in Spl of deformed peridotites) and Cr# from 7 to 10 (lower than that of Spl in deformed xenoliths). Amp is Prg, and has Mg# from 87.4 to 88.2 (the same as Prg in deformed xenoliths), and it is Cl-free.

As for the petrographic features, in *Transitional spinel-lherzolites*, the chemical composition of the mineral assemblage overlaps with that of the other groups of peridotites.

Peridotites have been equilibrated at mantle conditions, between 1.3-2 Gpa, at 950-1150°C.

Trace elements on Cpx and Prg in *Deformed spinel-lehrzolites* have been further analysed by Frezzotti et al. (2010, 2012b). Cpx showed LREE enrichment on HREE and flat REE patterns. HREE were relatively high, excluding re-equilibration with garnet. In particular, positive anomalies of LILE, in particular Th, U, Pb, and LILE/HFSE fractionation, were observed. Ti, Zr, and Hf showed moderate negative REE anomalies, and Nd and Ta contents lower than those in the primitive mantle. Prg, instead, was Cl-rich and was characterised by LREE, Pb, U, Th, and Sr similar to those of Cpx, but it concentrated Ba. Prg was not characterised by enrichments in Nb and Ta.

9.1.2.2 Fluid inclusion study

Fluid inclusions have also been described by Frezzotti et al. (2010, 2012b). They are present only in *Deformed spinel-lherzolites* as small clusters and trails in Ol I and Opx I, and are rare in Cpx. In Ol I, few fluid inclusions contain $CO_2 \pm H_2O$, while most of them react with the host mineral and are filled by daughter Tlc or Cal+Mgs without any fluid. In Opx I, fluid inclusions consist of $CO_2 \pm H_2O$ ($CO_2 \geq 80$ vol%). In Cpx, rare pure CO_2 fluid inclusions form alignments with tiny Amp inclusions (Cl-rich Prg equal in composition to that in the host rock). H_2O has been detected by mean of Raman micro-spectroscopy in few fluid inclusions trapped in Ol I and Opx I. Further, the association of Cl-Prg + CO_2 within the rare fluid inclusions in Cpx suggested that a reaction between CO_2+H_2O fluids and Cpx has occurred to form Prg, leaving residual CO_2.

Eutectic temperatures measured in fluid inclusions indicated the additional presence of Na^{+}, Mg^{2+} and Fe^{2+}, with little or no Ca^{+} within the aqueous fluid. Fluid inclusions density resulted in being around 1.12 g/cm^3.

9.1.3 References

Becerril, L., Galve, J. P., Morales, J. M., Romero, C., Sánchez, N., Martí, J., and Galindo, I. (2016). Volcano-structure of El Hierro (Canary Islands). *Journal of Maps*, ***12*****(sup1)**, 43-52; https://doi.org/10.1080/17445647.2016.1157767

Carracedo, J. C., Badiola, E. R., Guillou, H., de la Nuez, J., and Pérez Torrado, F. J. (2001). Geology and volcanology of La Palma and El Hierro, Western Canaries. *Estudios Geológicos*, **57(5-6)**, 175–273; https://doi.org/10.3989/egeol.01575-6134

Casagli, A., Frezzotti, M. L., Peccerillo, A., Tiepolo, M., and De Astis, G. (2017). (Garnet)-spinel peridotite xenoliths from Mega (Ethiopia): Evidence for rejuvenation and dynamic thinning of the lithosphere beneath the southern Main Ethiopian Rift. *Chemical Geology*, ***455***, 231-248; https://doi.org/10.1016/j.chemgeo.2016.11.001

Ferrando, S., Frezzotti, M. L., Neumann, E. R., De Astis, G., Peccerillo, A., Dereje, A., ... and Teklewold, A. (2008). Composition and thermal structure of the lithosphere beneath the Ethiopian plateau: evidence from mantle xenoliths in basanites, Injibara, Lake Tana Province. *Mineralogy and Petrology*, **93(1)**, 47-78; https://doi.org/10.1007/s00710-007-0219-z

Frey, F. A., Prinz, M. (1978). Ultramafic inclusions from San Carlos, Arizona: petrologic and geochemical data bearing on their petrogenesis. *Earth and Planetary Science Letters*, **38(1)**, 129-176; https://doi.org/10.1016/0012-821X(78)90130-9

Frezzotti, M. L., Ferrando, S., Peccerillo, A., Petrelli, M., Tecce, F., and Perucchi, A. (2010). Chlorine-rich metasomatic H_2O–CO_2 fluids in amphibole-bearing peridotites from Injibara (Lake Tana region, Ethiopian plateau): nature and evolution of volatiles in the mantle of a region of continental flood basalts. *Geochimica et Cosmochimica Acta*, **74(10)**, 3023-3039; https://doi.org/10.1016/j.gca.2010.02.007

Frezzotti, M. L., Ferrando, S., Tecce, F., and Castelli, D. (2012b). Water content and nature of solutes in shallow-mantle fluids from fluid inclusions. *Earth and Planetary Science Letters*, **351**, 70-83; https://doi.org/10.1016/j.epsl.2012.07.023

Gass, I. G. (1970). The evolution of volcanism in the junction area of the Red Sea, Gulf of Aden and Ethiopian rifts. *Philosophical Transactions for the Royal Society of London. Series A, Mathematical and Physical Sciences*, **267(1181)**, 369-381; http://www.jstor.org/stable/73627

Mercier, J. C., Nicolas, A. (1975). Textures and fabrics of upper-mantle peridotites as illustrated by xenoliths from basalts. *Journal of Petrology*, **16(1)**, 454-487; https://doi.org/10.1093/petrology/16.1.454

Mohr, P. (1983). Perspectives on the Ethiopian volcanic province. *Bulletin volcanologique*, **46(1)**, 23-43; https://doi.org/10.1007/BF02598243

Oglialoro, E. (2017). The Magma Plumbing System of the Rift Volcanism Activity in El Hierro, Canary Islands: Fluid Inclusion, and Petrological Studies. Ph.D thesis; http://hdl.handle.net/10281/153284

Oglialoro, E., Frezzotti, M. L., Ferrando, S., Tiraboschi, C., Principe, C., Groppelli, G., and Villa, I. M. (2017). Lithospheric magma dynamics beneath the El Hierro Volcano, Canary Islands: insights from fluid inclusions. *Bulletin of Volcanology*, **79(10)**, 1-17; https://doi.org/10.1007/s00445-017-1152-6

Remigi, S., Frezzotti, M. L., and Ferrando, S. (2019). Generation of CO_2-SO_2 fluxes in the lithospheric mantle beneath El Hierro (Canary Islands) on metasomatic reactions of carbonate-rich silicate melts. In *XXV ECROFI Conference (European Current Research On Fluid Inclusions)* (pp. 102-102).

Tiraboschi, C., Malaspina, N., Ferrando, S., Petrelli, M., and Frezzotti, M. L. (2017). Carbonate metasomatism in the lithosphere beneath El Hierro (Canary Islands): new insights on carbon mobilization from deep mantle xenoliths. In *Congresso SIMP-SGI-SOGEI-AIV 2017* (pp. 454-454). SIMP.

Whitney, D. L., Evans, B. W. (2010). Abbreviations for names of rock-forming minerals. *American mineralogist*, **95(1)**, 185-187; https://doi.org/10.2138/am.2010.3371

10. SUMMARY OF PUBLICATIONS, AND CONFERENCES, COURSES, AND SCHOOLS ATTENDED DURING THE PH.D. COURSE

10.1 Publications

10.1.1 Journal papers

Remigi, S., Mancini, T., Ferrando, S., Frezzotti, M.L. (2021) Interlaboratory Application of Raman CO_2 Densimeter Equations: Experimental Procedure and Statistical Analysis Using Bootstrapped Confidence Intervals. *Applied Spectroscopy*; doi:10.1177/0003702820987601

10.1.2 Contribution to Conferences

Kung, J., Villa, I.M., Remigi, S. (2018): Raman Microprobe Constraints on the Ar Degassing Mechanisms in Gem-Quality Sanidine. Goldschmidt Abstracts, 2018 1371

Remigi, S., Ferrando, S., and Frezzotti, M. (2016). Fluid-Assisted Coesite-Quartz Transition in the Dora-Maira Whiteschists, Western Alps: Petrographic and Raman Studies. Intervento presentato a: EMC, Rimini.

Remigi, S., Frezzotti, M., and Ferrando, S. (2019). Generation of CO_2 - SO_2 fluxes in the lithospheric mantle beneath El Hierro (Canary Islands) on metasomatic reactions of carbonate-rich silicate melts. Intervento presentato a: ECROFI, Budapest.

Remigi, S., Frezzotti, M., Ferrando, S., Villa, I., and Maffeis, A. (2017). The reliability of Raman micro-spectroscopy in measuring the density of CO_2 mantle fluids. Intervento presentato a: AGU Fall meeting 2017, New Orleans, USA.

Remigi, S., Mancini, T., Ferrando, S., and Frezzotti, M. (2020). The statistical equivalence of the CO_2 Raman densimeter equations. Intervento presentato a: Goldschmidt Virtual, Hawaii.

10.2 Conferences Attended

AGU Fall Meeting 2017, New Orleans, US

Goldschmidt 2018, 12-17th August 2018, Boston, US

ECROFI 2019, 24-26th June 2019, Budapest, HU

Goldschmidt 2020 Virtual conference, 21-26th June 2020, Hawaii

10.3 Courses and Schools attended

COURSES

Technologies to support research;

Writing a scientific paper;

Bibliographic literature review;

How to make a scientific presentation;

Scientific communication;

Scanning and Transmission Electron Microscopy, Principles and Applications;

Isotopes as Environmental tracers;

SCHOOLS

"Fluid in the Earth", Naples, Italy; 24/10/2016 - 29/10/2016

"Carbon forms, paths and processes in the Earth" Lake Como School, Como, Italy; 16/10/2016 - 20/10/2017

"Fluid in the Earth", Naples, Italy; 06/11/2017 - 11/11/2017

Workshop "Terra, Vita e Clima: il ciclo del carbonio", Pisa, Italia; 22/11/2018 – 23/11/2018